J. Iversen
M. Moghadam
January 1981

Final Report

EXPERIMENTAL INVESTIGATION OF VORTICES SHED BY VARIOUS WING FIN CONFIGURATIONS

Langley Research Center
Grant No. NSG 1582

ISU-ERI-Ames-81112
Project 1401

ENGINEERING RESEARCH INSTITUTE
IOWA STATE UNIVERSITY
AMES, IOWA 50010 USA

ENGINEERING RESEARCH

ENGINEERING RESEARCH
ENGINEERING RESEARCH
ENGINEERING RESEARCH
ENGINEERING RESEARCH

Final Report

EXPERIMENTAL INVESTIGATION OF VORTICES SHED BY VARIOUS WING FIN CONFIGURATIONS

J. Iversen
M. Moghadam
January 1981

Langley Research Center
Grant No. NSG 1582

ISU-ERI-Ames-81112
Project 1401

DEPARTMENT OF AEROSPACE ENGINEERING
ENGINEERING RESEARCH INSTITUTE
IOWA STATE UNIVERSITY AMES, IOWA 50011

TABLE OF CONTENTS

LIST OF SYMBOLS

A_{INLET}	Test section inlet area
A_{OUTLET}	Test section outlet area
a_c	Rankine vortex core radius
a_w	Average lift curve slope
AR_F	Fin aspect ratio
AR_{OF}	Optimum fin aspect ratio
AR	Follower aspect ratio
b_F	Fin span
b'_F	Spanwise separation between trailing vortex of fin and its base
b_G	Wing span of the generator
b'_G	Spanwise separation between trailing vortices of generator wing
b	Span of the follower model
c_G	Chord length of the generator wing
$\bar{c}_G$	Mean geometric chord of the generator wing
$\bar{c}_F$	Mean geometric chord of the fin
c	Chord length of the follower model
c_L	Lift coefficient
c_{L_G}	Lift coefficient of the generator
C_{L_F}	Fin lift coefficient
c_ℓ	Rolling moment coefficient
L	Rolling moment
$L_{T.S.}$	Length of the test section

$\vec{\ell}$	Distance along a closed nonintersecting curve
M	Pitching moment
N	Yawing moment
$\vec{n}$	Unit vector perpendicular to an open, two-sided surface
q	Dynamic pressure
r	Rankine vortex radius
r_{ij}	Radius from centroid of circulation
S_F	Fin plan-form area
S_{WING}	Wing area
S_G	Generator wing area
$\hat{s}$	An open, two sided surface
S_R	Rotor frontal area
S	Follower wing area
$t_{G_{MAX}}$	Generator wing maximum thickness
$t_{F_{MAX}}$	Fin maximum thickness
V_∞	Free stream velocity
u_θ	Tangential velocity
$\vec{V}$	Local total velocity
X	Drag force
Y	Side force
y	Rolling moment arm on the follower
Z	Normal force
α	Follower angle of attack

α_{WING}	Wing angle of attack
α_F	Angle of attack of the fin relative to free stream velocity
α_{OF}	Optimum angle of attack of the fin relative to free stream velocity
Γ	Fin circulation
Γ_G	Generator circulation
Γ_0	Fin vortex total circulation
γ	Circulation in point vortices
π	= 3.14159265
ρ	Density
ω	Rotor angular velocity
$\int$	Integral
$\int_c$	Line integral around a closed curve c
$\iint_{\hat{s}}$	Surface integral over an area $\hat{s}$

CHAPTER I. INTRODUCTION

During recent years much attention has been focused on the problem of trailing vortex hazards. When a following aircraft flies into the vortex wake of a generator aircraft, the following aircraft can experience large excursions, particularly in bank angles from the desired flight path. This problem is most evident and most dangerous during take-off and landing operations. One solution which has been enforced by FAA under instrument flight rules, is to set the separation distances large enough (about six miles) so that the vortices shed by the generator aircraft become sufficiently weak or far removed for the safe approach of the following aircraft. This solution however, reduces the traffic capacity of already busy airfields. Therefore, research has been conducted by NASA, FAA and the aircraft companies in the hopes of solving the problem by means of alleviating the hazard by reducing the strength of the generated vortex wake.

The results (1) have indicated that alleviation of the vortex wake hazard is possible by introducing a vortex interaction mechanism (fins, strakes, flaps, spoilers, engine-thrust, etc., can produce interaction mechanisms). In any case, the primary motive is to reduce the separation distances as much as possible, while paying the least penalty

for the generator aircraft performance. The interaction of an upper surface fin vortex with the wing tip vortex has proven to be one successful possibility. However, there are no definite general design criteria for determination of optimum shape, size and spanwise position of wing fin configurations. The purpose of the present study is to assist determination of optimum shape and size of aerodynamic fins.

An experimental investigation has been conducted at Iowa State University in the open circuit wind tunnel of the Aerospace Engineering Department. Forty-six different fins, which are members of twelve plan-form families, have been tested. Individual members of each family differed in some respect from the rest. This difference was mostly in aspect ratio whereas, some also differed in thickness and/or edge conditions.

A two-dimensional Boeing single element airfoil at an angle of attack of eight degrees and a sweepback angle of thirty-two was used to simulate a portion of the wing of a generator aircraft. Various free stream velocities were used to test any individual fin at its particular angle of attack. While the fin itself was mounted on the upper surface of the generator model, the angle of attack of each fin was varied until stall was reached and/or past.

The relative fin vortex strengths were measured in two

ways. First, the maximum angular velocity of a four blade rotor placed in the fin vortex center was measured with the use of a stroboscope. Second, the maximum rolling moment on a following wing model placed in the fin vortex center was measured by a force balance.

The two sets of experimental results are in fairly good agreement with each other and with the available theoretical and experimental results.

Problem Review

The strength of the circulatory motion of trailing vortices is directly proportional to the size of the generator vehicle. The history of aircraft growth shows an astonishing increase in size of aircraft over the last fifty years. The increasing rate of vortex strength resulting in the propagation of the wake hazards, therefore is a corollary of aircraft growth.

During the period of 1930 to 1950 the growth rate was practically zero (2). The aircraft size however, has been increasing since the 1950s. It was during the 1960s when wake vortex hazards attracted the attention of air control people. One-fourth of the general aviation accidents associated with turbulence during this period, were involved with the wake vortex hazards (3). The variation of the number of vortex accidents per year, during the 1960s, went up from

the mid-teens to the low twenties.

In recent years, the only solution which has helped the prevention of vortex wake type of accidents, has been the limitation on aircraft spacing during take-off and landing operations. This has caused a decrease in airport utilization rate especially during instrument flight conditions. Extensive research has been planned for exploration of an applicable solution.

It has been almost eighty years since Prandtl and Lanchester investigated the effects of the trailing vortices, of a model wing, on the flow over the wing. Theirs was the first attempt to study the concept of trailing vortices. During the years from 1900 to 1940, some of the basic theory of vortex behavior was developed. In the late 1960's the introduction of the large widebody subsonic transports with their large strength trailing vortices caused the beginning of a new era of wake vortex investigation.

Aircraft vortex wake studies indicate that wakes can follow two different patterns of behavior (1,4,5). First are those vortex wakes which exhibit some instability immediately downstream of the wing, but which quickly reorganize into stable forms of vortices. Second are those which are initially stable and decay slowly (i.e., tip vortex). Results indicate (6,7) that the initially unstable wakes could form a nonhazardous final trailing vortex system, provided a

vortex interaction or quick decay mechanism is injected into the wake. This mechanism could be due to the interaction of like or opposite sign vortices (by use of fins, flaps, or any device which injects a vortex) (6-16), or due to the dispersion of vortices by means of turbulence injection (by use of splines, engine-thrust or any device which injects turbulence) (17-20). Note, the combination of the two mechanisms has also been studied by use of spoilers, and in some cases proven to be effective (21).

Rossow (16) investigated the effects of rectangular fins on the wake of a B747 model. It was found that low aspect ratio fins ($AR_F \approx 0.333$) at high fin angles of attack ($18° \leq \alpha_F \leq 24°$) are more promising than those with high aspect ratio. Further, the optimum fin spanwise position was found experimentally to be near 50% of the semi-span. Theoretical guidelines for accurate estimate of optimum fin position have not yet been developed. Rossow (16), by maximizing the second moment of vorticity for half span of a two-dimensional vortex sheet, attempted to locate the position of the auxiliary vortex (second moment of vorticity is a measure of radius of circulation). This maximization, however, required the largest distance between the centroid of vorticity (obtained from the first moment of vorticity) and the lateral position of injection. Another

approach was used, by combining the first and the second moment of vorticity. The following parameter was found

$$c_v = \sum_{i=1}^{N-1} \sum_{i=i+1}^{N} \gamma_i \gamma_j r_{ij}^2$$

The smallest change in the value of c_v is supposed to confirm the best interaction. Rossow stated that when an auxiliary vortex is injected at the center of sheet vorticity, the change in c_v is minimized, whereas in the first approach the vortex was to be shed at distances far from the centroid. Neither one of the above methods were confirmed by experimental observations.

Iversen (22) by equating the second moment of vorticity of the final vortex to that of the initial vortices, relative to the centroid of vorticity, determined the radius of merged vortices to be five times larger than experimental results. Other methods (i.e., finite difference methods) have also failed to accurately predict the characteristics of merged vortices.

The results indicate (16) that for a B747 model the alleviation of wake hazard is nearly independent of fin height (or injection height) as long as it is less than 0.15 b_G. Iversen (22) shows that for some circular tip, circular, elliptic, rectangular and delta configurations the strength becomes independent of height for aspect ratios larger than

two. Therefore, the aspect ratio of an optimum fin should be small, so that performance penalties are also minimized.

The use of "highly cambered multielement lifting devices" such as wing fins were able to significantly reduce the wake hazard (16). It should be noted that, the wake of a fin is not only directly proportional to lift but it also depends on fin shape (i.e., some high lifting fins could shed rather weak vortices). It is extremely difficult to set a theoretical relation between shape and vortex strength, therefore, strength should be chosen as the dominant factor of importance.

In a later study (23), the minimization of fin size was approached analytically. Assuming equal vortex strength for all fin configurations, the fin size and strength are related to fin lift as

$$\text{"Lift} \approx \frac{\rho V_\infty^2}{2} S_F c_{L_F} = -\rho V_\infty \Gamma b'_F$$

$$\frac{\text{fin lift}}{\text{wing lift}} = \frac{S_F c_{L_F}}{S_G c_{L_G}} = \frac{\Gamma b'_F}{\Gamma_G b'_G}$$

if

$$\frac{b'_F}{b'_G} = \frac{b_F}{b_G} \quad \text{then} \quad \frac{\Gamma}{\Gamma_G} = \frac{c_{L_F}}{c_{L_G}} \frac{\bar{c}_F}{\bar{c}_G} \text{."}$$

For a constant wing vortex strength, the ratio of $\frac{\Gamma}{\Gamma_G}$ is, therefore, a constant. Physically, the last equation means: the smaller the fin the larger the lift coefficient should

be, so that the required alleviation can be achieved. The above derivation can not predict the optimum size of any fin, but it clearly suggests the fact that more configurations ought to be tested. For fin area minimization purposes, a design factor for comparison purposes besides simply the strength of the fin vortex is needed. Iversen (22) suggests the term $\frac{\Gamma}{V_\infty \sqrt{S_F}}$. Therefore, for a particular value of strength, the above term is maximized when $\sqrt{S_F}$ is minimized. Note that minimization of planform area would be approximately equivalent to minimization of fin weight and approximately fin parasite drag.

It has been shown (23), that wing fin planform shapes other than rectangular, could be used to alleviate wake hazards. In fact, the results (23) indicated that circular fins with Clark Y or GA(W)-2 wing sections are effective.

Objectives of the Study

Optimum fin shape, size and angle of attack quidelines, as of this date, are not available. Theoretically, and without the benefit of experimental evidence, the optimization is impossible. On the other hand, the number of possible fin configurations are unlimited. Therefore, experimental investigations of this nature could be lengthy and unpredictable. This study has been undertaken to provide a preliminary set

of guidelines, which could aid in determination of optimum shape, size and angle of attack of fin configurations. For the reasons mentioned above, this study has been primarily experimental.

CHAPTER II. EQUIPMENT AND PROCEDURE

Experimental Set-up

Test section

The tests were conducted in the open circuit wind tunnel of the Aerospace Engineering Department at Iowa State University. A rectangular (A_{INLET} = 36.25 x 30.25 in.^{2}, A_{OUTLET} = 38.0 x 32.0 in.^{2} and $L_{T.S.}$ = 82.0 in.) test section with plexiglass structure, shown in Figure A1 was used. The test section includes a manual traverse system at the outlet, and windows on either sides and on the floor. The traverse system served the purpose of positioning the measuring devices in a two-dimensional plane perpendicular to the free stream. This system is shown in Figure A2. The removable windows on one side of the test section made it possible to reach into the test section as shown in Figure A3.

Wing model

The Boeing single element airfoil (c_G = 9.841 in., $t_{G_{MAX}}$ = 1.093 in.) was mounted in a two dimensional fashion by means of a splitter plate as shown in Figure A1. The other end of the wing was let out of the test section, through a rotatable plexiglass window, and it was bolted at two spanwise locations as shown in Figure A4. The wing angle of attack could be chosen to be any value between -12 to +12 degrees. The cracks between the wing and this plexiglass

were filled by modeling clay. Once the wing was set at the desired angle of attack, the plexiglass was locked by use of clamps as shown in Figure A4. Throughout this study, the angle of attack and the sweep angle were set at eight and thirty-two degrees, respectively.

Splitter plate

This plate was 48.0 in. by 36.0 in., 0.50 in. thick and stood 6.093 in. above the base of the test section. The plate was screwed to the walls of the tunnel, while it was also tied down to the base by use of heavy duty wires as shown in Figure A1. Since the test section has a slight divergence, two removable tapered bars (for 32 degrees sweep) were screwed to each side of this plate. The removal of these bars would allow the plate to move along the base, and as a result the sweep angle could be chosen to be any value between 0 to 40 degrees.

The wing at its three-dimensional section went through a circular cut through the splitter. The center of this circle is located at 9.0 in. from the front and 18.0 in. from either side of the plate, and has a diameter of ≈ 16.0 in. The open area between the wing and the plate was covered with 3/16 in. thick plates (these plates were screwed to the lower surface of the splitter plate) and the cracks were filled by modeling clay and tape.

Fin configurations

The fin configurations were mounted at approximately the middle of the upper surface. The planform configurations are shown in Appendix B. Some of the fins were attached to the wing by screws at their bases as shown in Figure A5 (note that these fins were graduated in intervals of one, two and five degrees and are fins #9a, #9b, #9c, #9d, #9e, #10a, #10b, #10c, #10d, #2e and #2f). Since the rest of the fins did not have flat bases, they were attached to a circular brass plate through the slit available at the central base of each fin. A fastening pin was then pushed through the fin and the plate. Figure A6 shows how fin #2a is attached to the brass plate. A pin at the center base of the brass plate was set in a small hole on the wing. Therefore, the plate was rotatable about its center while holding the same position on the wing. Once the desired angle of attack was reached, the brass plate (this plate was graduated in intervals of one, two and five degrees), was fastened to the wing by means of screws, through the slits between the circumference and the center of the plate. Figure A7 shows fin #2a at $\alpha_F = 20°$.

Modeling clay was used to fill in the cracks between the fins and the wing curvature and, also to smooth the rough edges as shown in Figures A5 and A7. The brass plate was approximately 2.4 in. in diameter and 1/32 in. thick.

Figures A8 through A19 are pictures of the families of tested fin configurations.

Measuring devices

A four blade zero pitch rotor was mounted on the traverse system as shown in Figures A2 and A21 (blade area = 1.5 x 2 in.^{2} and rotor diameter = 3.0 in). A stroboscope, focused on the rotor, measured the angular velocity due to the fin generated circulation.

The rolling moment of the generated vortex on the following model was measured by a Boeing force balance. The balance was mounted on the traverse system as shown in Figure A20. The dimensions of the following model are given in Table 1. A number 2300 four channel, strain gage conditioning amplifier made by Vishay Instruments, was used to excite and amplify the X, Z, L and M components. The amplified output (A.F. = 1000) was measured using digital voltmeters. The Y and N arms were excited by use of a D.C. amplifier and the corresponding outputs were measured using a dial microvolt-meter.

Table 1. Dimensions of model

b = 4.563 in.
c = 0.875 in.
AR = 5.21
α = 0.00°
wing section is a NACA 0012

Experimental Procedure

Visualization technique

The approximate location of the center of the vortices were observed, when steam and/or liquid nitrogen was inserted into the test section. Figure A21 shows the center of the vortex shed by fin #9b at α_F = 7 degrees. However, as clear as it shows in this figure, it was not possible to observe the exact position of the center line of any vortex during the experiment. Once the vicinity of the vortex center was located, then the measuring devices were traversed in that vicinity until the exact location (i.e., the maximum response) was found.

Measurements

The fin families #1 through #11 were originally tested using the rotor as the measuring element. Each fin was first examined at an arbitrary angle of attack. Then, the angle of attack was increased and/or decreased at intervals of 2° and/or 5°, until stall was either reached and/or past. The more promising fins were tested again at intervals of 1°.

For comparison purposes, a Boeing force balance was used to measure the rolling moment. Thirteen of the better fins and one of the poor ones were tested again. An additional triangular fin #12a was also tested. The rest were not examined for the second time.

Tunnel velocity

The maximum velocity of about 250 ft/sec was obtainable. However, almost all of the fins were tested at velocities between 20.0 to 110.0 ft/sec. Occasionally, the velocity had to be increased up to about 100.0 to 200.0 ft/sec. This was only necessary in case of the poorer fins, when the measuring devices signals were very small or produced no response at all.

CHAPTER III. RESULTS AND DISCUSSION

Vortex Strength Terms

Angular velocity

The vortex strength design parameter $\frac{\Gamma}{V_\infty\sqrt{S_F}}$, has been chosen as figure of merit. In order to minimize fin area and thus weight, it is desirable to maximize the figure of merit. According to Stokes theorem the circulation Γ is defined as $-\Gamma = \oint_C \vec{V}\cdot d\vec{\ell} = \iint_{\hat{S}} \nabla \times \vec{V} \cdot \vec{n}\, d\hat{S}$. Since vorticity $\nabla \times \vec{V}$ is proportional to the angular velocity of the fluid particles, the product of the rotor frontal disc area times the rotor angular speed should be proportional to the above area integral and therefore, the circulation strength (i.e., $\Gamma \propto \omega\, S_R$) where ω and S_R are the rotor angular speed and disc area, respectively. Therefore, for any size rotor diameter, the vortex strength term $\frac{\Gamma_0}{V_\infty\sqrt{S_F}}$ is proportional to $\frac{\omega S_R}{V_\infty\sqrt{S_F}}$.

The plots of the rotor angular velocity versus the free stream velocity at particular angles of attack, provide the ratio $\frac{\omega}{V_\infty}$. Figure A22, A23, A24, and A25 are examples of plots. The slope $\frac{\omega}{V_\infty}$ increases with the angle of attack up to a maximum value. After stall, this ratio starts to decrease. These lines are supposed to go through the origin but because of the rotor bearing friction, the rotation of the blades starts when velocity is somewhere between 10 to 30

ft/sec, therefore moving the intersection to a point other than the origin, as shown in Figures A24 and A25.

Appendix C tabulates the $\frac{\omega}{V_\infty}$ slopes in Table C1 for the tested fins at the corresponding angles of attack, areas and aspect ratio.

Rolling moment

The figure of merit for the rolling moment measurements is chosen to be the same term $\frac{\Gamma}{V_\infty \sqrt{S_F}}$ as before. However, it is shown in Appendix D that $\frac{\Gamma}{V_\infty \sqrt{S_F}}$ is in this case proportional to $\frac{c_\ell b}{\sqrt{S_F}}$ for a Rankin vortex. It is also shown that the above term is directly proportional to $K_3 \frac{S_F}{b_F} [\frac{1}{2} - \frac{2}{3} K_2 \frac{b_F}{b}]$ where K_2 and K_3 are constants. Therefore, the term $\sqrt{S_F}$ should be approximately equal for all of the fin configurations so that the best shape between equal area fins can be found.

The six force and moment components in the wake, measured by the force balance are tabulated in Appendix C and Table C2.

Optimum Configuration

Rectangular plan-forms with triangular trailing edges

This configuration is family #1 of Appendix B. These fins were tested only with the rotor. Figure A26 shows that the optimum aspect ratio for this shape is between fin #1a and #1d with the value of $AR_{OF} \approx 0.5$ and the maximum vortex term

of about 0.035. The optimum fin of this family, should have an angle of attack in the range $15° \lesssim \alpha_{OF} \lesssim 19.5°$ as can be seen from Figure A28. These fins have equal thickness and similar edge conditions.

Parabolic fins

The parabolic configurations which were first tested with the rotor (i.e., fins #2a, #2b, #2c, and #2d) showed very promising characteristics. The optimum aspect ratio from the rotor results for this configuration is about an $AR_{OF} \approx 0.594$ at an optimum angle of attack $17° < \alpha_{OF} < 19°$ as can be seen from Figures A29 and A30. These fins were tested again with the force balance. Figures A31 and A32, which correspond to the balance measurements, outline the optimum aspect ratio of about $AR_{OF} \approx 0.585$ and α_{OF} between $18.5° < \alpha_{OF} < 21°$. The results mentioned so far are only for the parabolic fins of similar edge and thicknesses. Using these guidelines, three fins with sharp edges and different thicknesses were built (i.e., #2e, #2f and #2g). These fins have the same planform dimensions of fin #2b, since this fin is very close to or perhaps is the optimum size and shape.

It is found that for a flat (i.e., 0.0625 in. thick) parabolic fin with sharp edges (i.e., fin #2e) the maximum vortex strength due to angular velocity is less than that

with smooth edges and $t_{F_{MAX}}$ = 0.25 in. (i.e., fin #2b). Whereas, the rolling moment measurements indicate sharp edges increase the maximum vortex term as can be seen from Figures A29 and A31. Therefore, at this point it is not clear how edge condition affects the strength of the shed vortex although, it is known that, in general, the leading edge vortex increases as edge sharpness increases. However, it is certainly clear from Figures A29 and A31 that fin #2f which is a 5% circular section and is 0.0625 in. thick, is a definite improvement over fin #2b. On the other hand, the rotor and the balance data disagree on fin #2g which is a 5% thick circular section. The optimum angle of attack seems to be not affected by edge conditions. As Figures A30 and A32 show fins #2b and #2c have almost the same optimum angles of attack. The 5% thick cambered fin #2g seems to stall at higher angles than fin #2b, whereas fin #2f stalls earlier. The maximum vortex strength terms of $\frac{\omega S_R}{V_\infty \sqrt{S_F}}$ = 0.107 and $\frac{c_\ell b}{\sqrt{S_F}}$ = 0.1532 were obtained for fin #2f. These values are quite high compared with most of the fins tested during this study.

Trapezoidal fins with swept leading edge

These are fin family #3 of Appendix B. The angular velocities of all fins of this family were tested. However, the rolling moment of only one (i.e., fin #3a) was measured. The optimum aspect ratio for this family can not be predicted

from the available data. As can be seen from Figure A26, the optimum aspect ratio is somewhere between $0 < AR_{OF} < 0.4$, whereas the optimum angle of attack from Figure A33 is greater than or equal to 19°. All the members of this family have similar edge and thickness conditions. The maximum vortex strength term of $\frac{\omega S_R}{V_\infty \sqrt{S_F}} = 0.08$ and $\frac{c_\ell b}{\sqrt{S_F}} = 0.132$ was obtained for fin #3a from Figures A26 and A34.

Parabolic fins with triangular trailing edge cutouts

Family #4 of Appendix B fits this description. The rotor data indicate that the optimum aspect ratio for this family is $AR_{OF} = 0.875$ at an optimum angle equal to ≈21° as shown in Figures A26 and A27. The rolling moment strength terms of Figures A34 and A35 only confirm that fin #4b is closer to the optimum shape than #4a (since these are the only two which were tested with the balance). The maximum vortex terms obtained are $\frac{\omega S_R}{V_\infty \sqrt{S_F}} = 0.077$ and $\frac{c_\ell b}{\sqrt{S_F}} = 0.128$ for fin #4b.

Semi-elliptic fins

These fins are members of family #5 of Appendix B. As can be seen from Figure A26, the optimum aspect ratio for this family is not found. However, because of the resemblance with family #2, one might expect the optimum aspect ratio of about 0.5 to 0.7 and angle of attack larger than 15°

for optimum vortex strength injection. For fin #5a, the maximum vortex strength of $\frac{\omega S_R}{V_\infty \sqrt{S_F}} = 0.068$ occurred at 14° as shown in Figure A36. However, since the optimum fin in this family should be smaller than #5a (as far as aspect ratio is concerned), its optimum angle of attack has to be larger than 14°. This family was not tested for rolling moment measurements.

Elliptic fins

All of the elliptic fins of family #6 have been tested with the rotor. Only one fin (i.e., fin #6a) was investigated using the force balance. Figure A26 indicates that optimum aspect ratio for elliptic fins has to be smaller than 0.50, while Figure A37 shows the optimum angle of attack larger than 20°. The rolling moment results indicate that fin #6a has an optimum angle at 17.80° as shown in Figure A34 while the rotor velocity shows stall angle larger than 20° in Figure A37. Therefore, it is not clear what the optimum angle range is. One might suggest the following range $16° \leq \alpha_{OF} \leq 23°$. The maximum rolling moment and the angular velocity strength terms for fin #6d are 0.12 and 0.0732, respectively.

Semi-circular fins

This is the shape of family #7 of Appendix B. There are only two fins with this particular shape. The rotor results in Figure A26 indicate that the optimum fin aspect ratio has not been found. This aspect ratio is perhaps smaller than 1.90 as shown in Figure A26. Figure A39 shows that the optimum angle of attack is perhaps larger than 7°. Fin #7b is the one closer to the optimum and has the maximum vortex term of $\frac{\omega S_R}{V_\infty \sqrt{S_F}} = 0.0575$ and $\frac{c_\ell b}{\sqrt{S_F}} = 0.082$. The rolling moment results of Figure 34 show that fin #7b stalls at about 2.5°. It is therefore not certain what the limit is on choices of angle of attack. It is reasonable to choose the range $2° \leq \alpha_{OF} \leq 10°$.

Rectangular fins with semi-circular leading edges and semi-rectangular circular trailing edges

As shown in Appendix B these are fins of family #8 tested during this study. The angular velocity measurements of these fins as shown in Figures A40 and A41 do not give a clear picture of what the optimum aspect ratio and angle of attack ought to be. As shown in Figure A40, it is hard to believe that a family of fins would have optimum size at two different aspect ratios (i.e., one optimum aspect ratio between fins #8e and #8c and the other smaller than #8b). However, this type of behavior could be due to two opposite

sign vortices injected from each corner of the semi-triangular trailing edge of these fins.

Circular fins

Family #9, as shown in Appendix B, are circular planform fins. The angular velocity measurements as shown in Figure A40 and A43 were taken for all members of this family. The comparison of vortex term $\frac{\omega S_R}{V_\infty \sqrt{S_F}}$ between those members with approximately equal areas (this excludes fin #9b and #9c which are about 3.5 $in.^2$ smaller) indicates the following: First, it is observed that sharp edges and the smaller thickness (i.e., 0.0625) of fin #9e has decreased the maximum vortex term by 0.012 relative to fin #9g which is 0.25 in. thick and has smooth edges. Second, on the other hand, the 5% thick circular fin #9f with sharp edges has larger maximum vortex term than fin #9g. Further, it is observed that fin #9c and #9a with GA(W)-2 and Clark-Y sections, respectively, are better configurations. Rolling moment measurements of #9a and #9c confirmed that indeed the fin with Clark-Y section sheds a stronger maximum vortex than that with GA(W)-2 section as shown in Figures A40 and A34. This is consistent with Rossow's (23) results.

As mentioned before, the fins with smaller areas (i.e., fins #9b and #9d) are not to be compared (look in Appendix D) with the rest of the fins in this family, for the constants

K_3 and K_2 of Equation D14 in Appendix D are not known. Note that the maximum $\frac{c_\ell b}{\sqrt{S_F}}$ obtained for fin #9b has been found to be ≈0.15 at 11°. Whereas the maximum occurs at 15° for the rotor. The optimum angles of attack of #9b and #9d are not in agreement between the tests.

Rectangular fins with flaps

Appendix B has the shapes and dimension of these fins. Figures A40 and A42 show that the optimum aspect ratio for these fins has to be $AR_{OF} \leq 0.35$ while the optimum angle of attack is perhaps $\alpha_{OF} \geq 13°$. The maximum value of $\frac{\omega S_R}{V_\infty \sqrt{S_F}} \geq 0.073$ is obtainable for this configuration. This family was tested for angular velocity observations only.

Parabolic fins with semi-triangular trailing edge

Fin #11a is the only one which has this shape. It is found to have an optimum angle of attack of 18.25° with the maximum strength term $\frac{\omega S_R}{V_\infty \sqrt{S_F}} = 0.044$. It is assumed that two vortices are injected from this fin, one from the tip and the other from the corner of the parabola and the semi-triangle. Since both are in the same direction, therefore, it might be assumed that the resultant vortex should be quite strong. Apparently, for this aspect ratio (i.e., $AR_F = 1.57$) this is not so. Other aspect ratios should be tested so this could be either confirmed or denied.

Triangular fins

The triangular fin #12a was tested for rolling moment measurements. The aspect ratio of this fin is $AR_F \approx 0.80$ and has maximum $\frac{c_\ell b}{\sqrt{S_F}} \approx 0.125$. Figure A34 shows the optimum angle of attack $\alpha_{OF} \approx 20°$ was reached. Unfortunately, no outline for optimum aspect ratio and angle of attack can be given since this is the only triangular fin tested.

General discussion

Iversen (22) based on estimated vortex term $\frac{\Gamma}{V_\infty \sqrt{S}_{WING}}$ has presented a plot of estimated values $\frac{\Gamma}{V_\infty \sqrt{S}_{WING}}$ V.S. α_{WING} for wings of aspect ratio ≈1.0. Figure A6 of reference 22 shows this plot. This figure indicates that between semi-eliiptic, gothic, square, elliptic and delta wings the best one is the semi-elliptic shape. The second is shown to be the gothic while the third is the square wing. The elliptic configuration is shown to be better than the delta for angles of attack smaller than ≈38° and obtain the forth rank after the square wing.

For aspect ratio equal to one the following table is obtained from Figures A26, A29 and A40.

Table 2. Comparison of maximum vortex term $\frac{\omega S_R}{V_\infty \sqrt{S_F}}$ between configurations with aspect ratio ≈1.0

	$[\frac{\omega S_R}{V_\infty \sqrt{S_F}}]_{max}$	Family #
Semi-elliptic	0.070	#5
Parabolic/Gothic	0.085	#2
Square	0.057	#10
Elliptic	0.040	#6

According to the above table parabolic fins are better vortex generators at $AR_F \approx 1.0$. Semi-elliptic has the second best position while square and elliptic are third and fourth, respectively. The quality of delta fin with $AR_F \approx 1.0$ is not predictable from the available data. Although Figure A6 of reference 22 disagrees with the semi-elliptic and parabolic comparisons obtained during the present study, it agrees with that of square and elliptic configurations. Since the effective angles of attack are plotted in Figure A6 of reference 22, there are no exact comparisons possible for angle of attack between Figures A6 and the results of this study.

Figures 4 and 5 of reference 22 show that rectangular configurations have an optimum aspect ratio less than 0.10 and 0.8, respectively. It was found during this study that

rectangular fins should have aspect ratios less than or equal to 0.35 as shown in Figure A40 for family #10. Rossow (16), however, has found that an aspect ratio of 0.333 is more likely the optimum for this configuration.

From the lift coefficient vs. angle of attack plots of reference 24 it can be seen that between gothic and delta wings of equal or approximately equal aspect ratios the gothic planforms have higher lift curve slopes. The results of the present study show that the triangular fin #12a is poorer than the parabolic fin #2d which has approximately the same aspect ratio.

The effect of trailing-edge sweep on lift of gothic wing with aspect ratio equal to one is shown in Figure A47 of reference 24. It seems that in general, positive sweep increases the lift coefficient. Configuration family #4 is very similar to this shape. However, the results have shown that this shape is not any better than plain parabolic, but yet is even worse. The members of family #1 have also swept trailing edges. Compared with fins #10 which are also rectangular but have no trailing edge sweep, family #1 fins have not performed well. The strength of the vortices shed by fins with swept trailing edges are related to their lift coefficient in a more complicated fashion. For example, it is very possible that the wake of such configurations is a region of two oppositely signed vortices.

In reference 25 it is concluded that a gothic wing of aspect ratio 1.0 has a better lift and drag characteristics than a delta wing with the aspect ratio of 1.0. While it is also shown in Figures A36 and A31 that at AR ≈ 0.8, the parabolic configuration is more likely better than the delta.

Vortex breakdown phenomenon is one concept which ought to be understood, in particular when fin vortices are being studied. The observations made by Lambourne and Bryer (26) for a flat-plate delta wing tested in water tunnel describes the breakdown of the leading edge vortex in three stages. First, the flow along the axis of the normal vortex decelerates. Second, the vortex, takes a shape of a spring and whirls about the vortex axis. Finally, the breakdown of the filament occurs.

In the work done by Wentz and Kohlman (27) it is shown that breakdown at the trailing edge of some delta wings with various sweep angles occurs at relatively low angles ot attack (13° to 40°), while the breakdown at the apex occurs at angles of attack close to or even past the stall (30° to 70°). Further, the breakdown angle of attack increases with increase of sweep angle. This in general, is in agreement with wind tunnel results published by Engler and Moss (28). At low angles of attack, for low aspect ratios, bursting of the trailing vortex occurs at some distance downstream of the trailing edge. As the angle of attack increases, the burst

point moves forward to the trailing edge, and as the angle of attack increases still further, the burst point moves forward to the apex as noted above. Actual flight observations done on the HP 115 aircraft by Fennel (29) confirm the forward progression of the burst point with increase in angle of attack.

There are no data available on breakdown of fin vortices nor were any observations made during the present study. Therefore, at low angles of attack the measuring devices could have been positioned in normal (i.e., prior to burst) vortices. Bursting at or just forward of the measurement point as fin angle increased could be a reason for the sudden decrease (sharp peaks) of $\frac{\omega S_R}{V_\infty \sqrt{S_F}}$ and $\frac{c_\ell b}{\sqrt{S_F}}$ for α_F larger than the peak value. Examples of such peaks could be observed in Figure A30 for fin #2b or Figure A32 for fins #2e, #2d and #2a. It is thus probable that peak values of $\frac{\omega S_R}{V_\infty \sqrt{S_F}}$ and $\frac{c_\ell b}{\sqrt{S_F}}$ were obtained at angles of attack below the fin stall angles.

CHAPTER IV. CONCLUSIONS AND RECOMMENDATIONS FOR FURTHER STUDY

Conclusions

The correlation between the two experimental methods as shown in Figure A44 follows the straight line $[\frac{c_\ell b}{\sqrt{S_F}}]_{max} = 0.8907[\frac{\omega S_R}{V_\infty \sqrt{S_F}}]_{max} + 0.0542$. Some of the data points in Figure A44 such as #9a, #2b, #2d, etc., show inconsistencies between the two methods. For example, fin #2b has a larger $[\frac{\omega S_R}{V_\infty \sqrt{S_F}}]_{max}$ than #2g, but the rolling moment term $[\frac{c_\ell b}{\sqrt{S_F}}]_{max}$ of #2g is larger. Since the balance was mounted at a position closer (the leading edge of the follower wing is about 3.0 in. closer to the generator than the front of the rotor) to the generator than the rotor, delay in vortex breakdown could have been one reason for this inconsistency. Noise interference could have affected the readings also. On the other hand, it should be noted that the force balance output, eventhough magnified by a factor of 1000.0, was still very small (the maximum rolling moment response of 0.060 mv was the largest rolling moment output). Therefore, for such small changes of response the accuracy of the balance readings is questionable. Note that the complex interactions between either the rotor or the balance wing and the vortex burst positions of course are not understood.

The conclusions are made as follows: the vortex strength term comparison of configurations with equal planform area, no camber, same thickness and same edge condition has suggested that the Parabolic configuration is the most successful vortex injector for wake alleviation pruposes. Figure A44 shows that family #2 which is the Parabolic configuration has demonstrated to be very promising for use as a fin vortex generator. On the other hand, fin #9a which is a circular configuration and has GA(W)-2 wing section is very close to fin #2b as shown in Figure A44. However, it should be noted that fin #2b is not cambered. Whereas when fin #2b becomes cambered (i.e., fin #2f) suddenly a big jump in vortex strength appears. It has also been observed that between circular fins (i.e., family #9) approximately equal area the flat fins have demonstrated poorly (i.e., #9e and #9g). Therefore, an optimum fin apparently should be cambered. Apparently, the Clark Y wing section is superior to GA(W)-2 wing section for circular fins of family #9. Whereas the 5% thick circular arc section of Parabolic fin #2g is not better than fin #2f (note that these fins have the same aspect ratios but #2f is a 0.0625 in. thick plate which was bent 5%).

If the optimum fin is chosen to be a cambered Parabolic fin its aspect ratio according to the results of the present study should be in the range $0.5 \leq AR_{OF} \leq 0.7$ as can be seen from Figures A29 and A31. The angle of attack as

defined in this study of such a highly cambered and low aspect ratio fin has to be in the range $13° \leq \alpha_{OF} \leq 16°$ as can be seen from Figures A30 and A32. Any fin configuration other than Parabolic would have low optimum aspect ratio and high optimum angle of attack for optimum vortex injection purposes.

Recommendations for Further Study

For further optimum fin search purposes, the following suggestions are recommended:

1. Many other configurations (any reasonable shape that one might think of) ought to be tested.

2. Camber and edge effects on the strength of the injected vortex should be carefully studied for a few different planforms.

3. An experimental approach should be taken towards seeking the position of vortex breakdown in wakes of fin configurations.

4. The effects of the generator angle of attack on the strength in the wake should be determined.

5. Eventually, the effects of fin spanwise blowing and multiple fin performance should be studied.

6. Once a particular fin or fin combination is selected as optimum (i.e., injects the strongest vortex), then its best

position on the generator must be found for each airplane configuration in question.

7. For practical applications, the performance penalties (mostly drag penalties) ought to be known in more detail, for an optimum fin is not only the best vortex generator but is also the one with smallest detriment to aircraft performance.

REFERENCES

1. Proceedings of NASA Symposium on Wake Vortex Minimization, NASA SP-409, 1976.

2. B. W. McCormick. "Aircraft Wakes: A Survey of the Problem." Presented at FAA Symposium on Turbulence, Washington, D.C., March 22-24, 1971.

3. D. D. Thomas. "Turbulence Related Accidents, Worldwide Synopsis." Presented at FAA Symposium on Turbulence, Washington, D.C., March 22, 1971.

4. A Gessow. "Aircraft Wake Turbulence Minimization by Aerodynamic Means." Proceedings of the 6th Conference on Aerospace and Aeronautical Meteorology, El Paso, Texas, Nov. 12-14, 1974.

5. J. J. Tymczyszyn and M. R. Barber. "A Review of Recent Wake Vortex Flight Tests." Proceedings of the 18th Annual Symposium of Society of Experimental Test Pilots, Los Angeles, Calif., Sept. 26 (1974), 52-68.

6. V. J. Rossow. "Inviscid Modeling of Aircraft Trailing Vortices." Proceedings of NASA Symposium on Wake Vortex Minimization, NASA SP-409 (1976), 4-54.

7. V. J. Rossow. "Convenctive Merging of Vortex Cores in Lift-Generated Wakes." Journal of Aircraft, 14, March (1977), 283-290.

8. V. J. Rossow. "Theoretical Study of Life-Generated Vortex Wakes Designed to Avoid Roll-Up." AIAA Journal, 13, No. 4 (1975), 476-484.

9a. S. A. B. Brandt and J. D. Iversen. "Merging of Aircraft Trailing Vortices." AIAA Journal of Aircraft, 14, No. 12 (1977), 1212-1220.

9b. V. R. Corsiglia, K. L. Orloff and J. D. Iversen. "Laser-Velocimeter Surveys of Merging Vortices in a Wind Tunnel." AIAA Paper 78-107, Jan. 1978.

10. P. Raj and J. D. Iversen. "Computational Studies of Turbulent Merger of Co-Rotational Vortices." AIAA Paper 78-108, Jan. 1978.

11. J. E. Hackett and P. F. Evans. "Numerical Studies of Three-Dimensional Breakdown in Trailing Vortex Wakes." AIAA Journal of Aircraft, 14, No. 11 (1977), 1093-1101.

12. V. R. Corsiglia, V. J. Rossow and D. L. Ciffone. "Experimental Study of the Effect of Span Loading on Aircraft Wakes." AIAA Journal of Aircraft, 13, No. 12 (1976), 968-973.

13. D. L. Ciffone. "Vortex - Interactions in Multiple Vortex Wakes Behind Aircraft." AIAI Journal of Aircraft, 14, No. 5 (1977), 440-446.

14. D. L. Ciffone and B. Pedley. "Measured Wake Vortex Characteristics in Ground Effect." AIAA Paper 78-109, Jan. 1978.

15. A. J. Bilanin, M. E. Teske, and J. E. Hirsch. "The Role of Atmospheric Shear, Turbulence and a Ground Plane on the Dissipation of Aircraft Vortex Wakes." AIAA Paper 78-110, Jan. 1978.

16. V. J. Rossow. "Effect of Wing Fins on Life-Generated Wakes." AIAA Journal of Aircraft, 15, No. 3 (1978), 160-167.

17. D. R. Croom. "Low-Speed Wind-Tunnel Investigation of Various Segments of Flight Spoilers as Trailing-Vortex-Alleviation Devices on a Transport Aircraft Model." NASA TH D-8162, 1976.

18. D. R. Croom. "Evaluation of Flight Spoilers for Vortex Alleviation." AIAA Journal of Aircraft, 14, No. 8 (1977), 823-825.

19. V. R. Corsiglia and V. J. Rossow. "Wind-Tunnel Investigation of the Effect of Porous Spoilers on the Wake of a subsonic Transport Model." NASA TM X-73, 091, 1976.

20. J. C. Patterson, Jr. and F. L. Jordan, Jr. "Thrust Augmented Vortex Attenutation." Proceedings of NASA Symposium on Wake Vortex Minimization, NASA SP-409 (1976), 258-274.

21. M. R. Barber, E. C. Hastings, Jr., R. A. Champine and J. J. Tymczyszyn. "Vortex Attenuation Flight Experiments." Presented at NASA Wake Vortex Minimization Symposium, Washington, D.C., Feb. 1976.

22. J. D. Iversen. "Review of the Boeing Wake Technology Program." Boeing Document No. D6-46966TN, Dec. 1978.

23. V. J. Rossow. "Experimental Investigation of Wing Fin Configurations for Alleviation of Vortex Wakes of Aircraft." NASA Technical Memorandum 78520, Nov. 1978.

24. D. H. Peckham. "Low-Speed Wind-Tunnel Tests on a Series of Uncambered Slender Pointed Wings with Sharp Edges." Communicated by the Deputy Controller Aircraft (Research and Development), Ministery of Supply, Reports and Memoranda No. 3186, 1958.

25. D. H. Peckham and S. A. Atkinson. "Preliminary Results of Low Speed Wind Tunnel Tests on a Gothic Wing of Aspect Ratio 1.0." Aeronautical Research Council Technical Report, No. 508, 1960.

26. N. C. Lambourne and D. W. Bryer. "The Bursting of Leading-Edge Vortices - Some Observations and Discussion of the Phenomenon." Aeronautical Research Council Technical Report, No. 3282, 1962.

27. W. H. Wentz Jr. and D. L. Kohlman. "Vortex Breakdown on Slender Sharp-Edged Wings." AIAA Journal of Aircraft, 8, No. 3 (1971), 156-161.

28. P. B. E. Engler and G. F. Moss. "Low-Speed Wind-Tunnel Tests on a 1/8th Scale Model of the Handley-Page HP 115." R.A.E. Technical Report, Report and Memoranda No. 3486, 1965.

29. L. J. Fennel. "Vortex Breakdown - Some Observations in Flight on the HP .115 Aircraft." R.A.E. Technical Report, Report and Memoranda No. 3805, 1971.

30. K. Karamcheti. Principles of Ideal-Fluid Aerodynamics, New York: John Wiley and Sons, Inc., 1966.

ACKNOWLEDGMENTS

The author wishes to express appreciation and gratitude to Dr. J. D. Iversen for his guidance and suggestions during this study. Also, I would like to acknowledge Dr. C. T. Hsu, Dr. L. K. Severside, and Dr. F. M. Graham for serving as committee members and to Mrs. Pat Gunnells for typing this thesis.

APPENDIX A: FIGURES

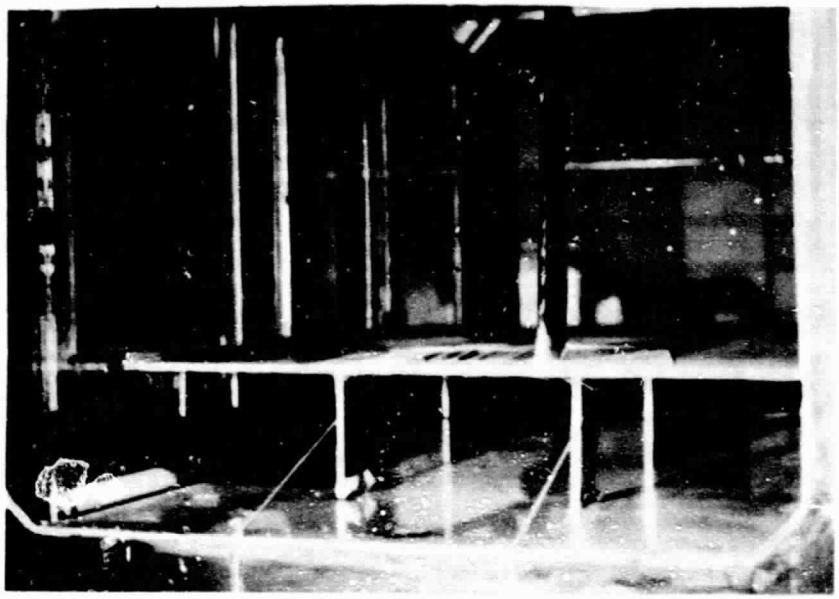

Figure A1. The frontal view of the test section. The two-dimensional wing is mounted at an angle of attack of 8^{o} and a sweep angle of 32^{o}

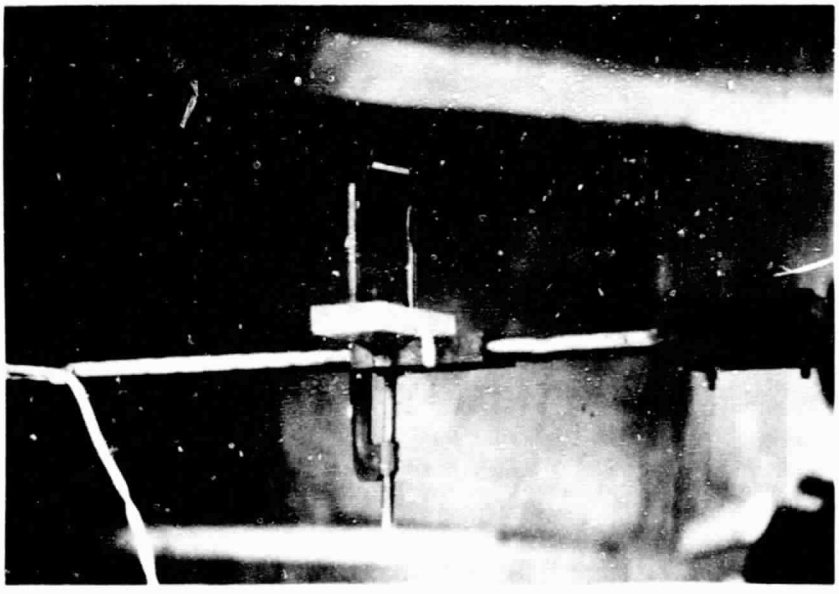

Figure A2. The four blade rotor mounted on the traverse system. The traverse system moves the measuring devices in a two-dimensional plane perpendicular to the free stream velocity

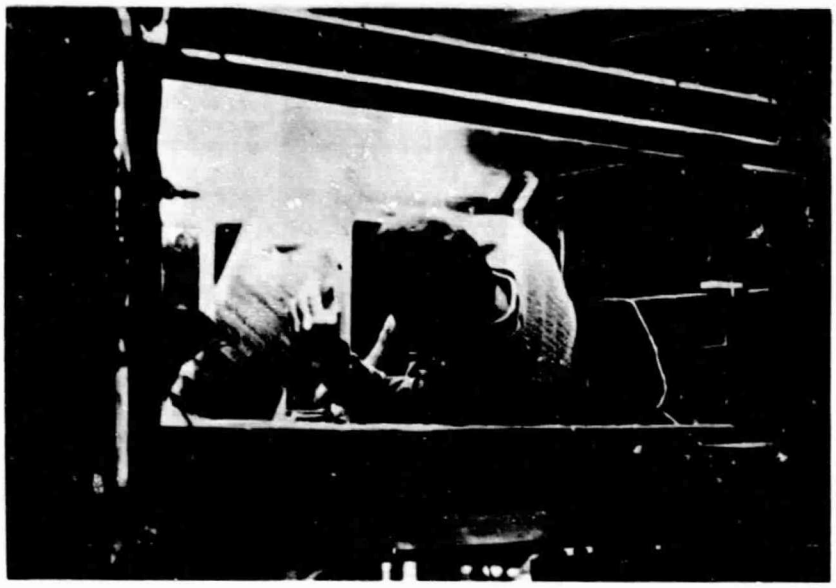

Figure A3. Fin #9b is being mounted on the upper surface of the wing at $\alpha_F = 7^o$

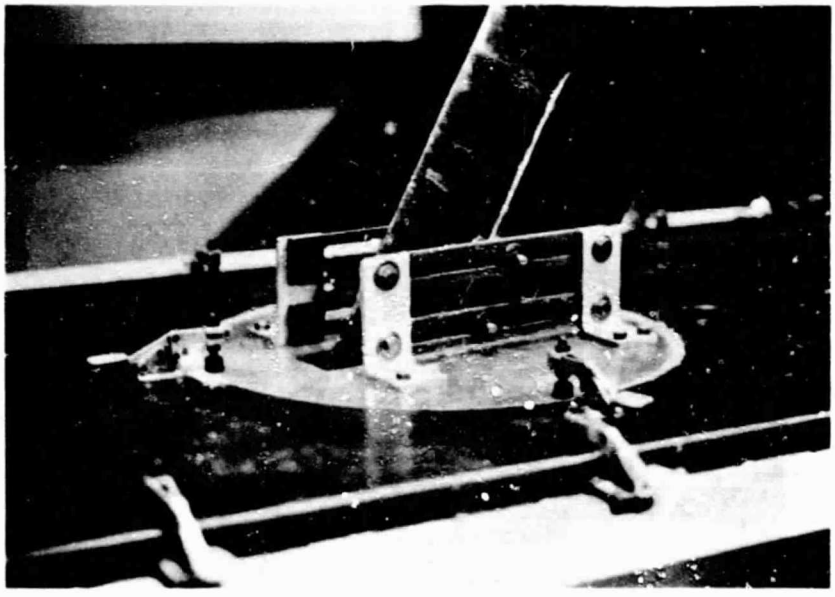

Figure A4. The wing was held tight enough so that the aerodynamic forces and moments were not able to change the wing angle of attack and/or the sweep angle

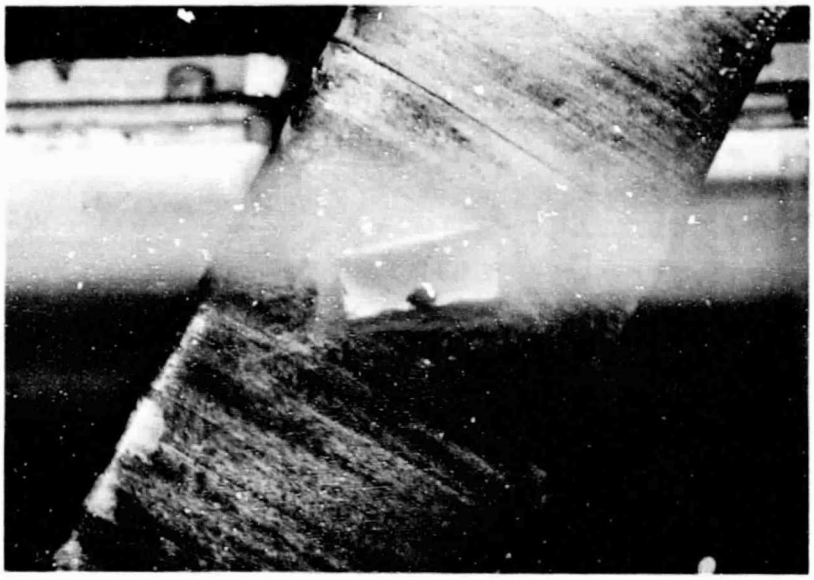

Figure A5. Fin #9b at $\alpha_F = 7^o$ is attached to the wing by one screw at its base (the screw is hidden under clay)

Figure A6. Fin #2a is attached to the graduated brass plate

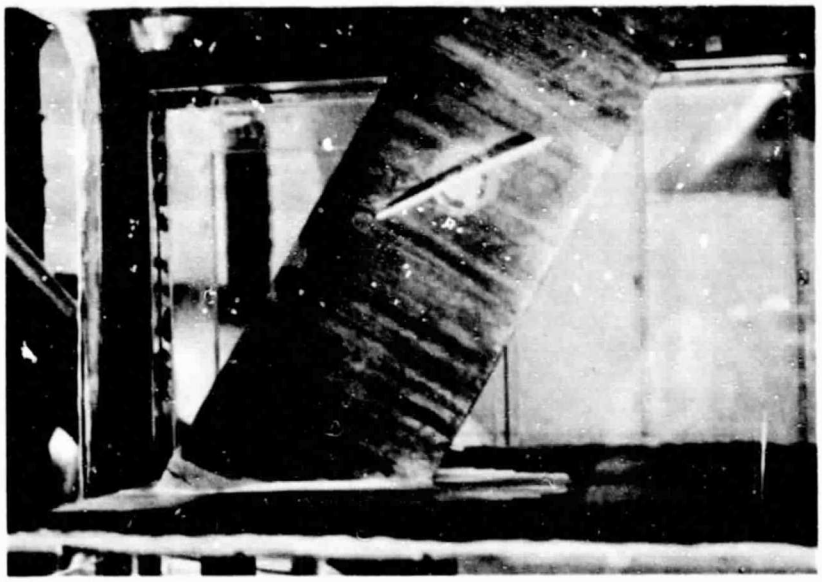

Figure A7. Fin #2a at $\alpha_F = 20^o$ is attached to the wing by use of the rotatable brass plate

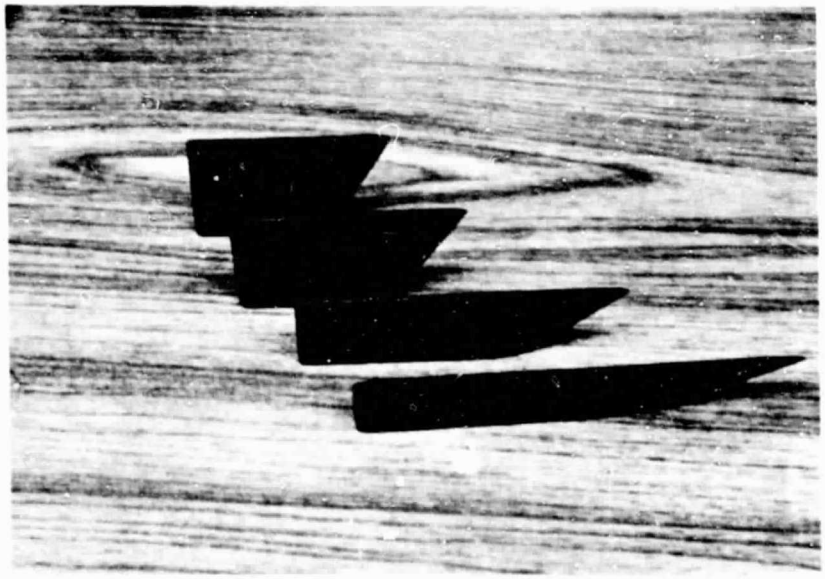

Figure A8. Tested members of fin family #1.

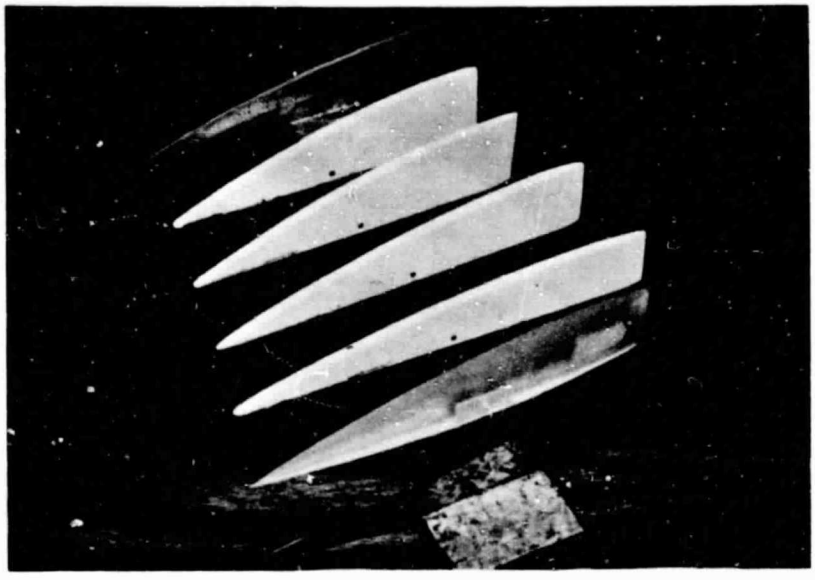

Figure A9. Tested members of fin family #2

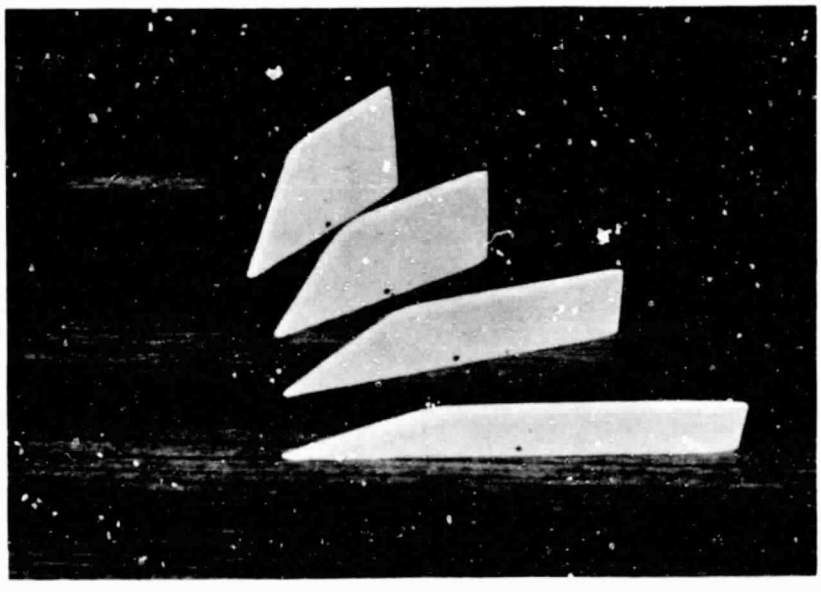

Figure A10. Tested members of fin family #3

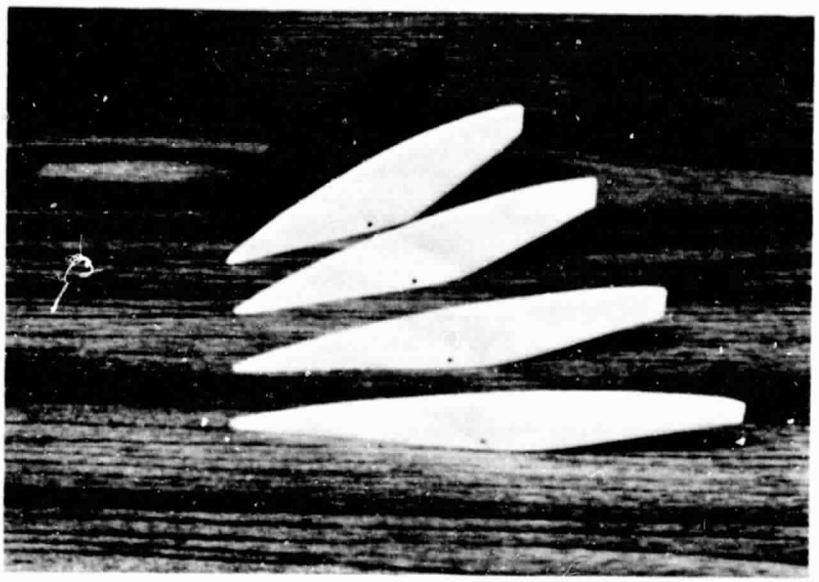

Figure A11. Tested members of fin family #4

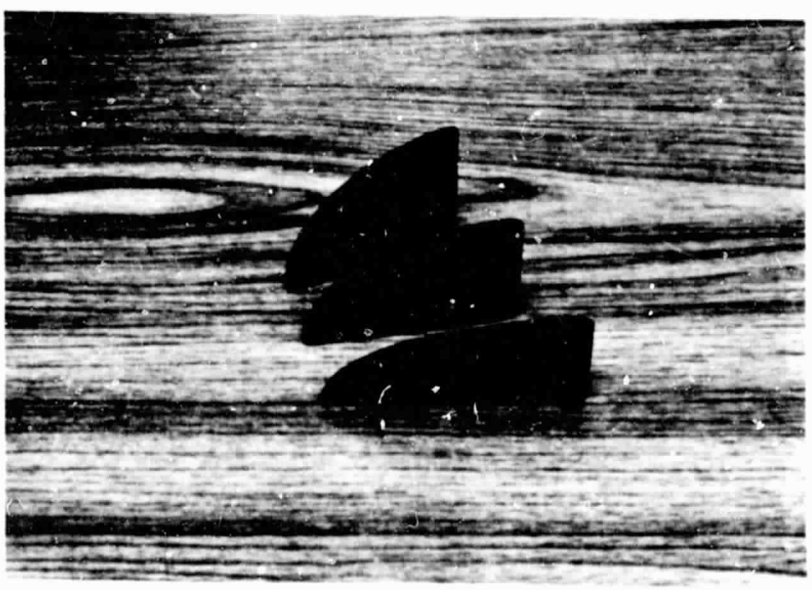

Figure A12. Tested member of fin family #5

Figure A13. Tested members of fin family #6

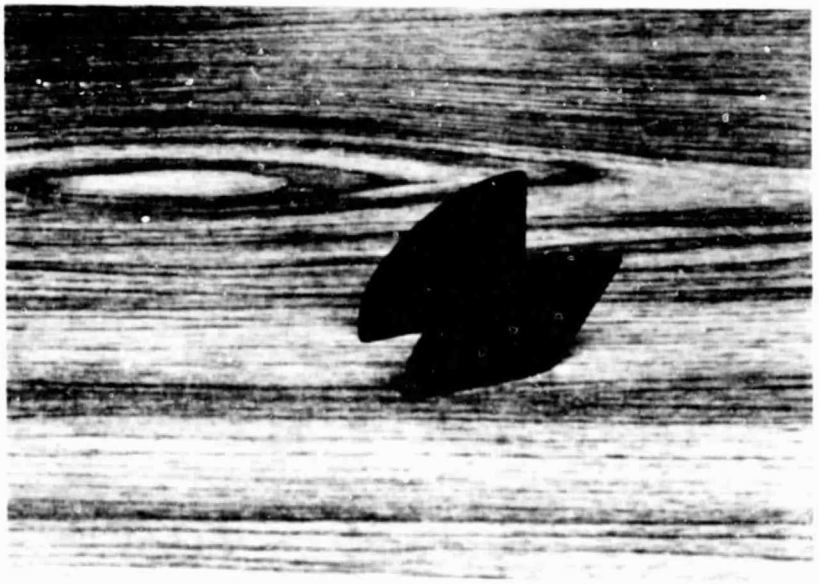

Figure A14. Tested members of fin family #7

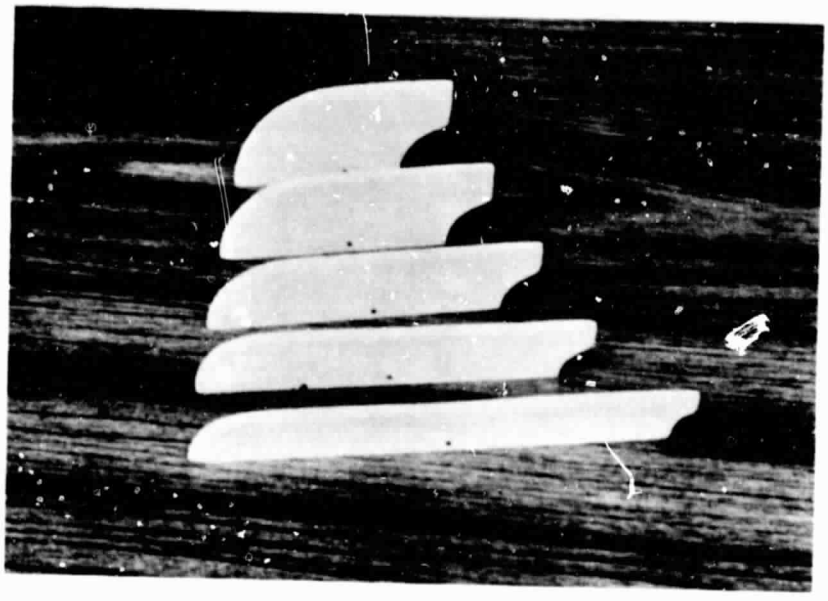

Figure A15. Tested members of fin family #8

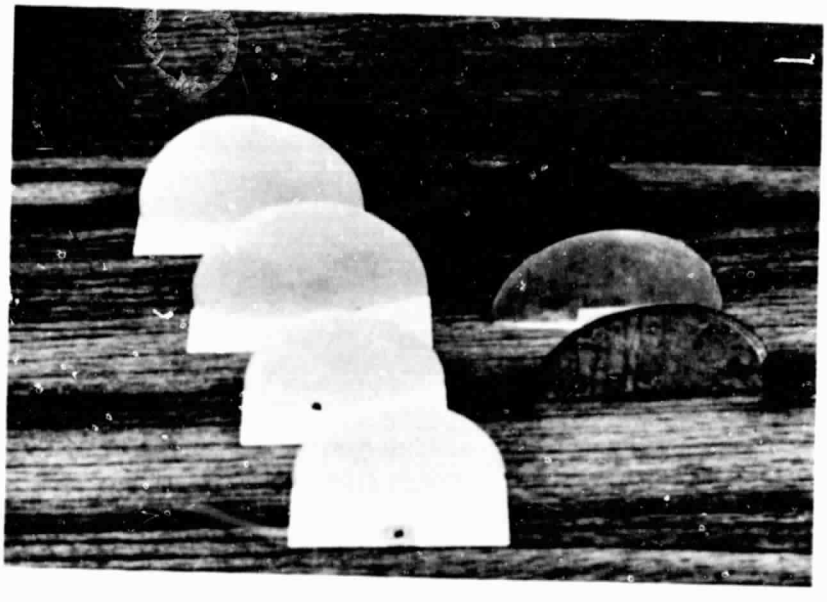

Figure A16. Tested members of fin family #9

Figure A17. Tested members of fin family #10

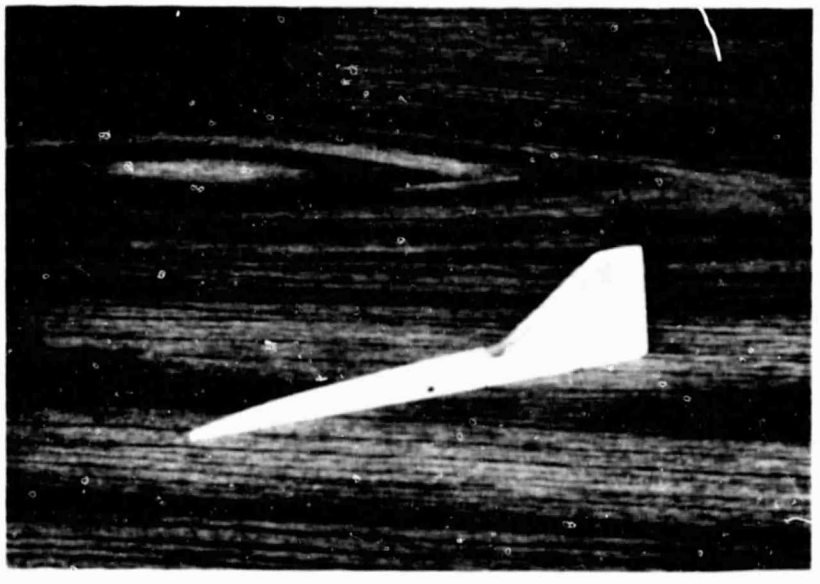

Figure A18. Tested member of fin family #11

Figure A19. Tested member of fin family #12

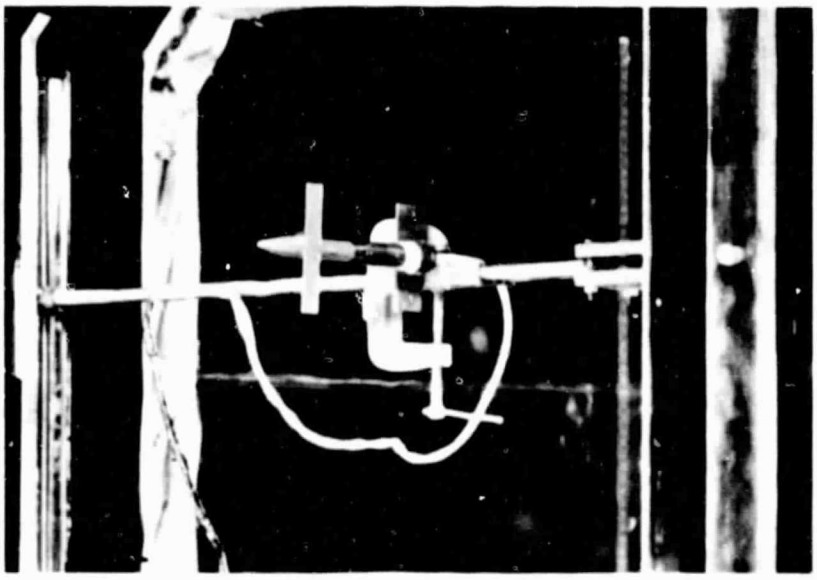

Figure A20. The balance/follower model is mounted on the traverse system. This model is set at zero angle of attack relative to the free stream velocity

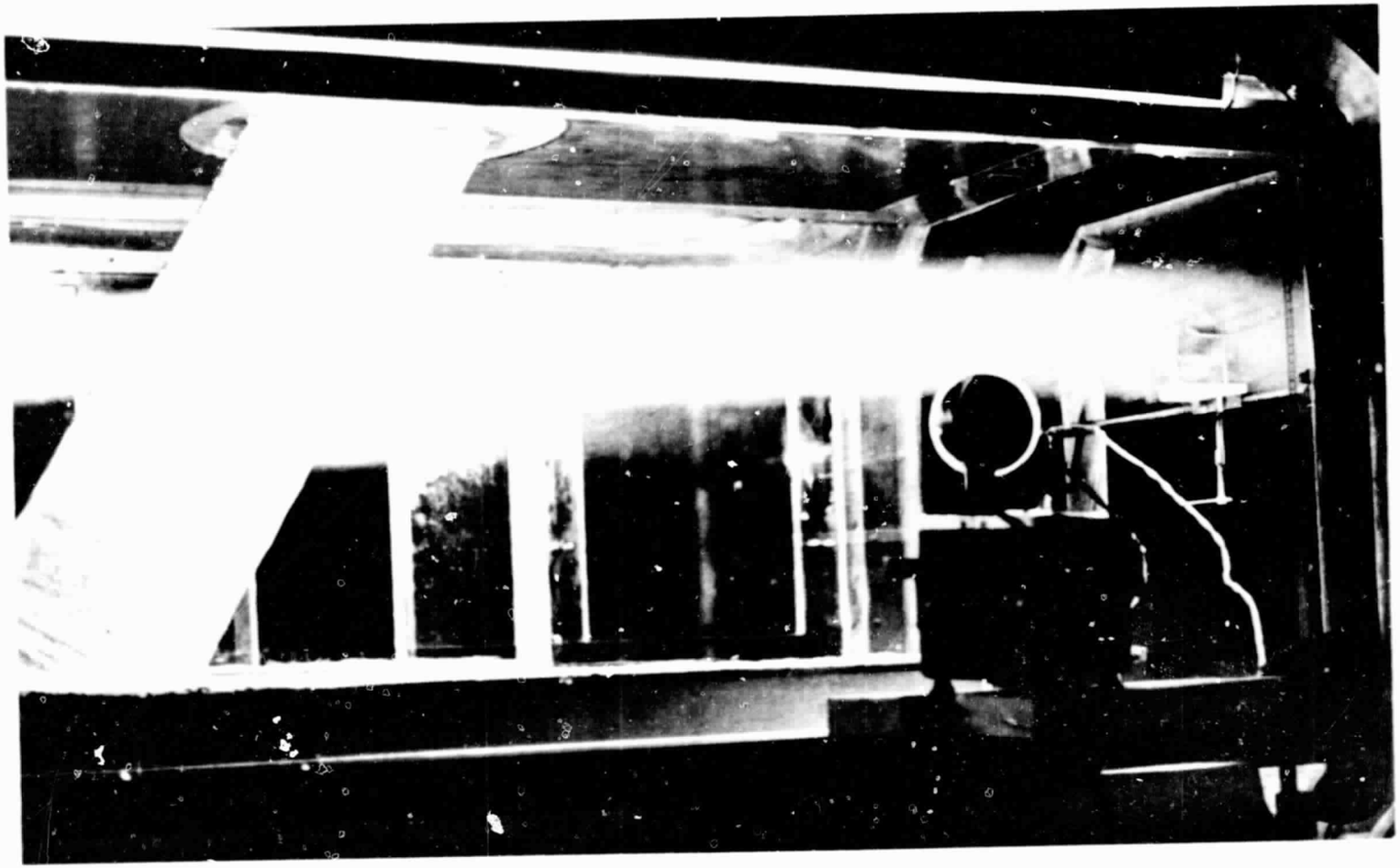

Figure A21. Steam is being used to visually locate the center of the vortex shed by fin #9b at $\alpha_T = 7^o$. At $V_\infty = 87.5$ ft/sec the rotor is rotating at $\omega = 1483.0$ rpm

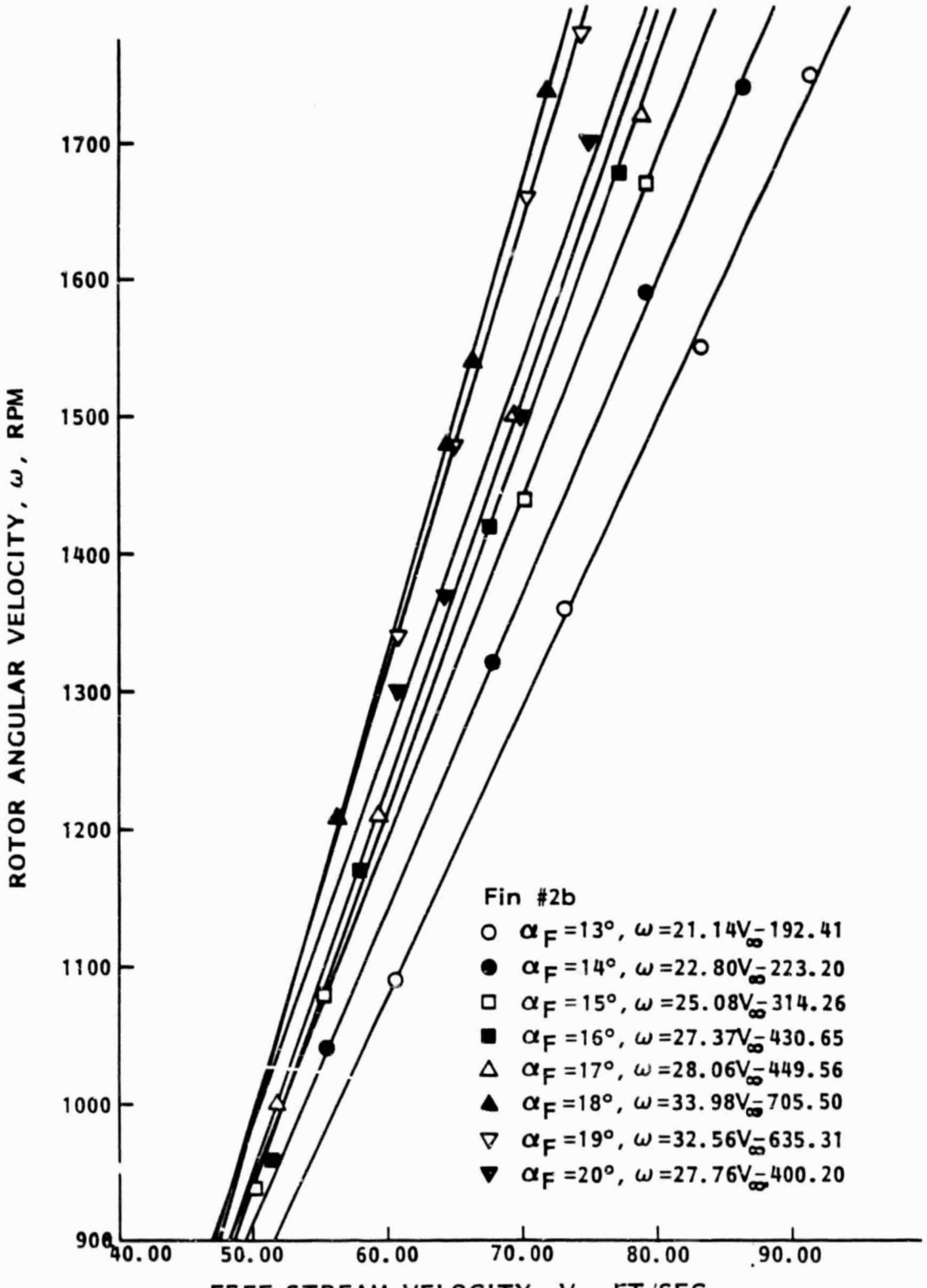

Figure A22. Rotor angular velocity vs. free stream velocity

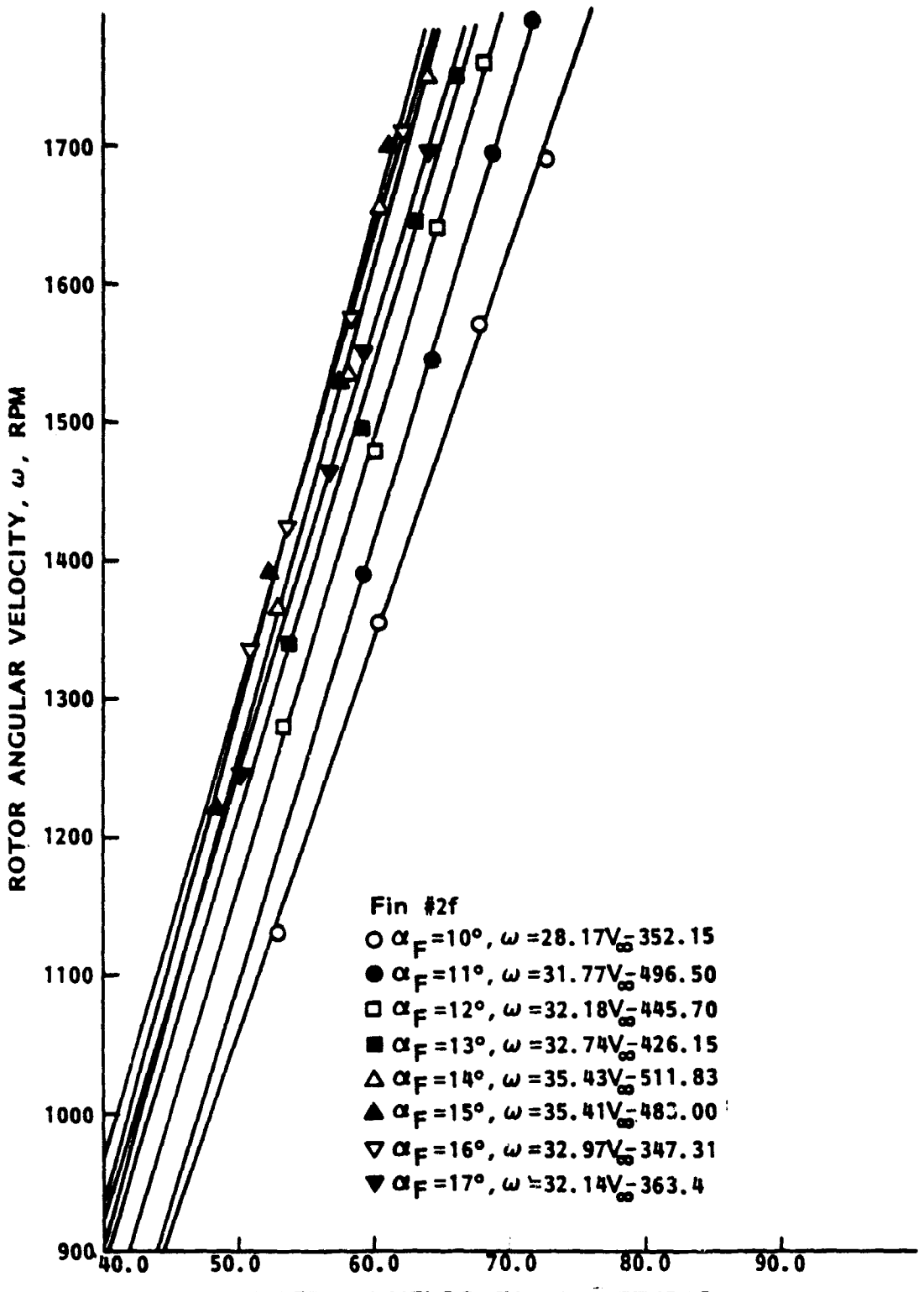

Figure A23. Rotor angular velocity vs. free stream velocity

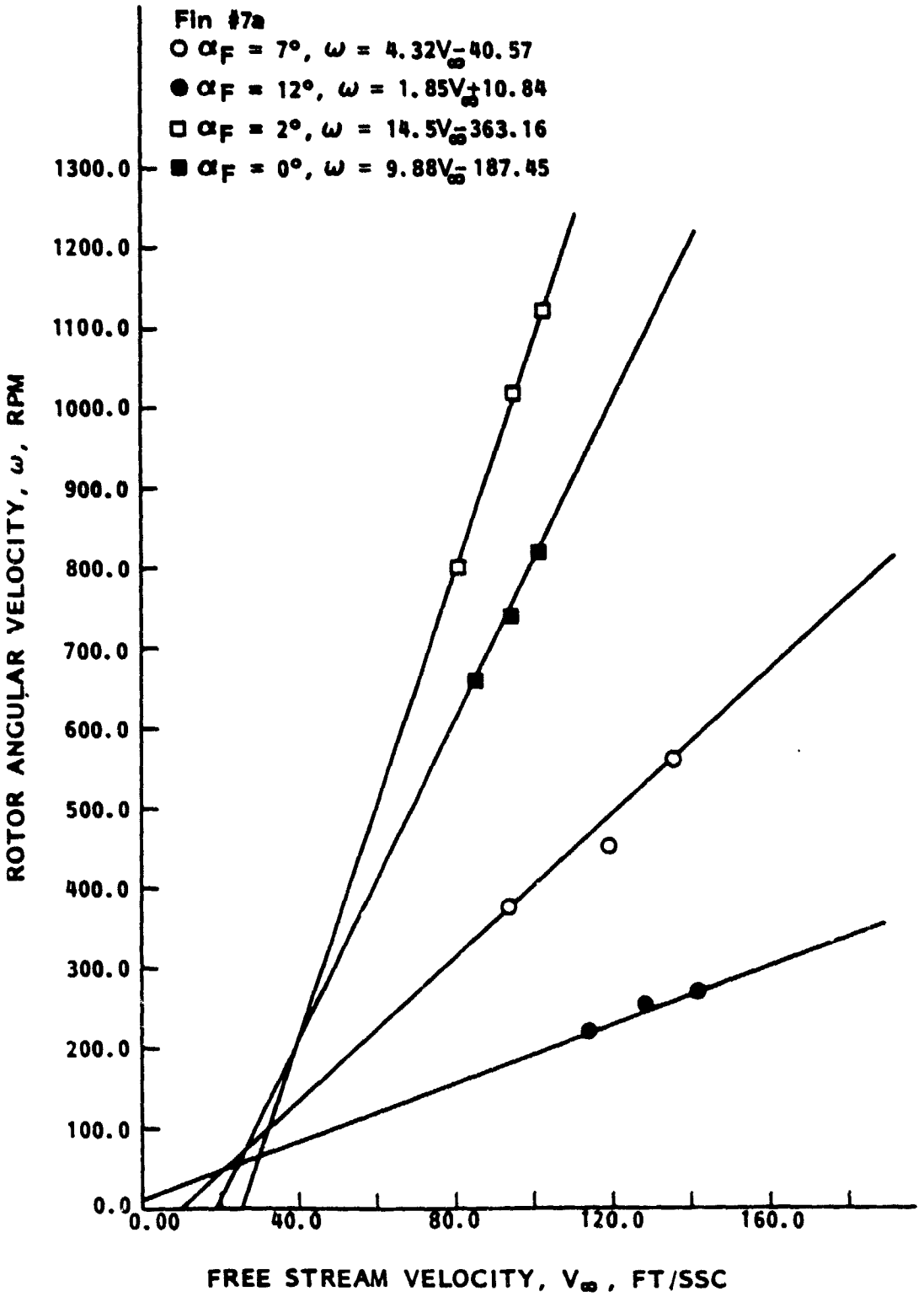

Figure A24. Rotor angular velocity vs. free stream ocity

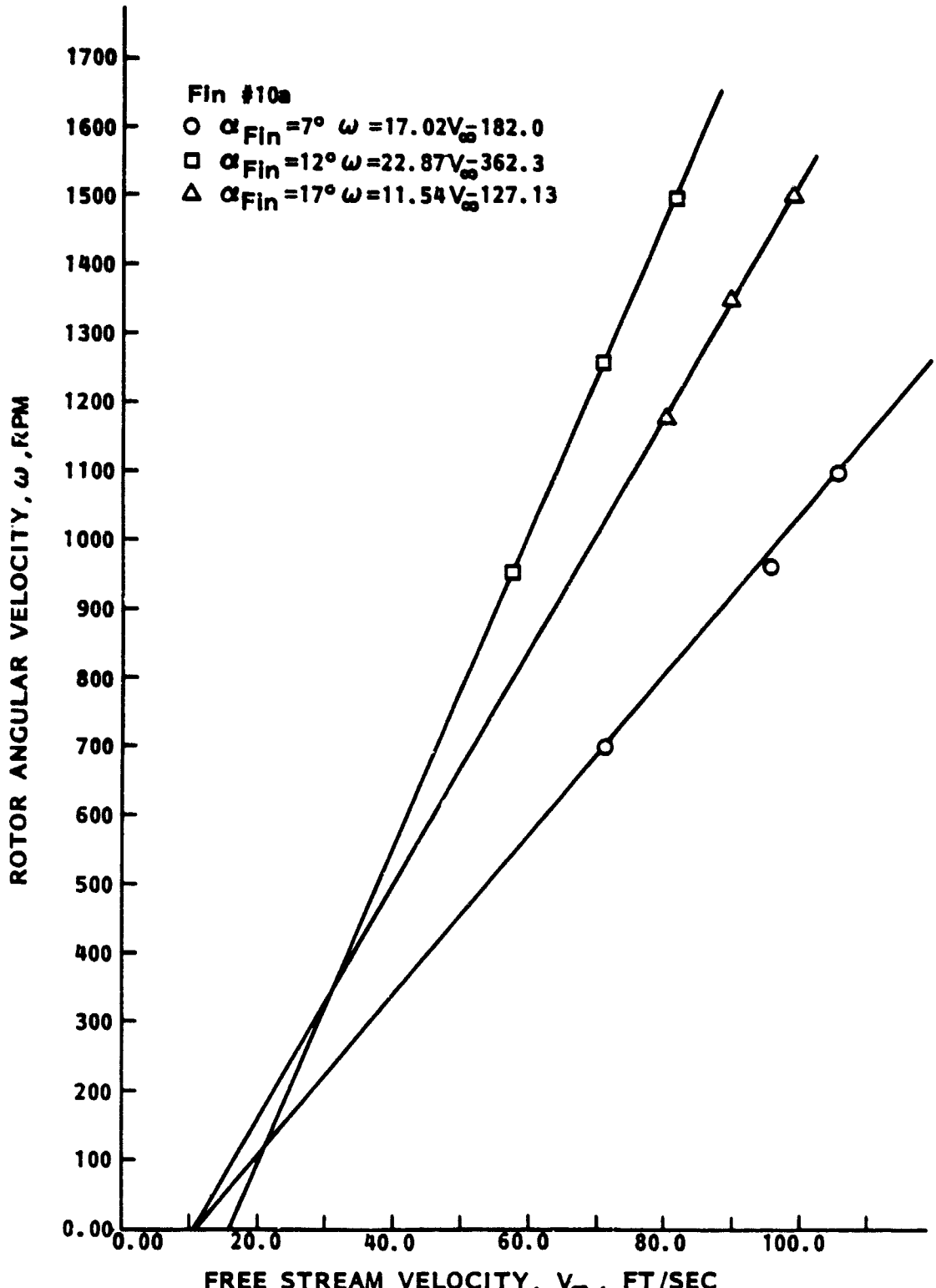

Figure A25. Rotor angular velocity vs. free stream velocity

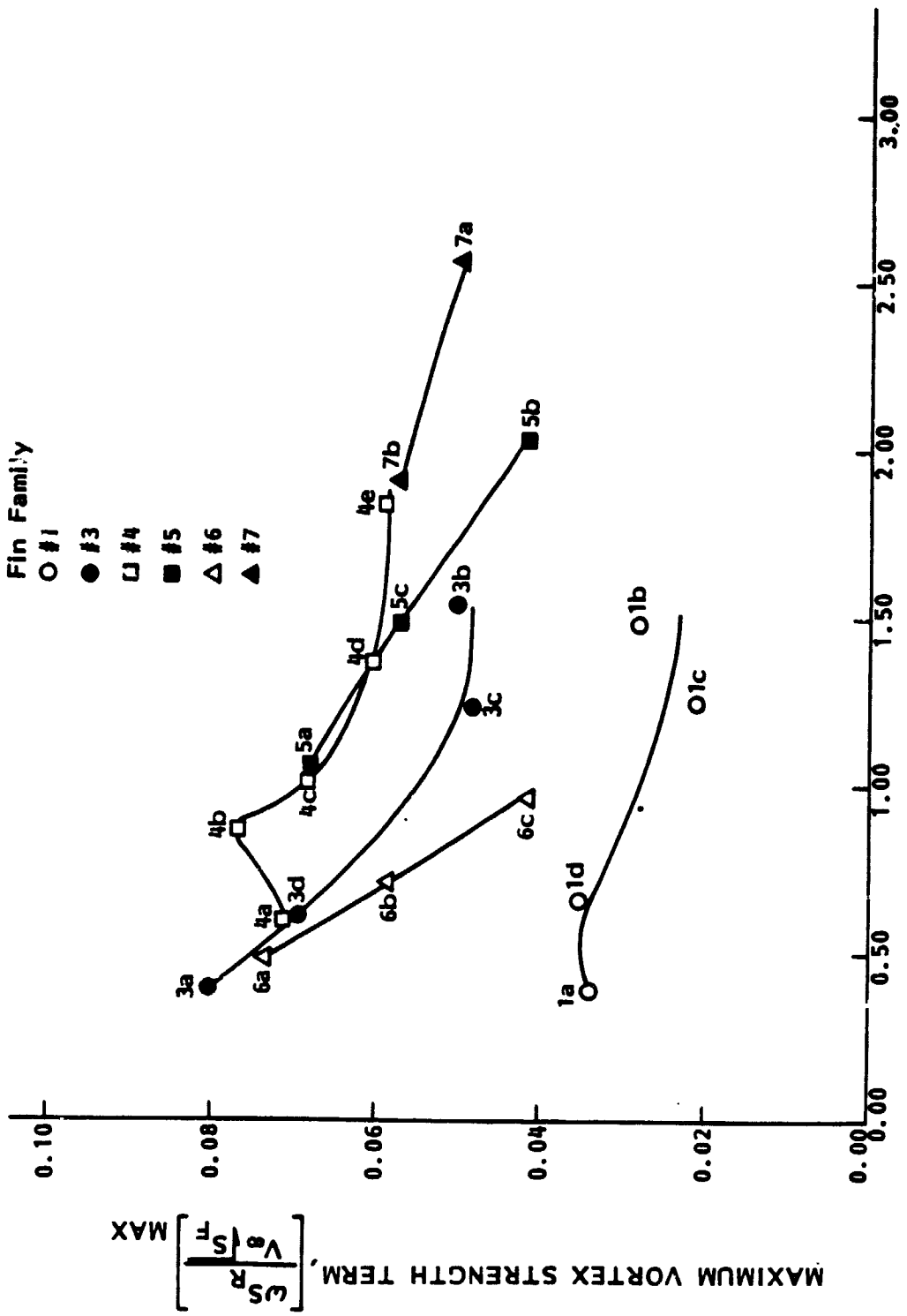

Figure A26. Maximum vortex strength term vs. fin aspect ratio

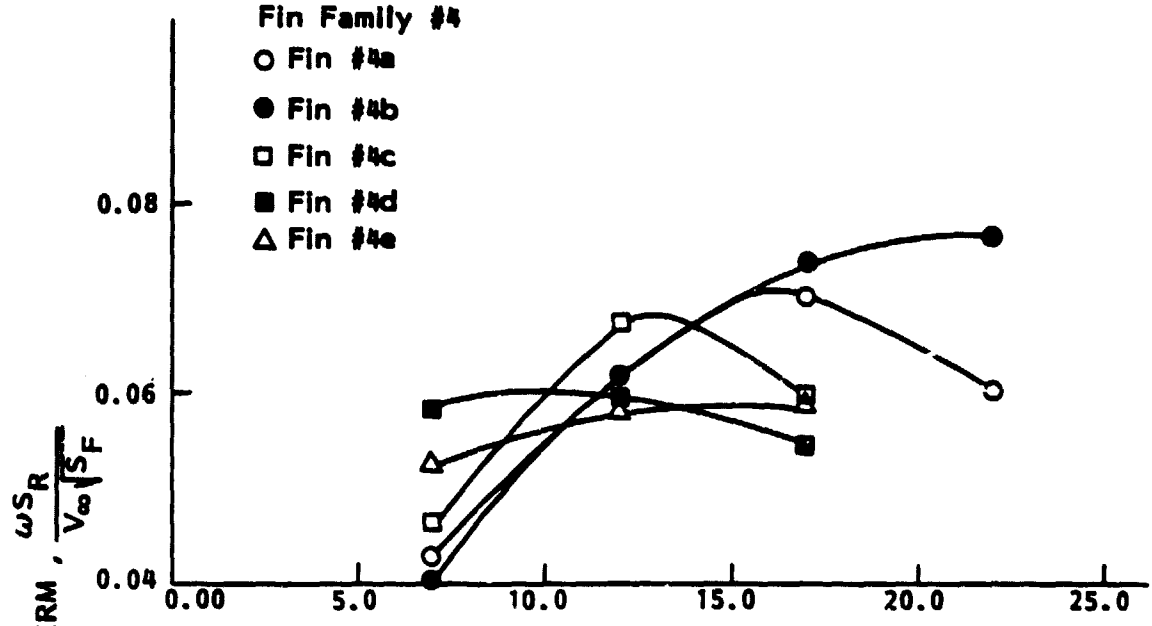

Figure A27. Vortex strength term vs. fin angle of attack

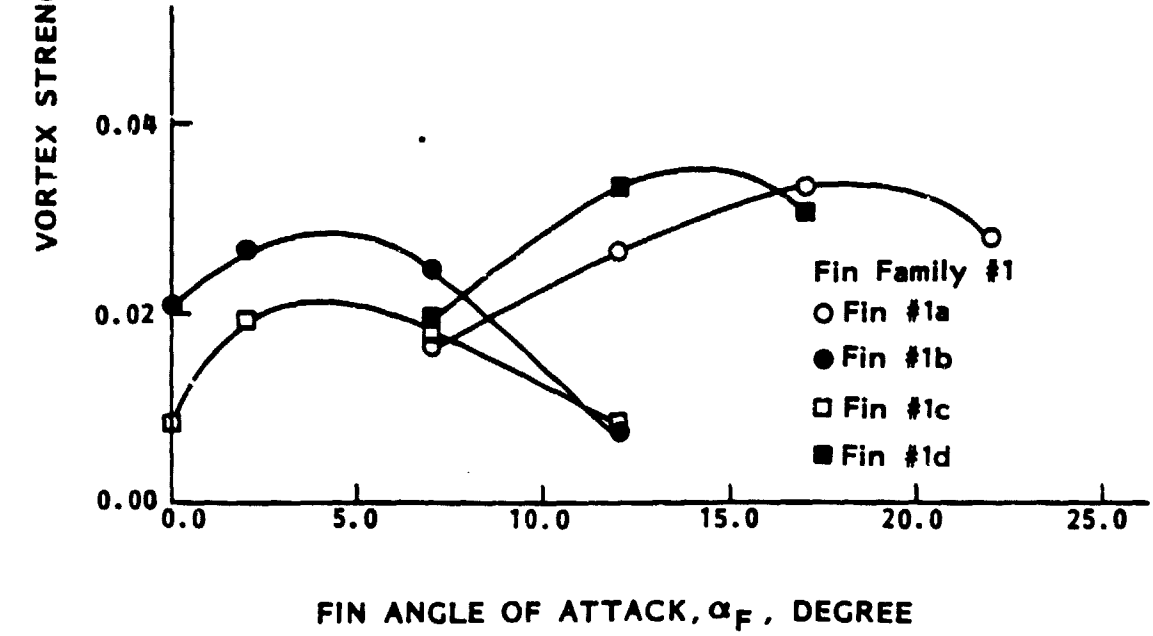

Figure A28. Vortex strength term vs. fin angle of attack

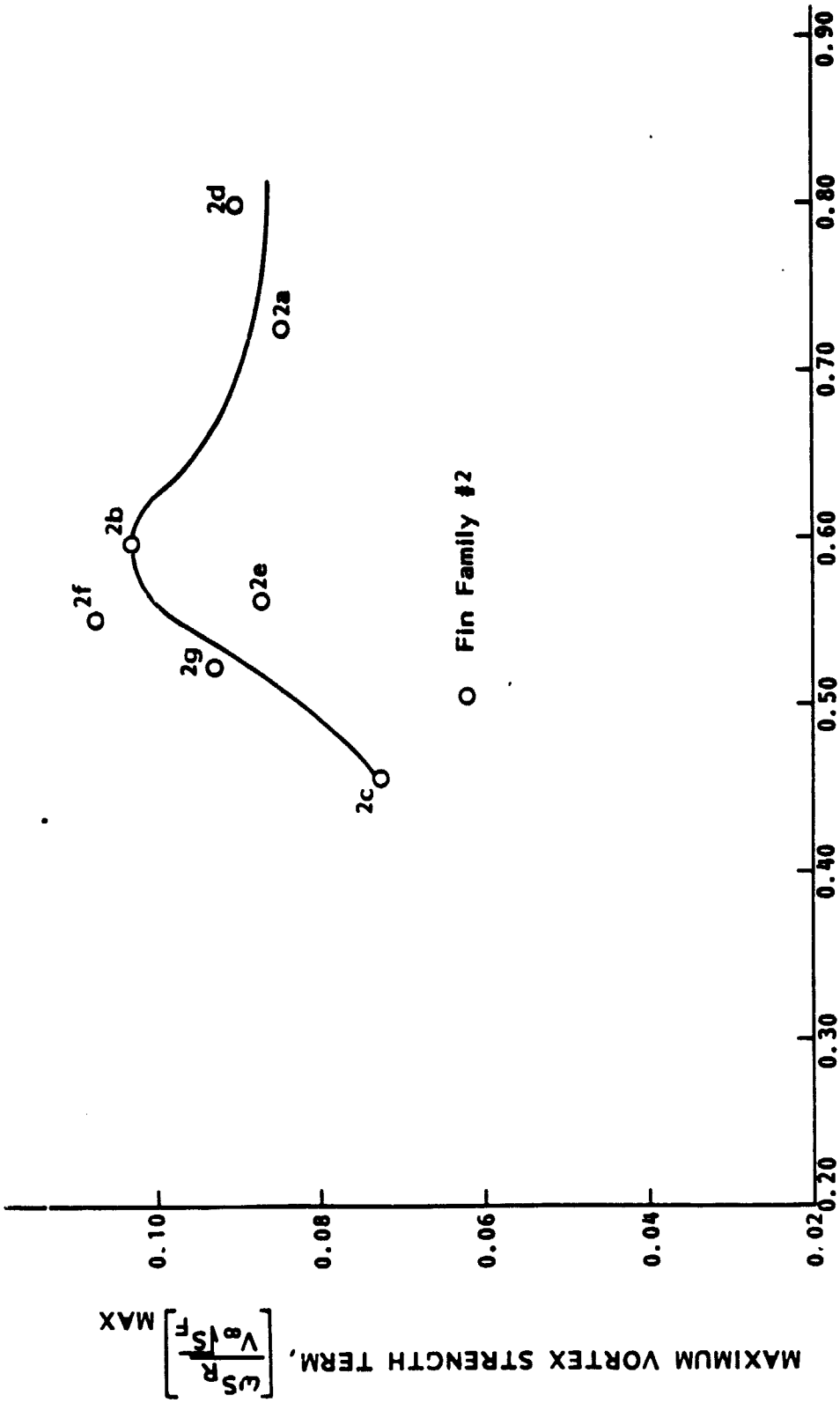

Figure A29. Maximum vortex strength term vs. fin aspect ratio

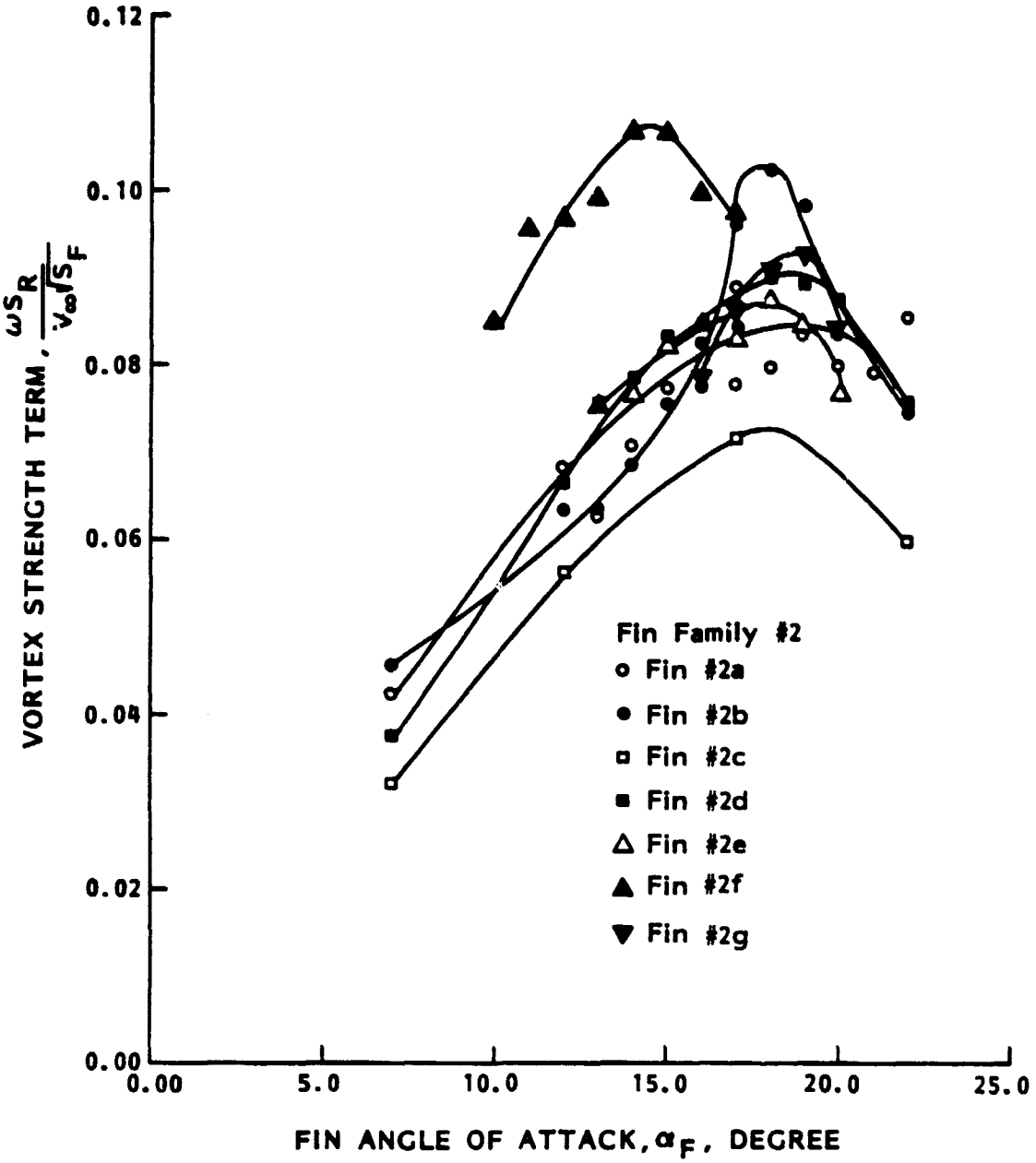

Figure A30. Vortex strength term vs. fin angle of attack

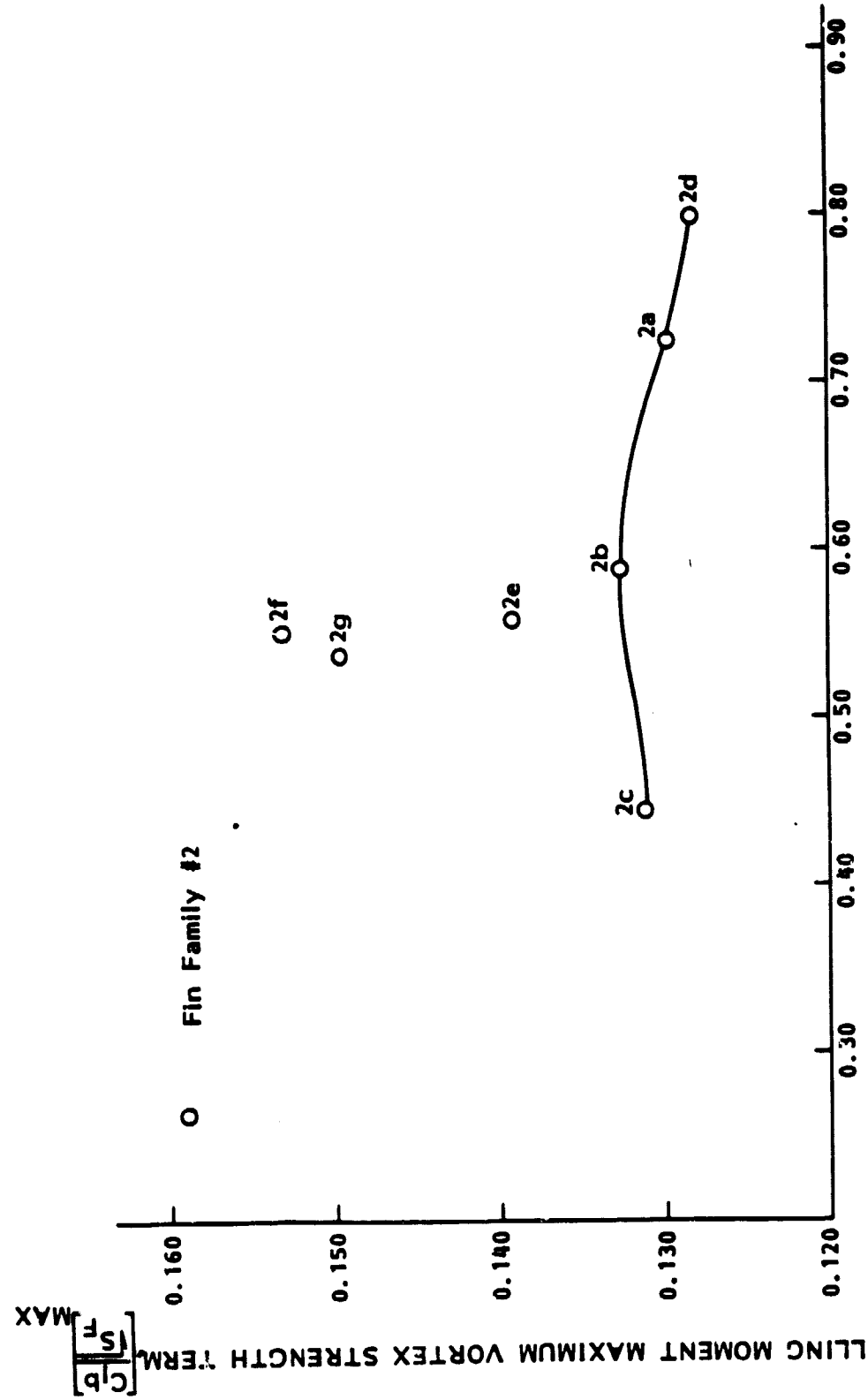

Figure A31. Rolling moment maximum vortex strength term vs. fin aspect ratio

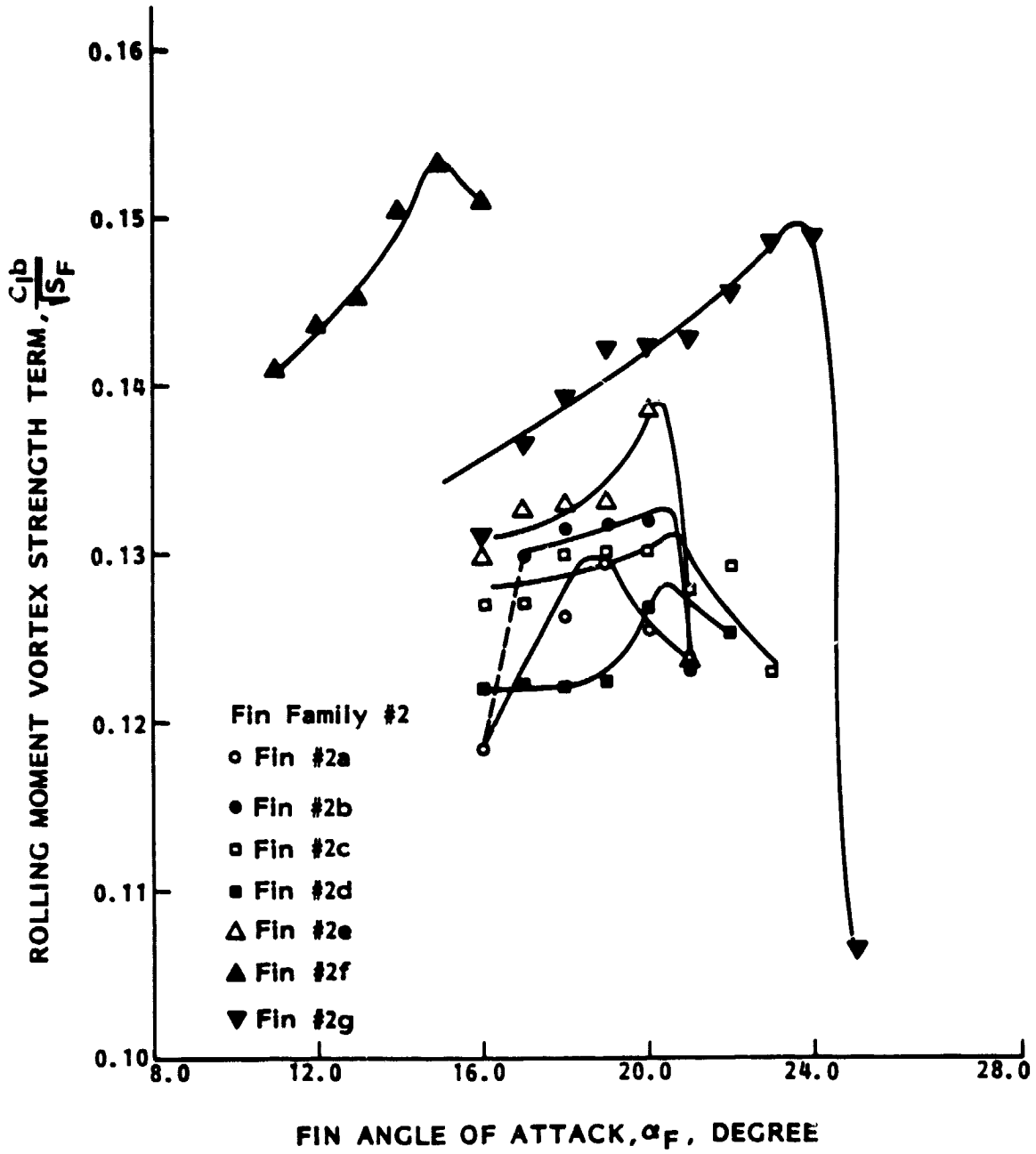

Figure A32. Rolling moment vortex strength term vs. fin angle of attack

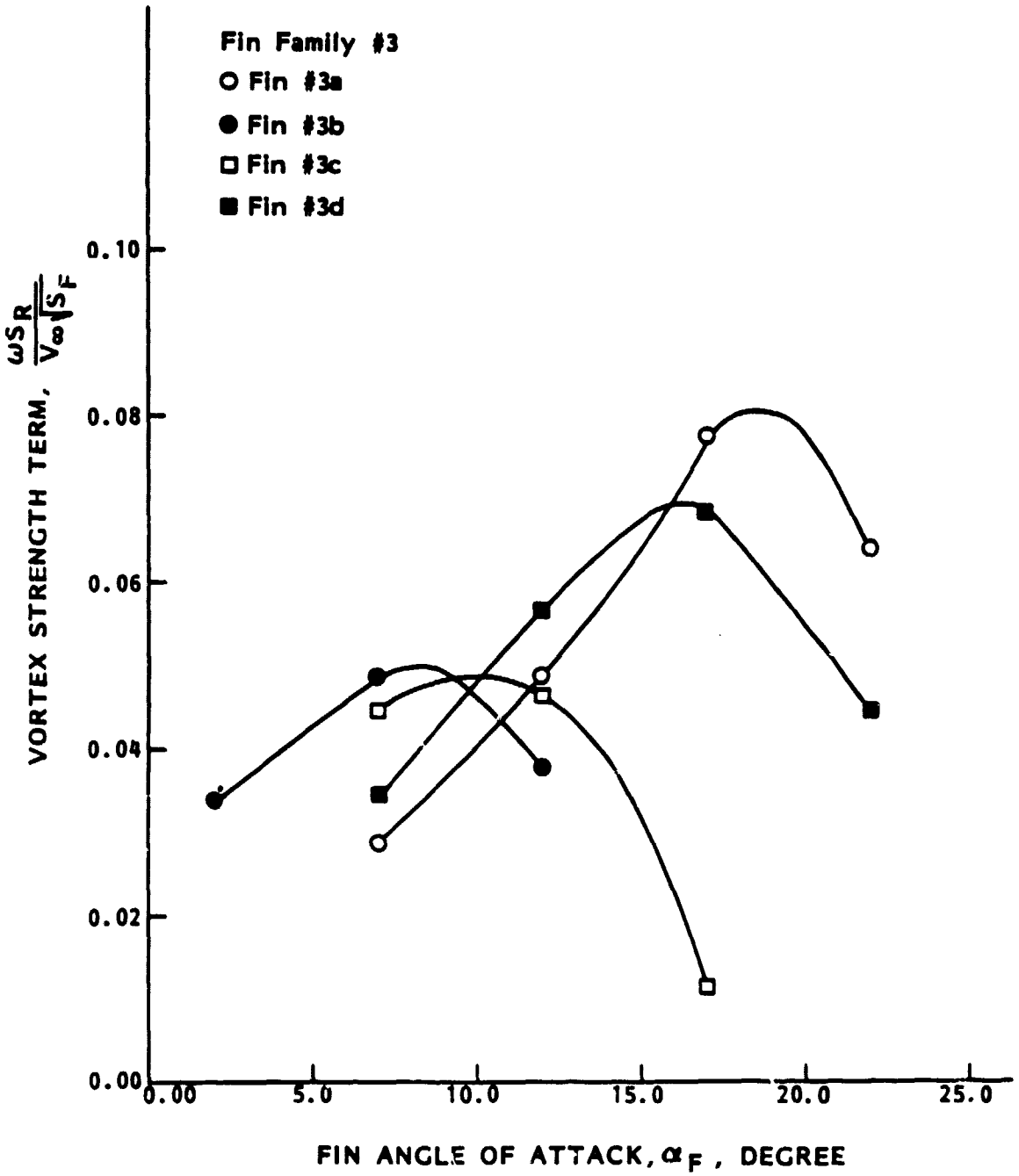

Figure A33. Vortex strength term vs. fin angle of attack

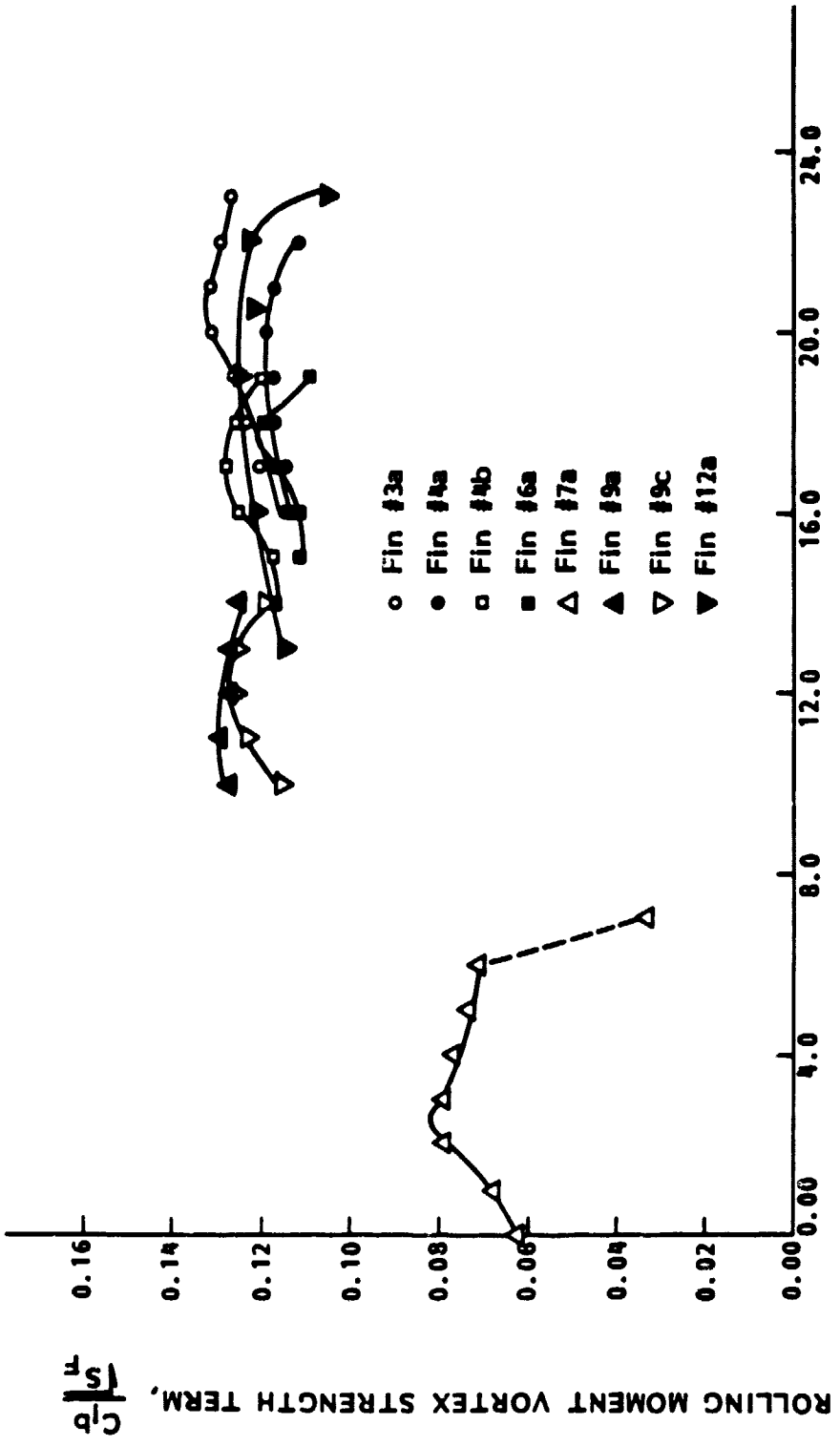

Figure A34. Rolling moment vortex strength term vs. fin angle of attack

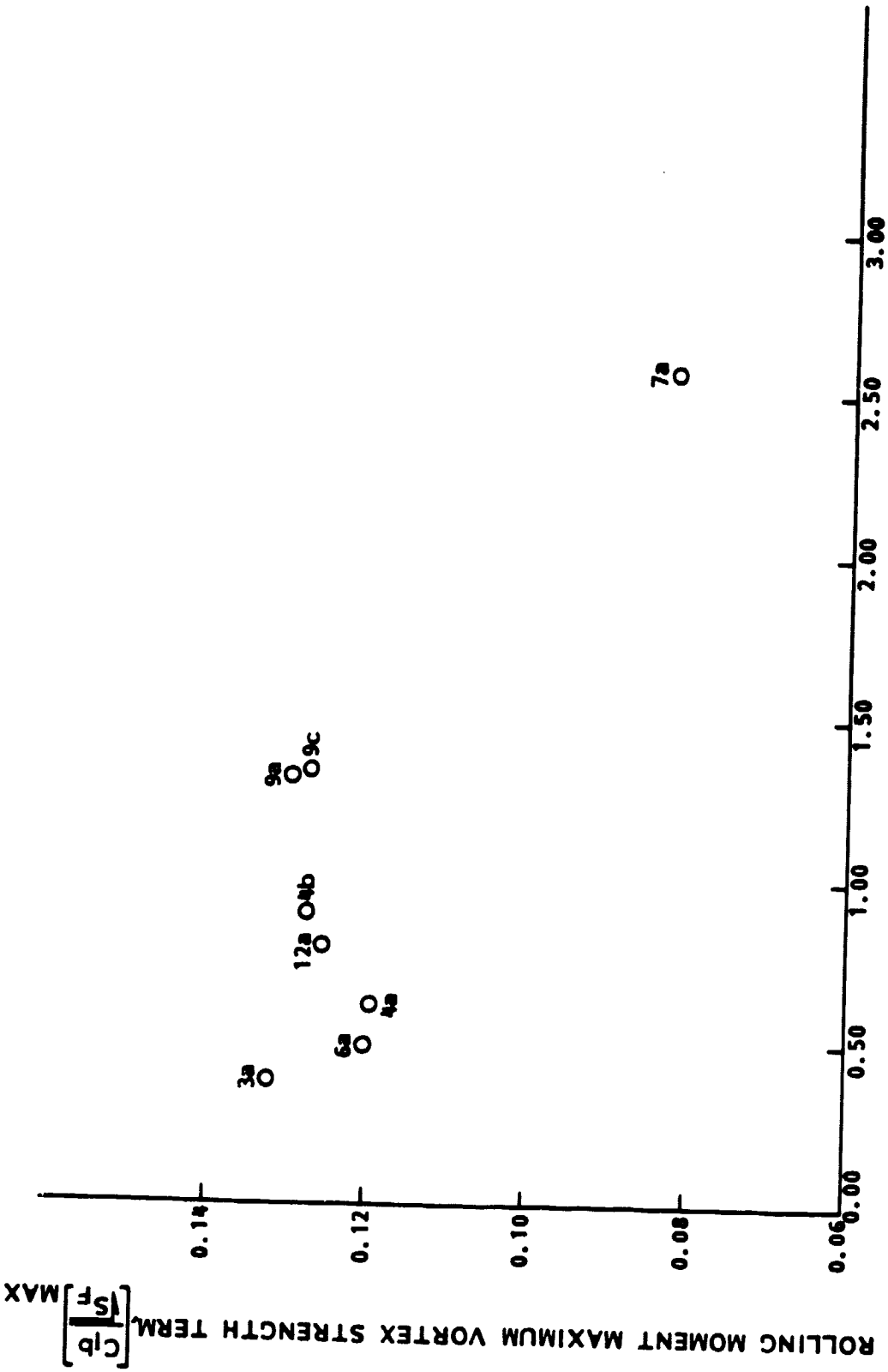

Figure A35. Rolling moment maximum vortex strength term vs. fin aspect ratio

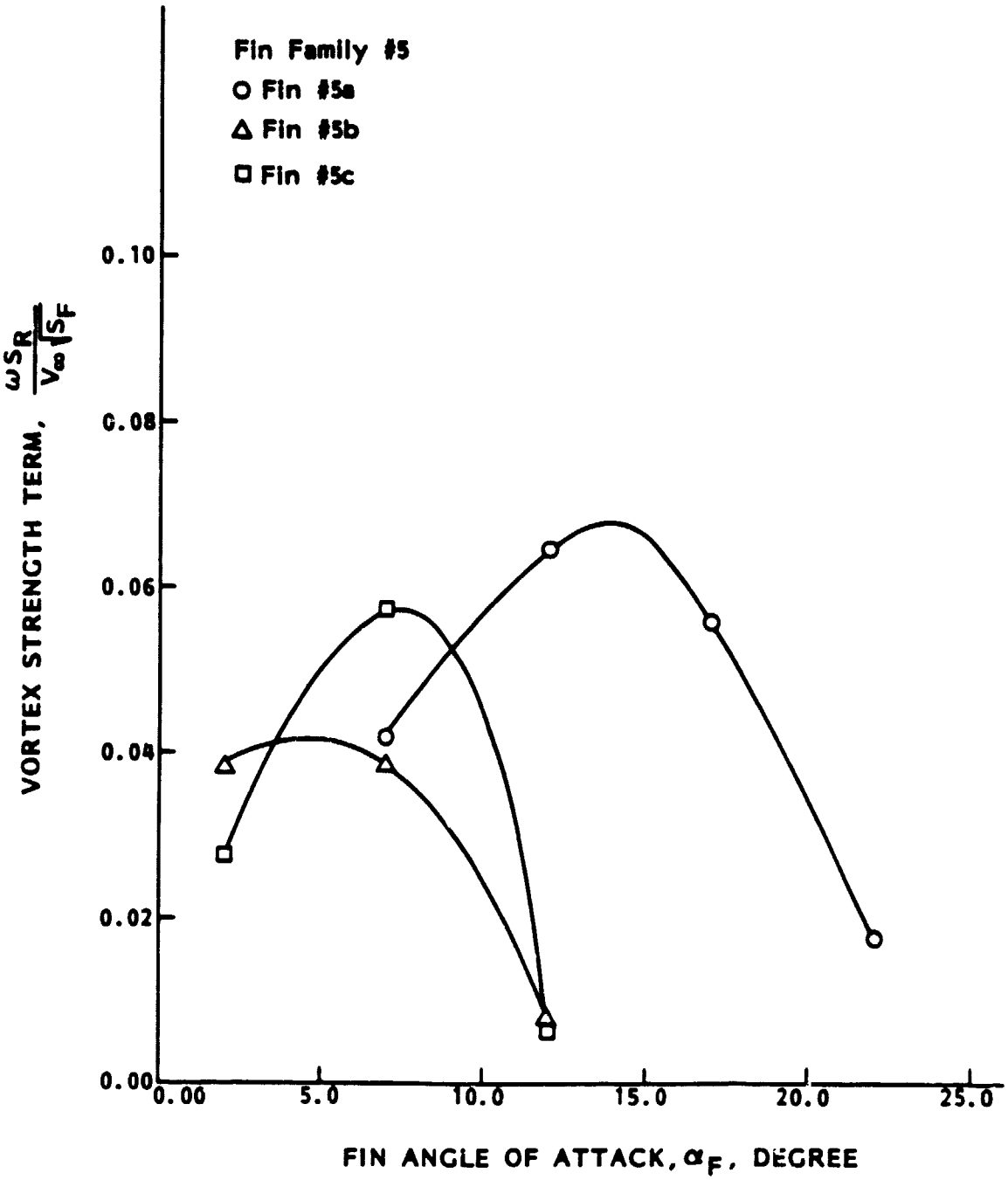

Figure A36. Vortex strength term vs. fin angle of attack

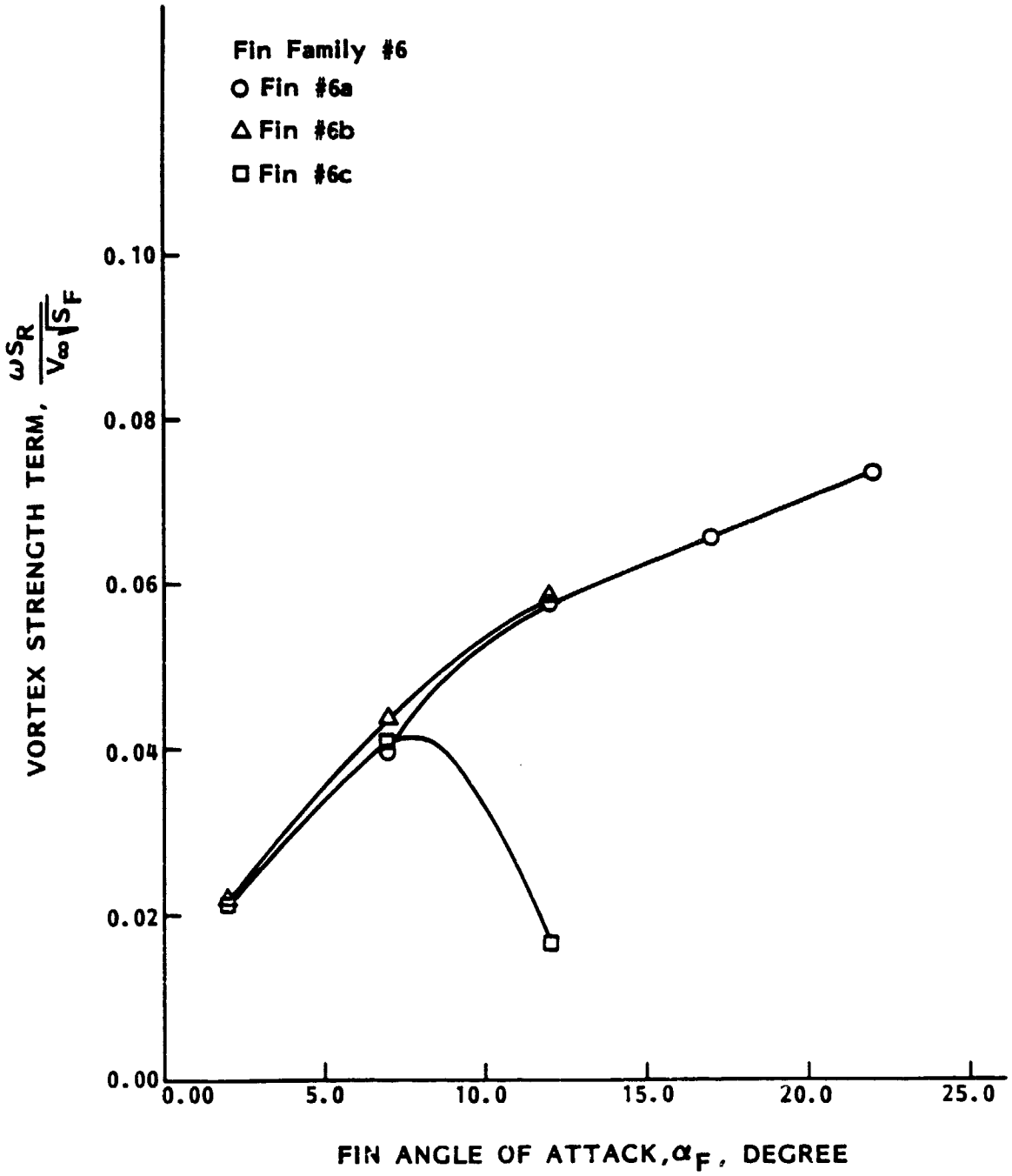

Figure A37. Vortex strength term vs. fin angle of attack

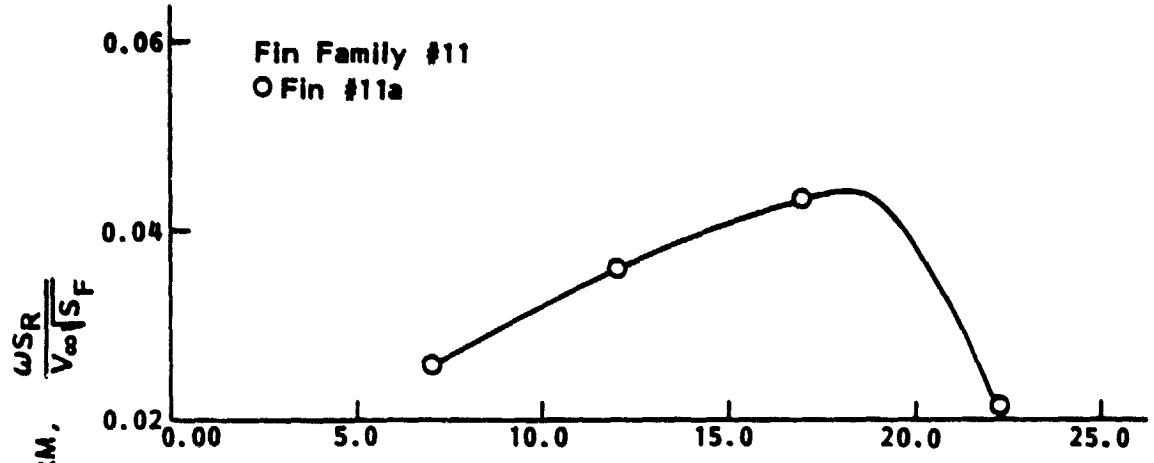

Figure A38. Vortex strength term vs. fin angle of attack

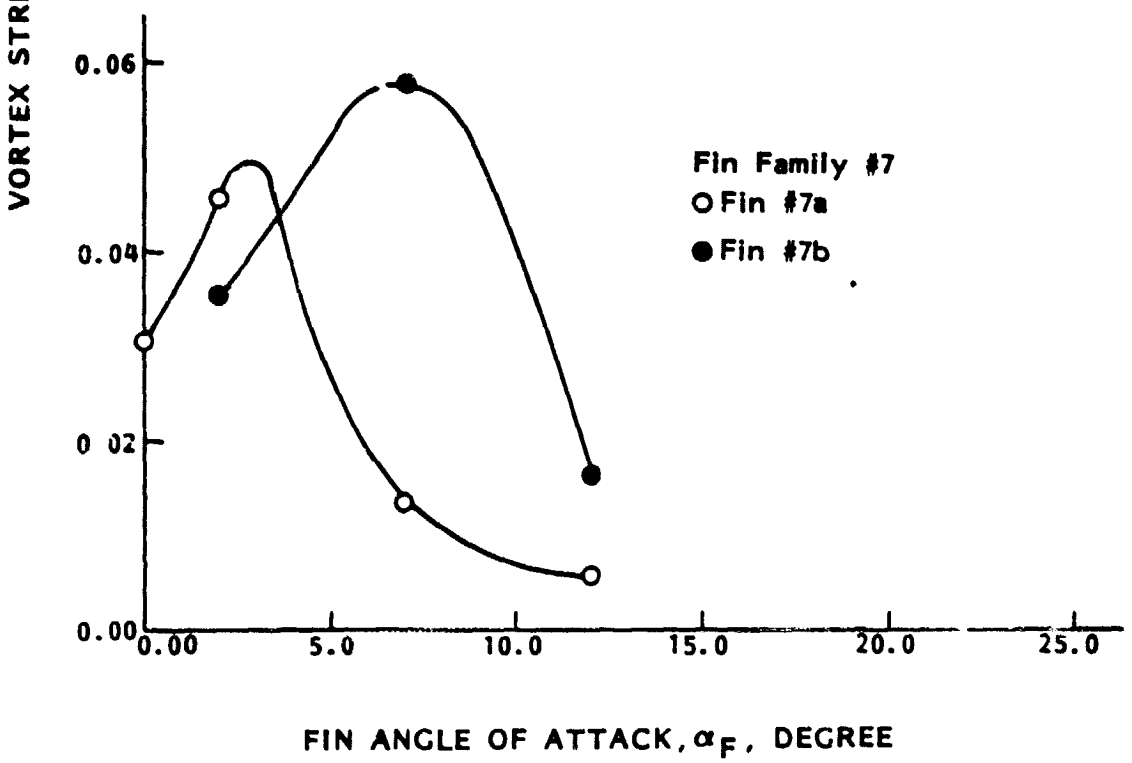

Figure A39. Vortex strength term vs. fin angle of attack

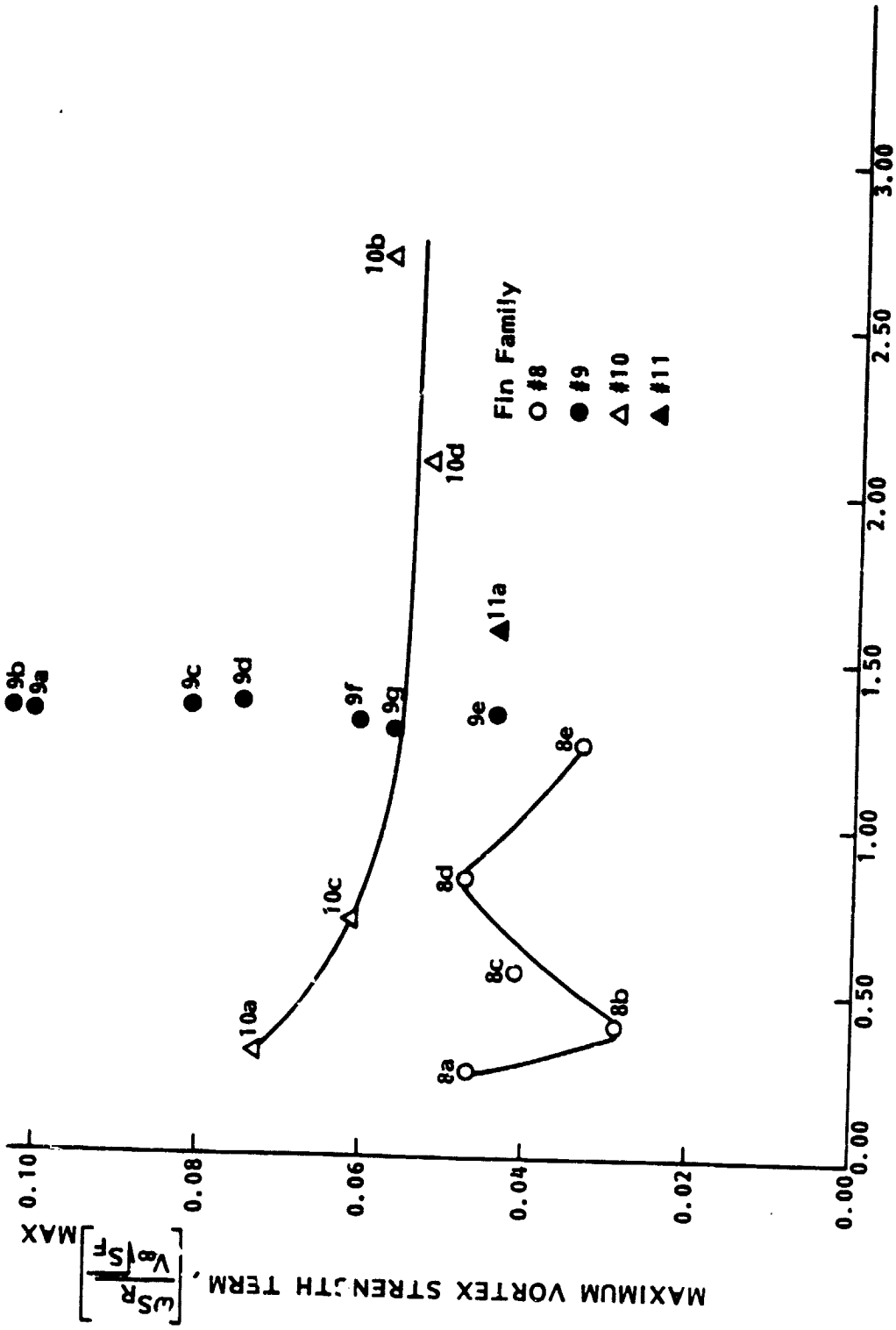

Figure A40. Maximun vortex strength term vs. fin aspect ratio

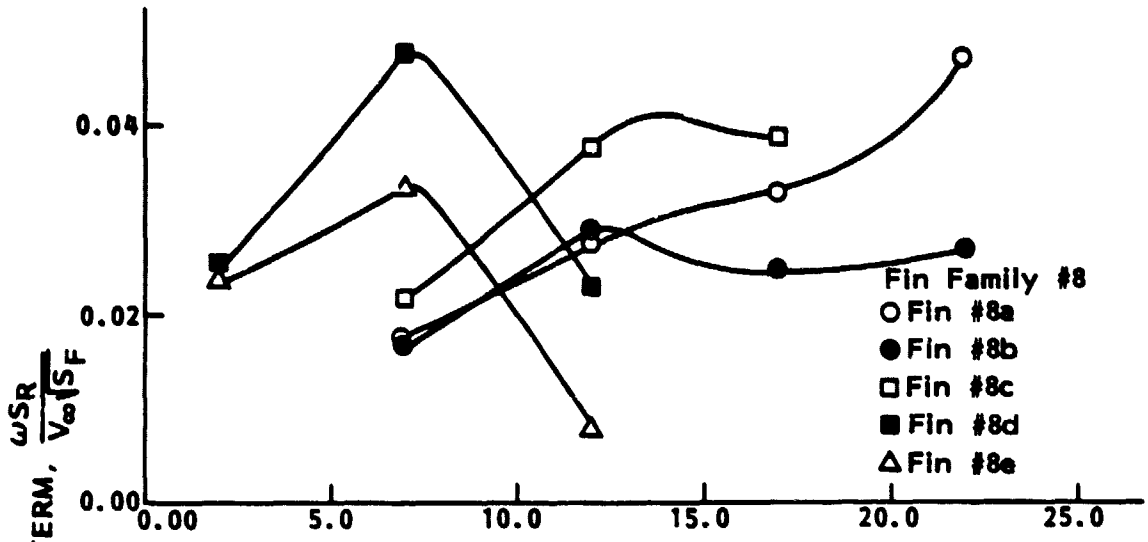

Figure A41. Vortex strength term vs. fin angle of attack

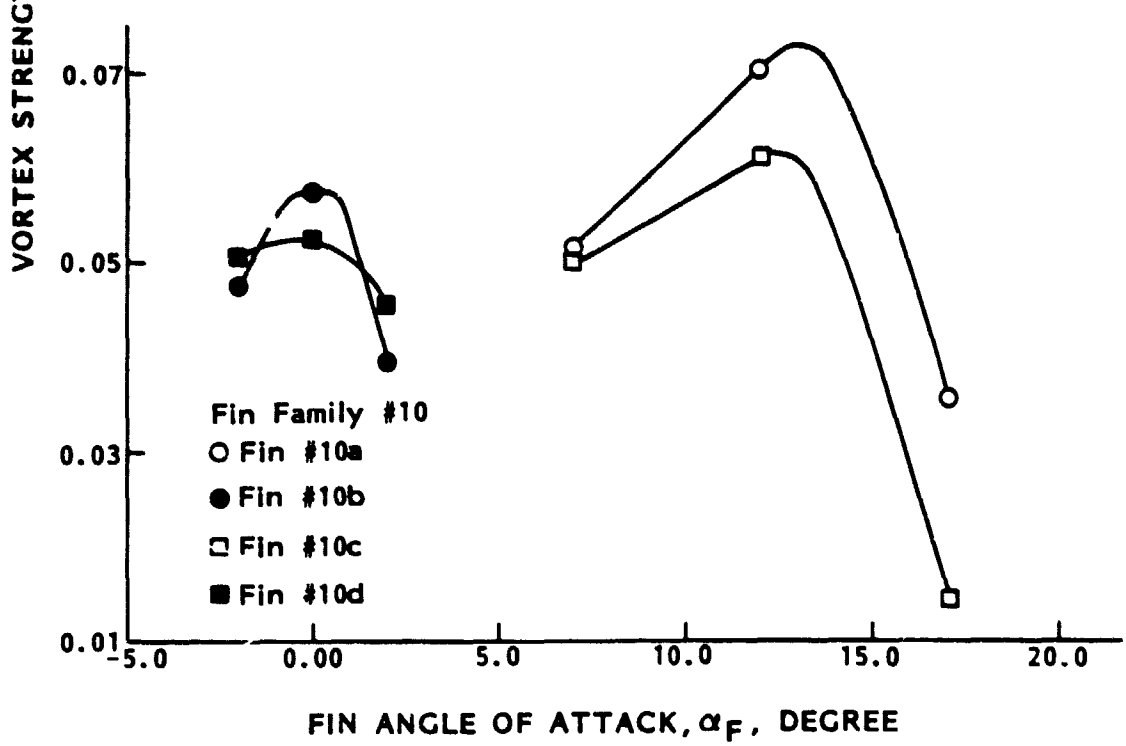

Figure A42. Vortex strength term vs. fin angle of attack

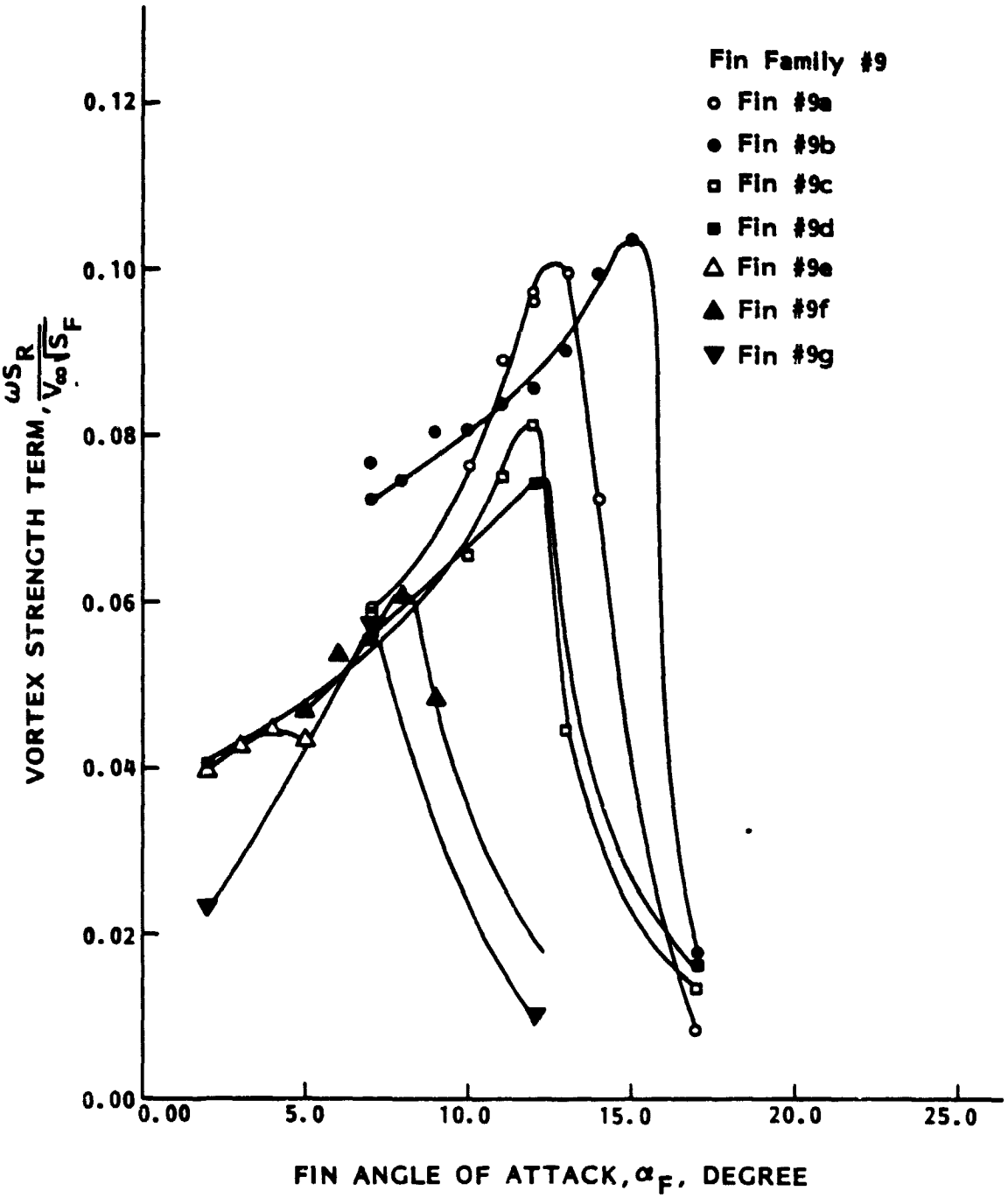

Figure A43. Vortex strength term vs. fin angle of attack

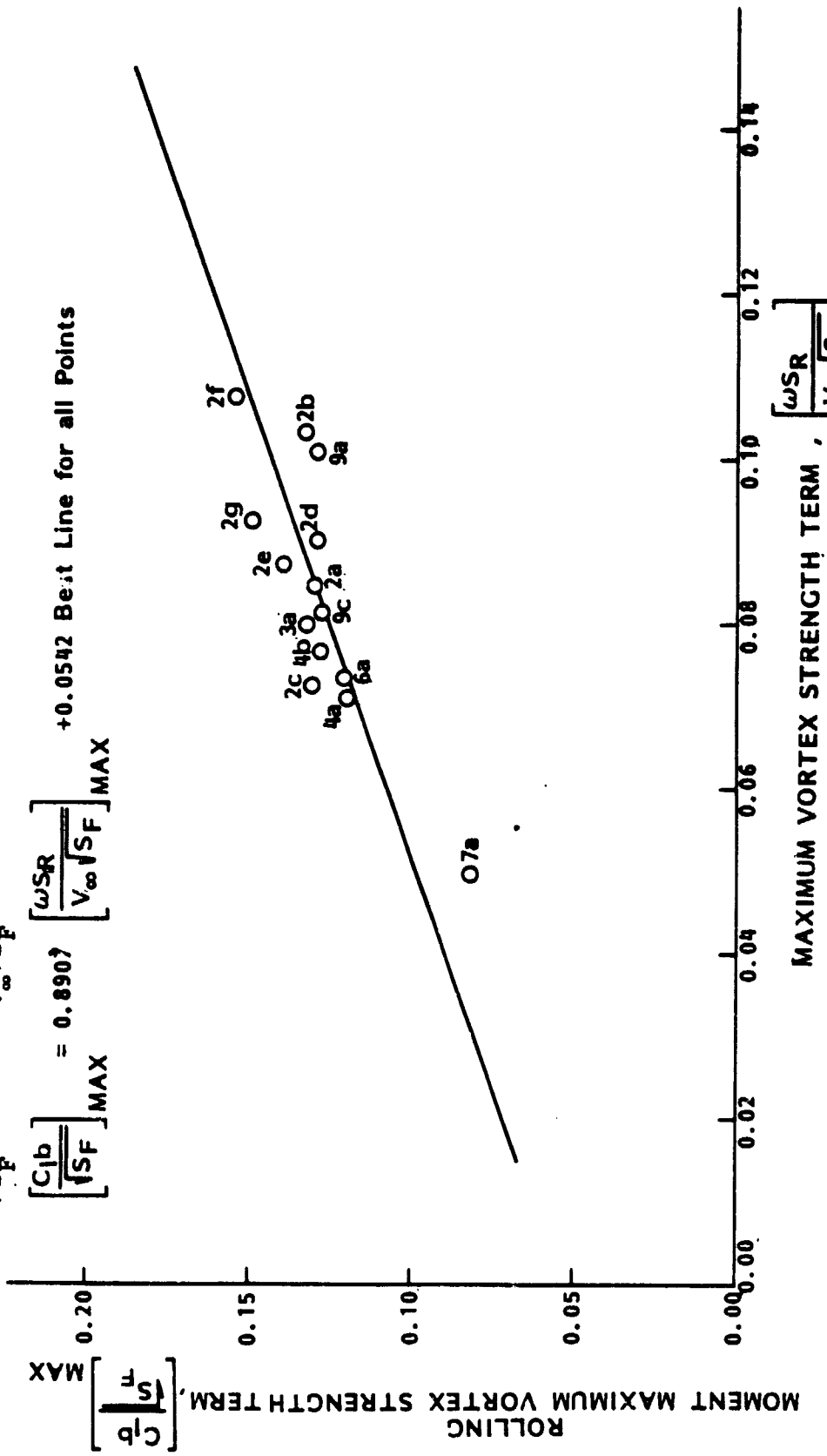

Figure A44. Correlation between the force balance technique and the rotor method

APPENDIX B: PLAN-FORM CONFIGURATIONS

Figure B1. Fin family #1. Fins #1a through #1d have sharp trailing edges, smooth leading and upper edges, and the thickness of 0.25 in.

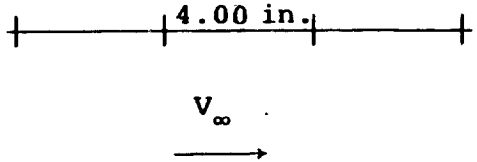

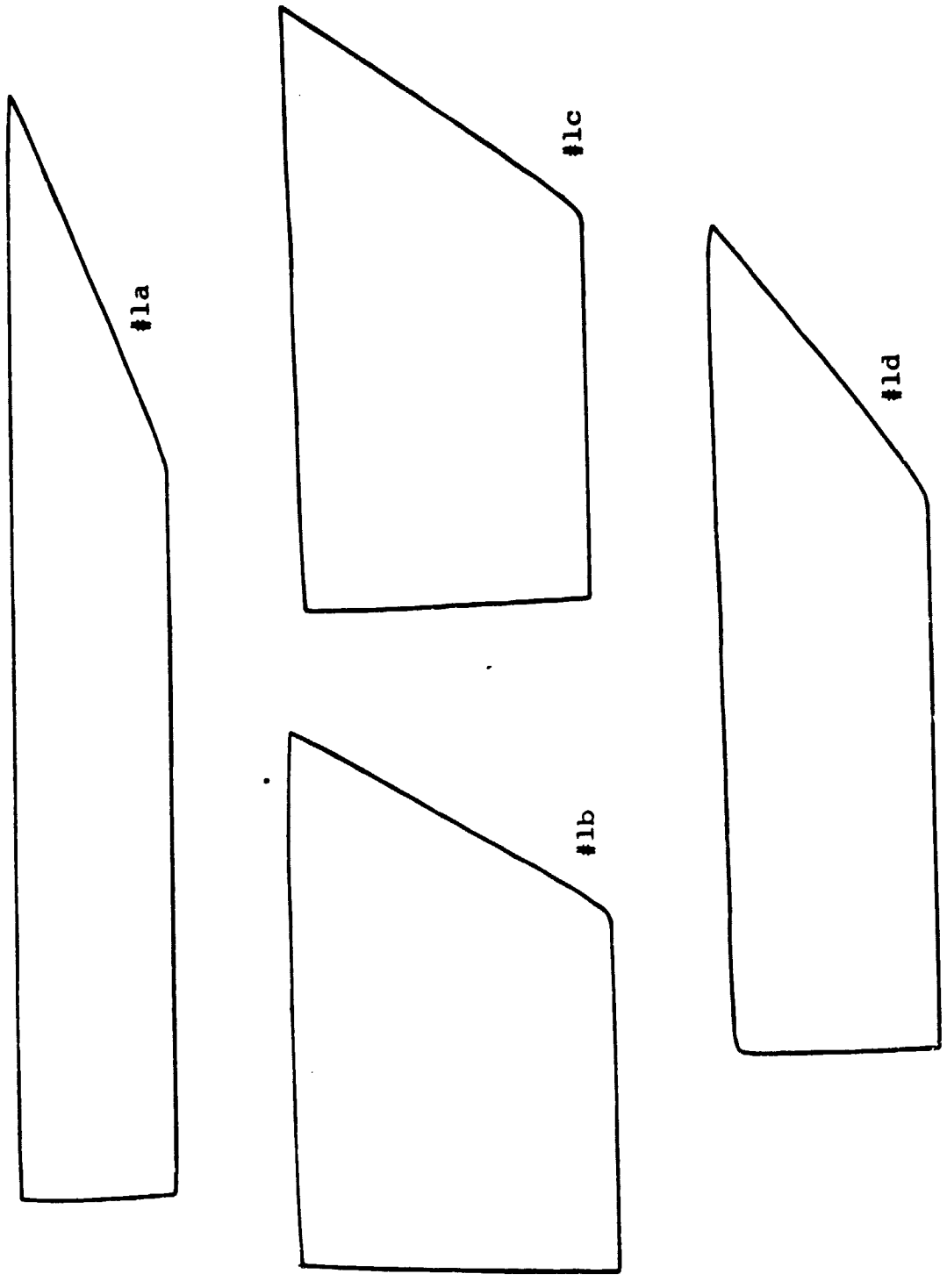
#1a
#1c
#1d
#1b

Figure B2. Fin family #2. Fin#2a through #2d have sharp trailing edges, smooth leading and upper edges and the thickness of 0.25 in., #2e has sharp edges and is 0.0625 in. thick, #2f has sharp edges, is 0.0625 in. thick and was bent to a form of 5% circular arc plate, #2g has sharp edges and has a 5% thick circular section

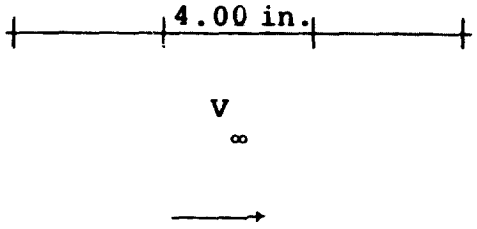

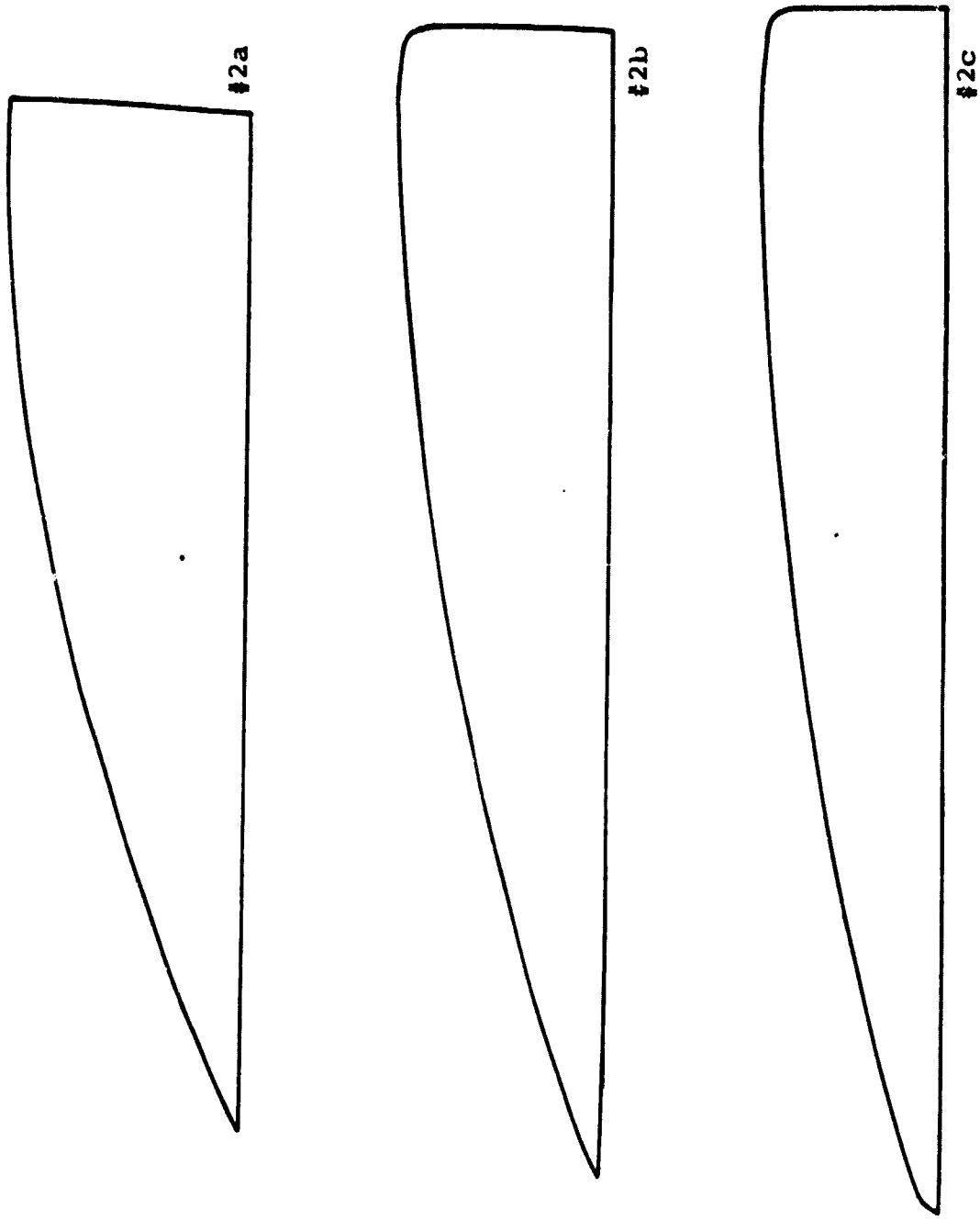
#2a
#2b
#2c

Figure B2 (Continued)

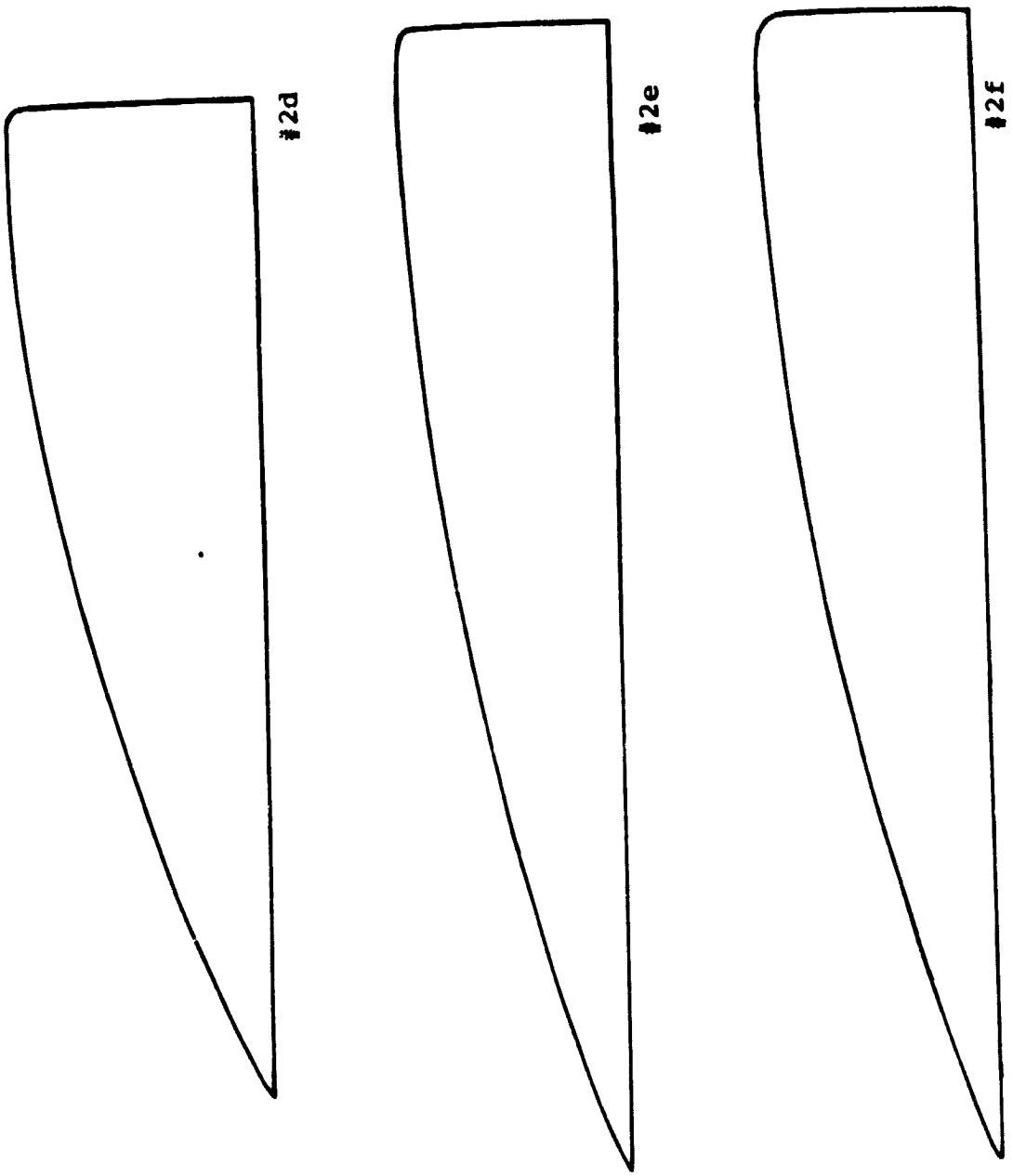
#2d
#2e
#2f

Figure B2 (Continued)

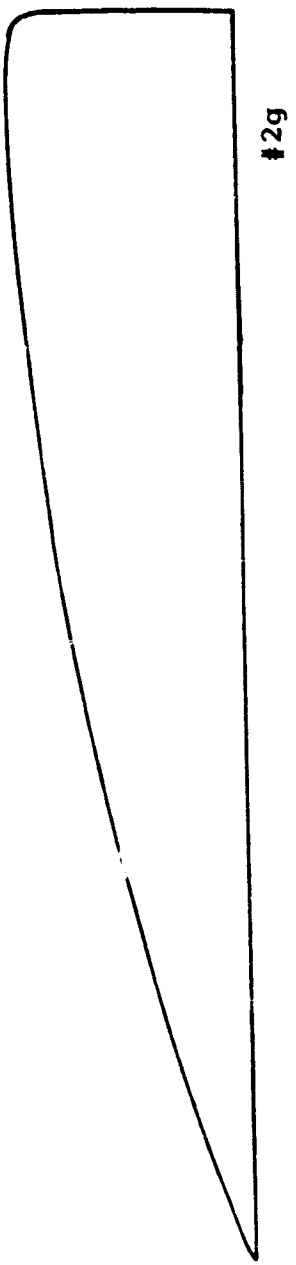
#2g

Figure B3. Fin family #3. Fin #3a through #3d have sharp trailing edges, smooth leading and upper edges, and thickness of 0.25 in.

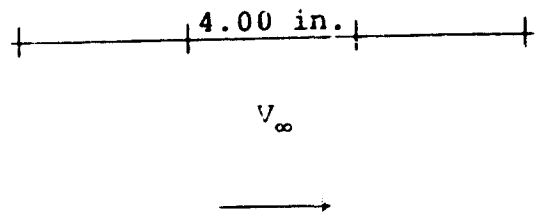

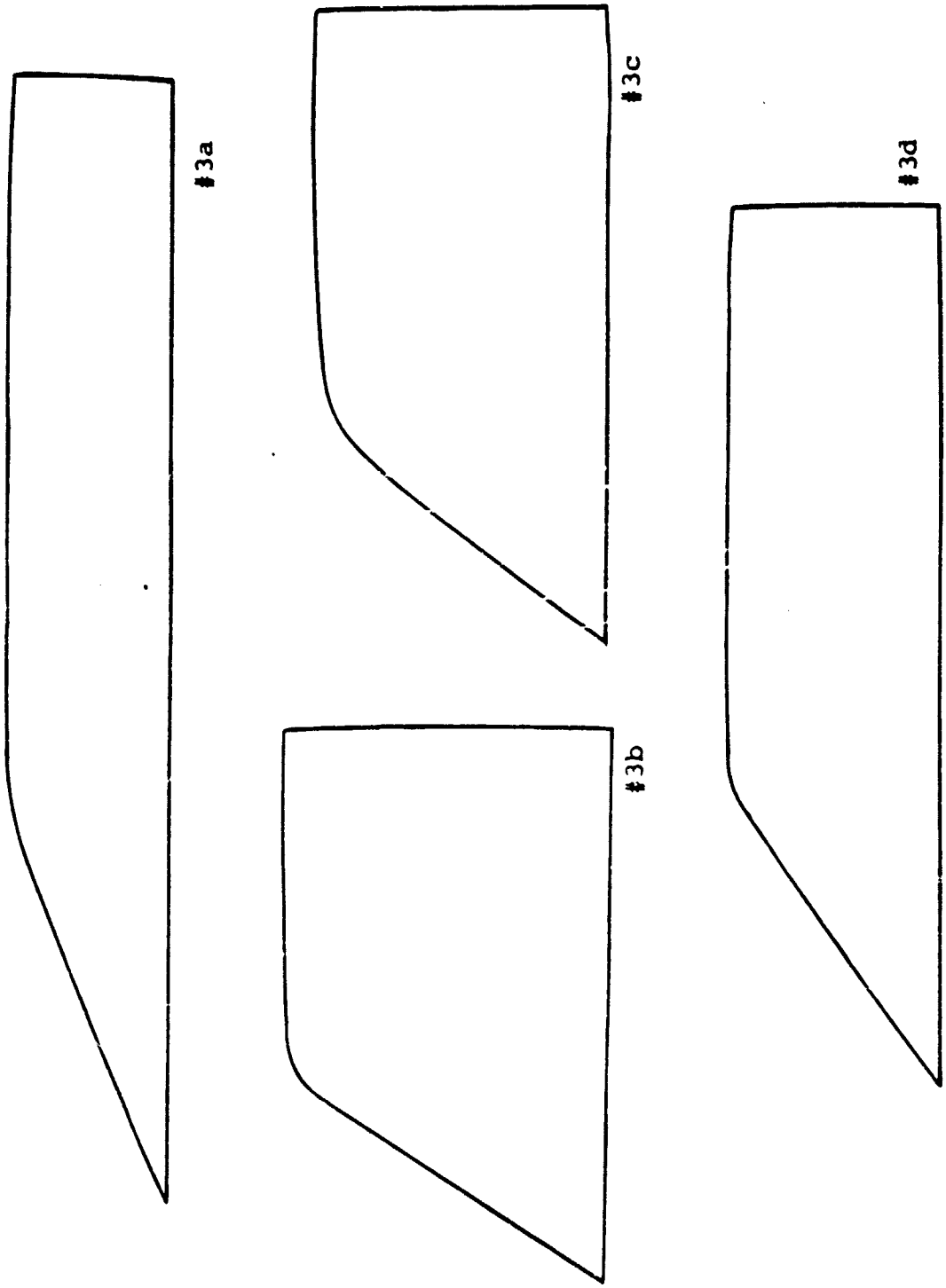
#3a
#3c
#3b
#3d

Figure B4. Fin family #4. Fins #4a through #4e have sharp trailing edges, smooth leading and upper edges, and the thickness of 0.25 in.

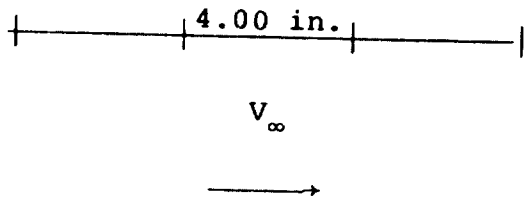

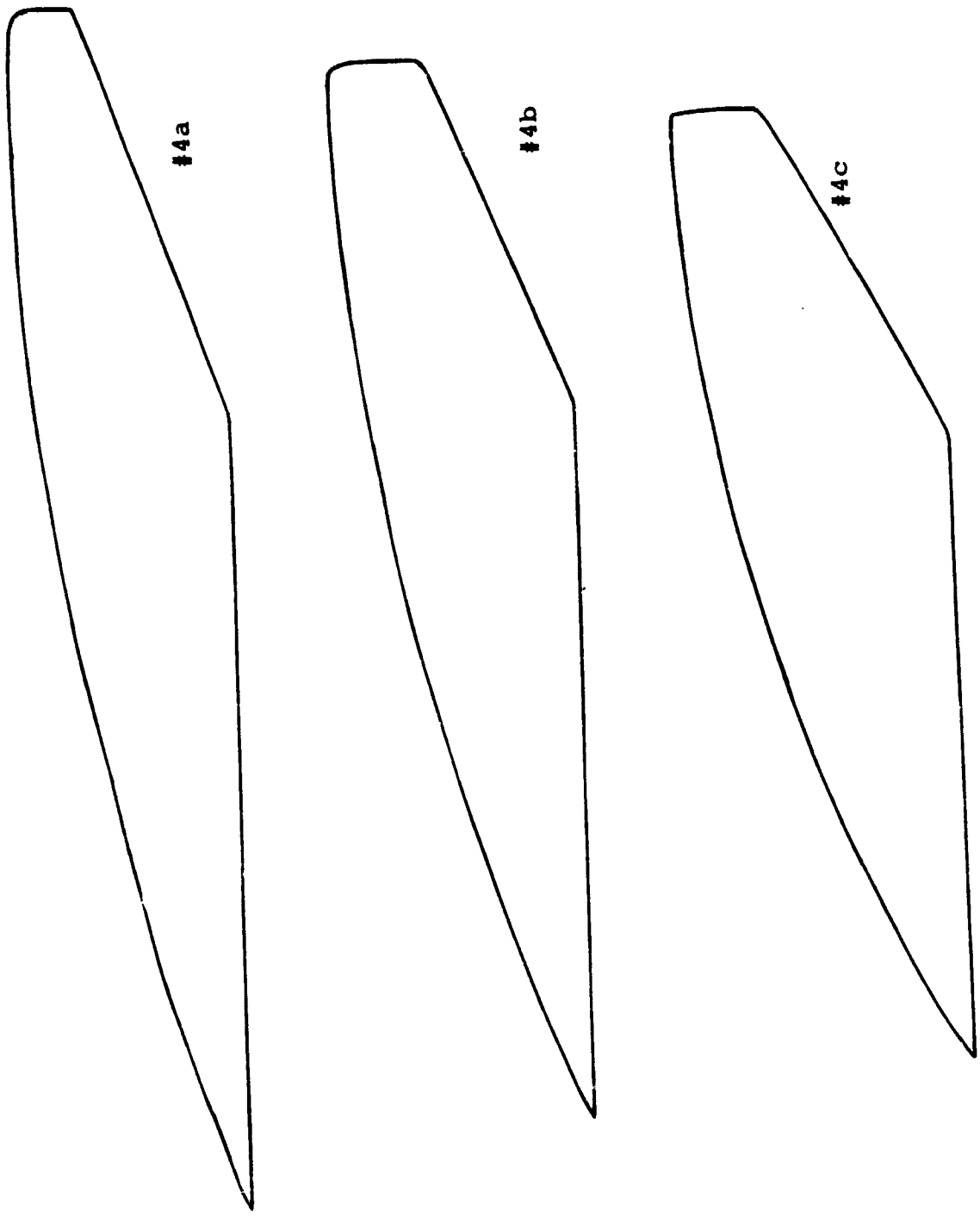
#4a
#4b
#4c

Figure B4 (Continued)

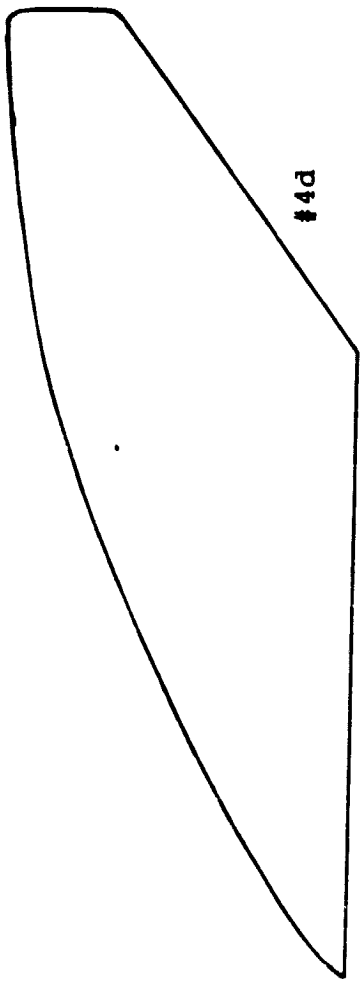
#4d

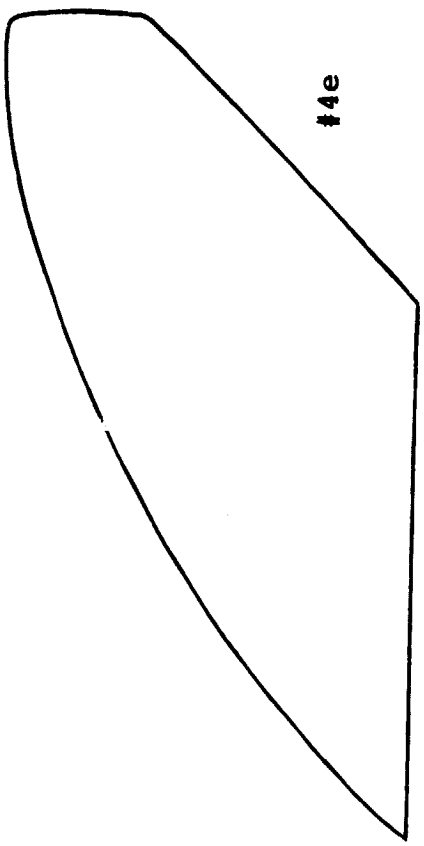
#4e

Figure B5. Fin family #5. Fins #5a through #5c have sharp trailing edges, smooth leading and upper edges and the thickness of 0.25 in.

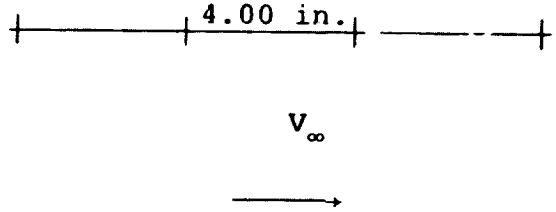

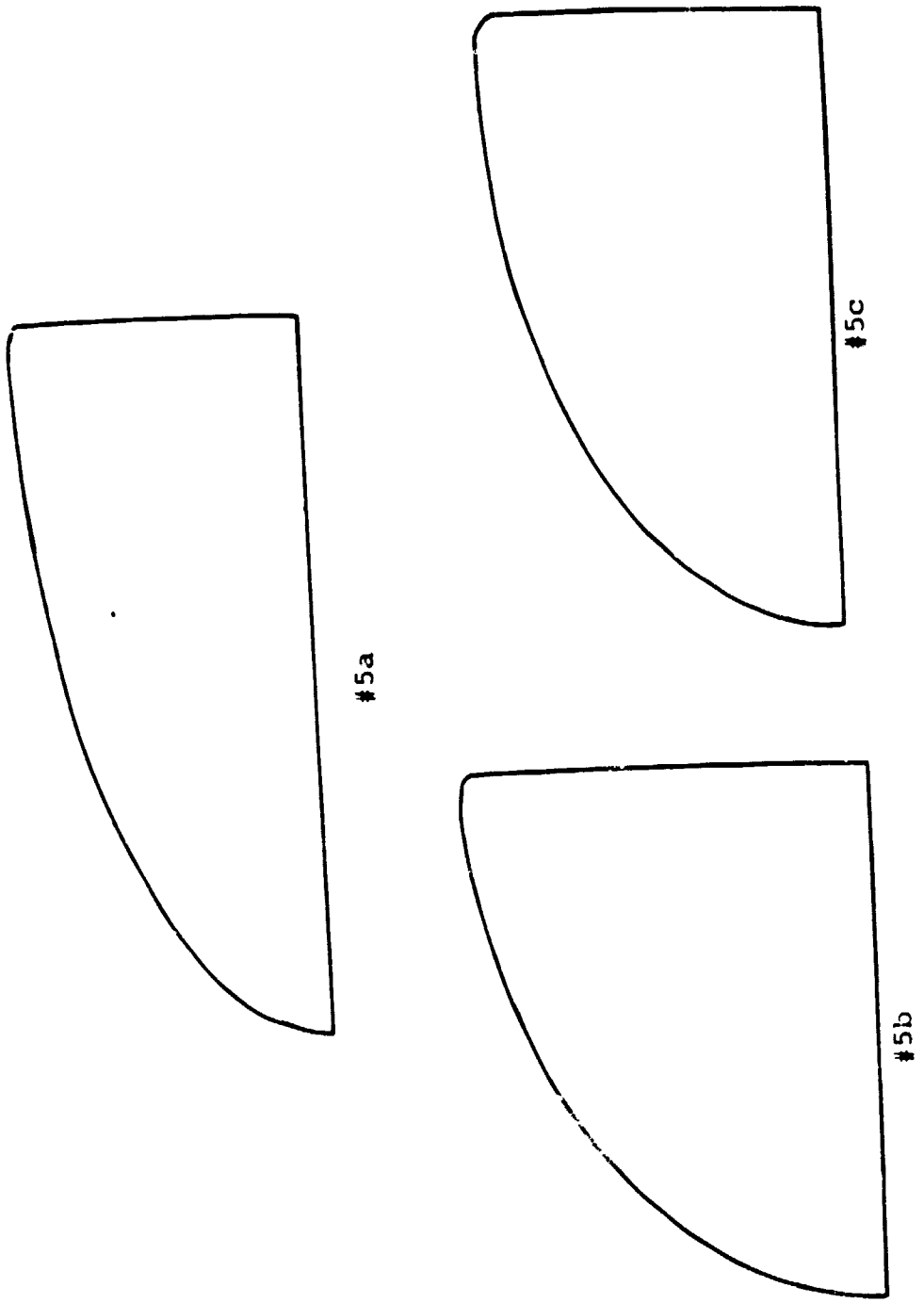
#5a
#5c
#5b

Figure B6. Fin family #6. Fins #6a through #6c have smooth edges and are 0.25 in. thick

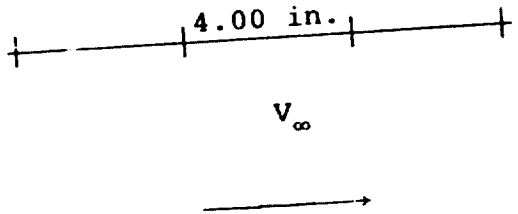

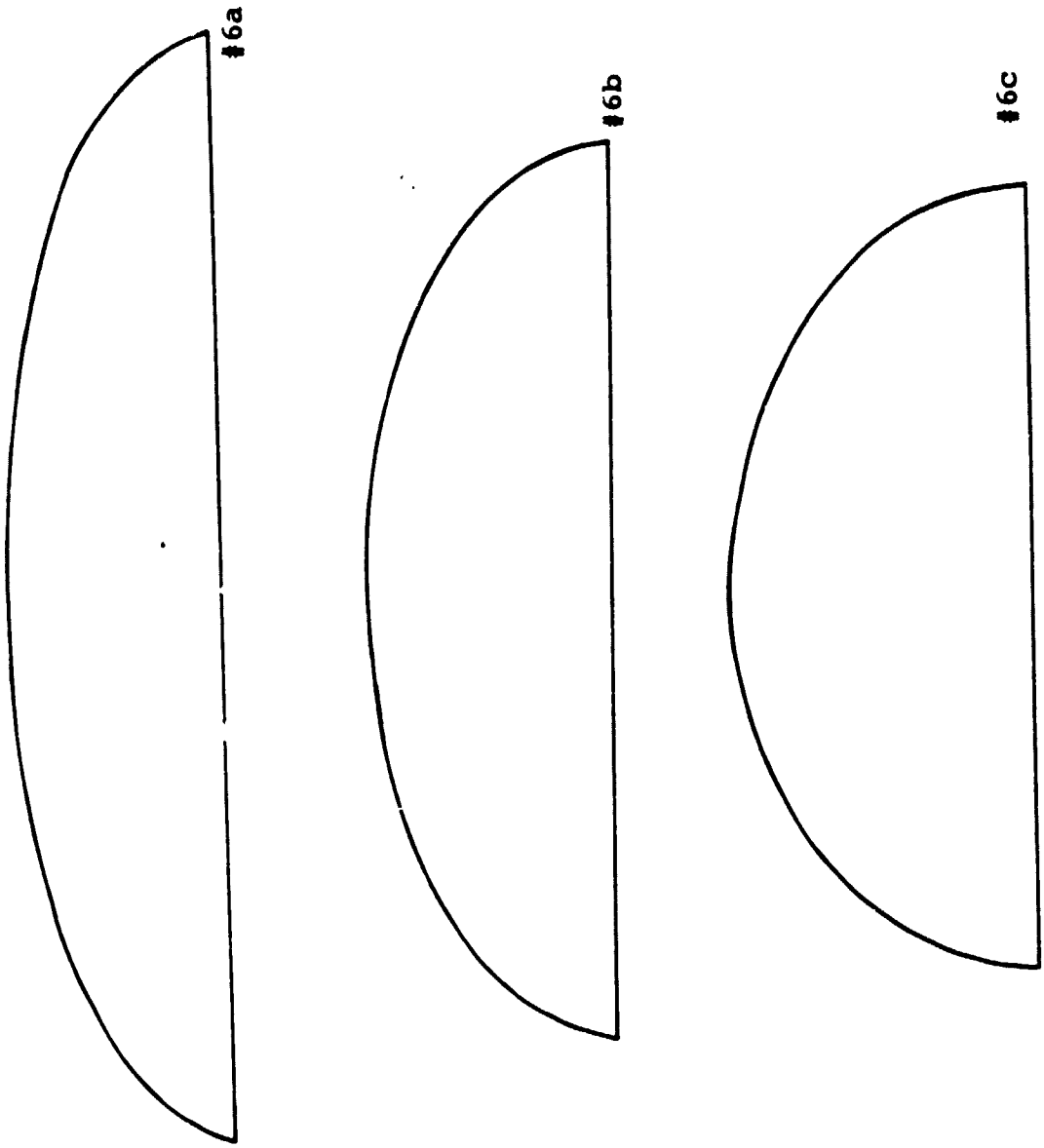
#6a
#6b
#6c

Figure B7. Fin family #7. Fins #7a and #7b have sharp trailing edges, smooth leading and upper edges and the thickness of 0.25 in.

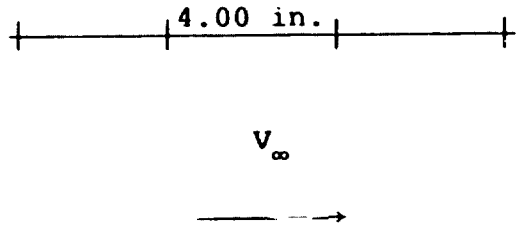

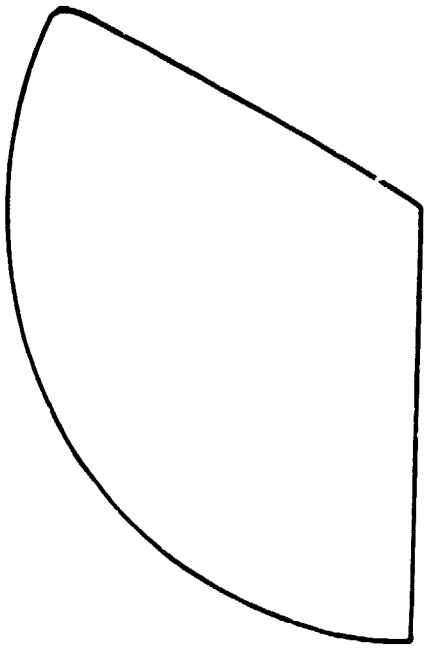

#7b

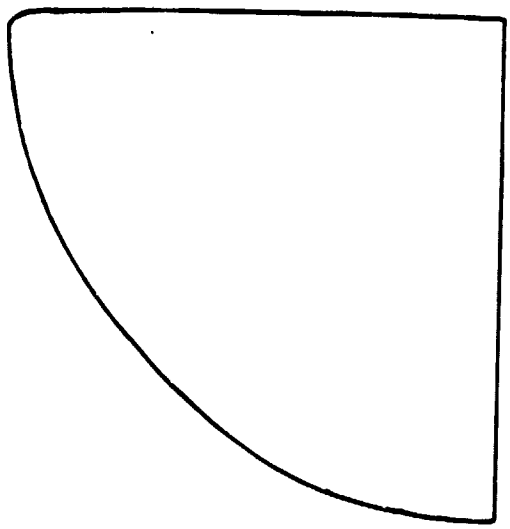

#7a

Figure B8. Fin family #8. Fins #8a through #8e have smooth leading and upper edges, while the trailing edges are sharp at the semi-rectangular and are cornered at the semi-circular trails. Fins family #8 are all 0.25 in. thick

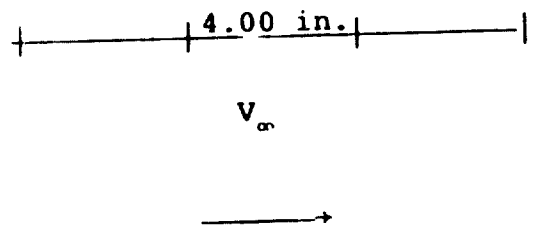

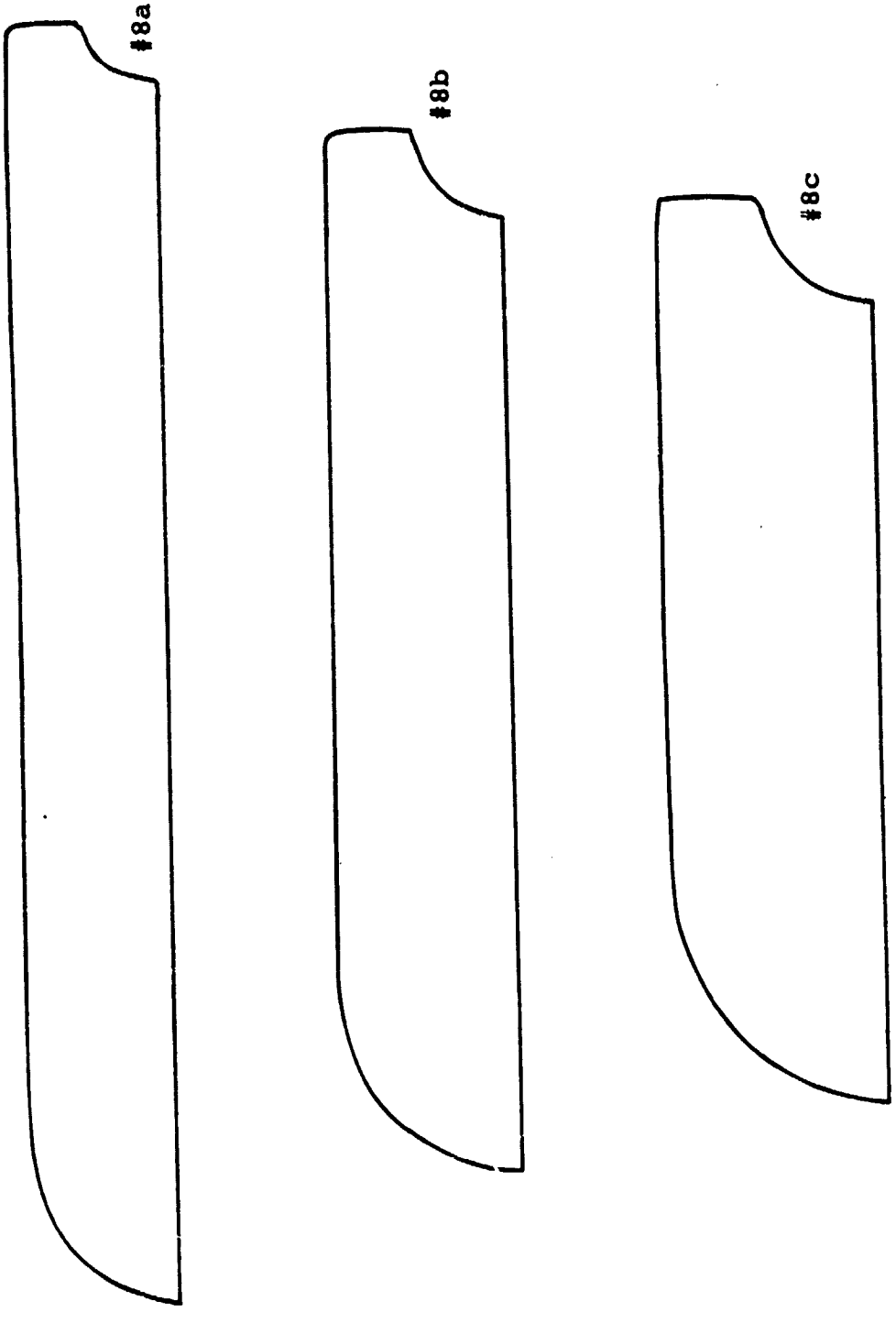
#8a
#8b
#8c

Figure B8 (Continued)

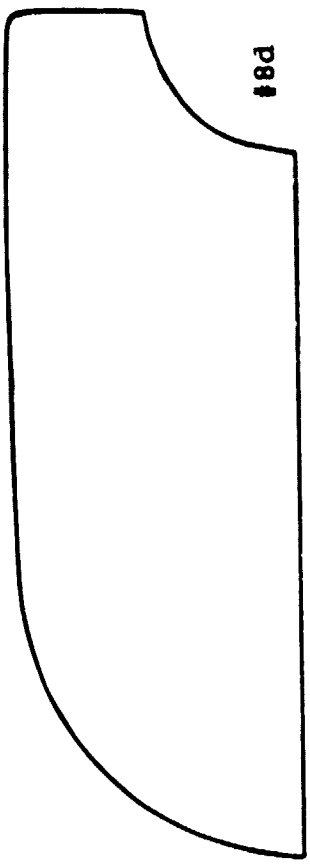
#8d

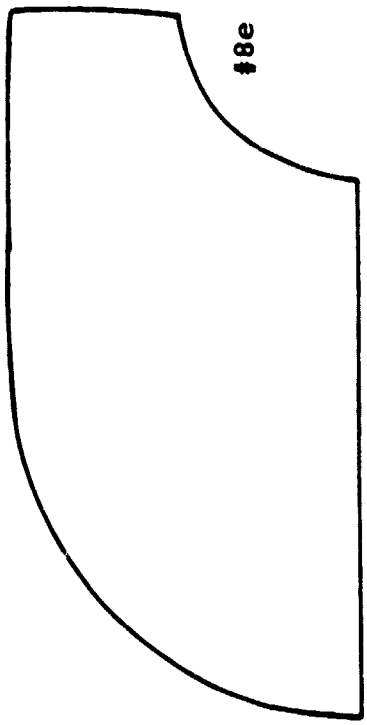
#8e

Figure B9. Fin family #9 (Fin #9a, 9b, 9c and 9d are all NACA fins)
#9a and #9b have Clark Y wing section, #9c and #9d have GAW wing section, #9e has sharp edges, and is 0.0625 in. thick,
#9f has sharp edges, and 5% thick circular arc,
#9g has smooth edges, and is 0.25 in. thick

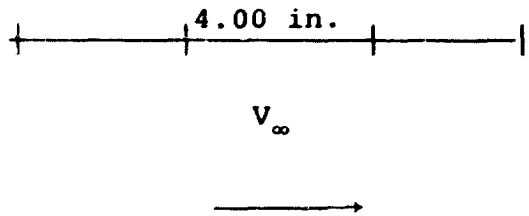

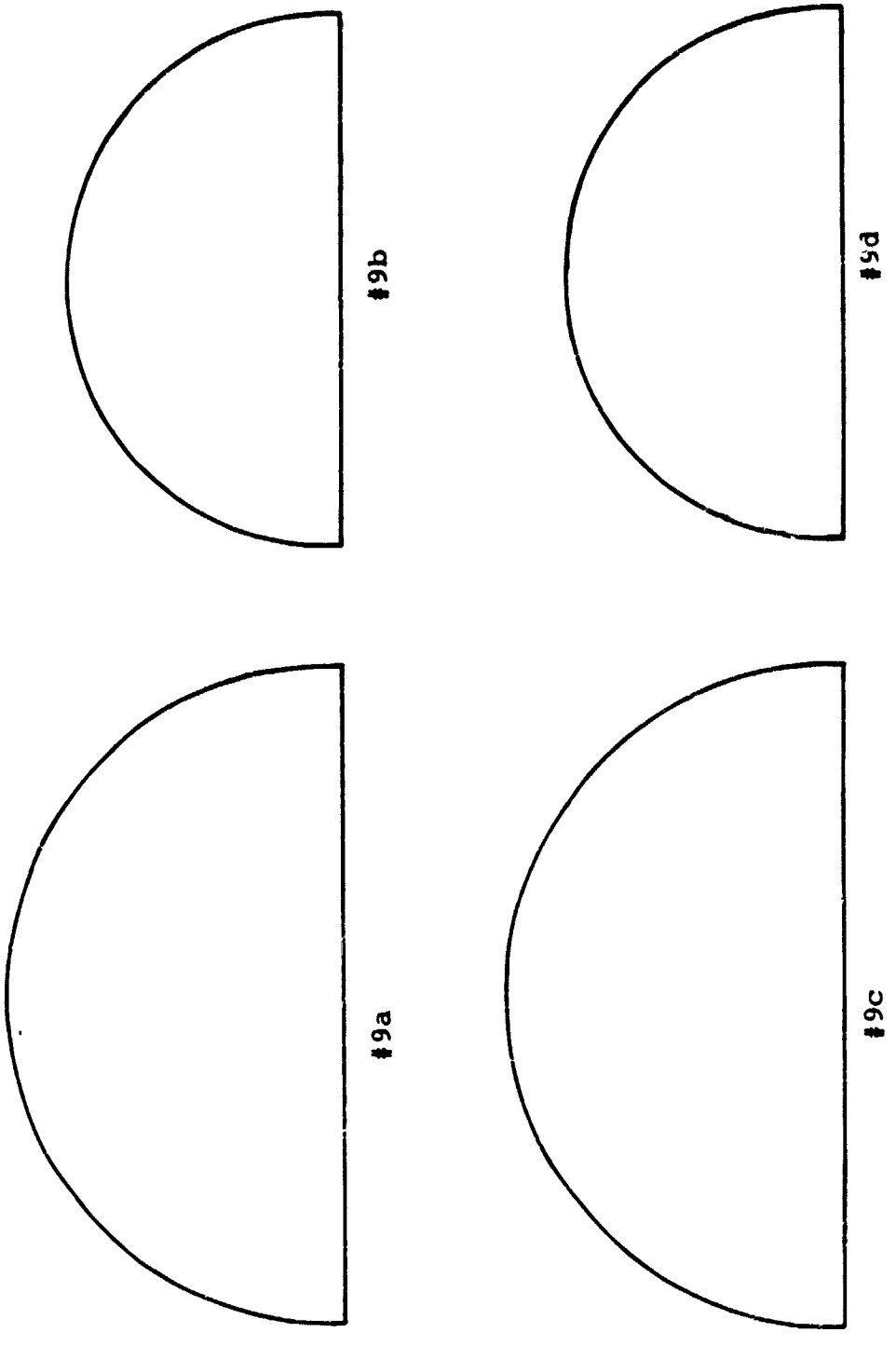
#9b
#9d
#9a
#9c

Figure B9 (Continued)

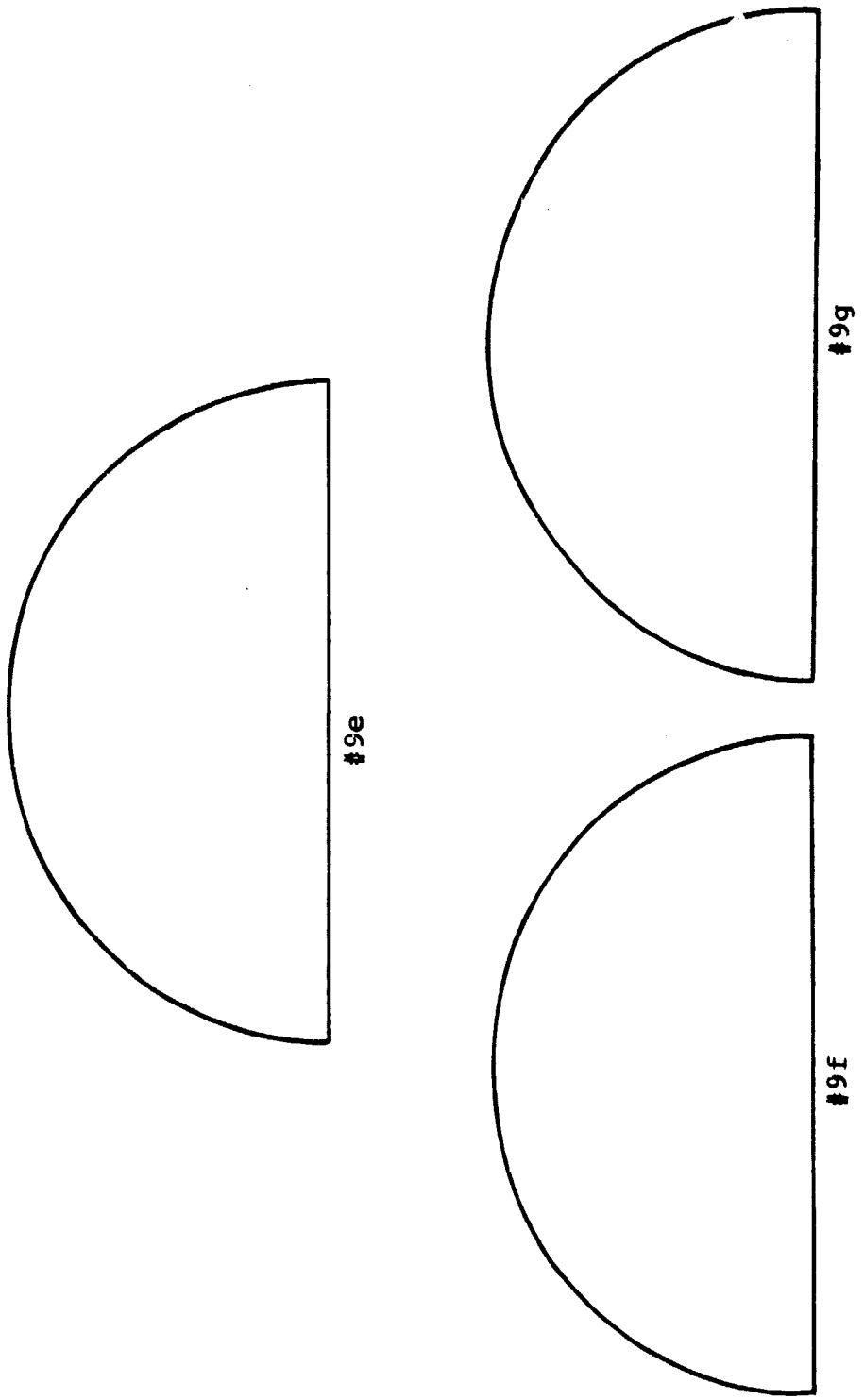
#9e
#9g
#9f

Figure B10. Fin family #10 (NACA fins)
Fins #10a through #10b are 0.0625 in. thick

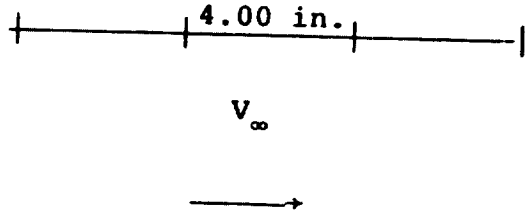

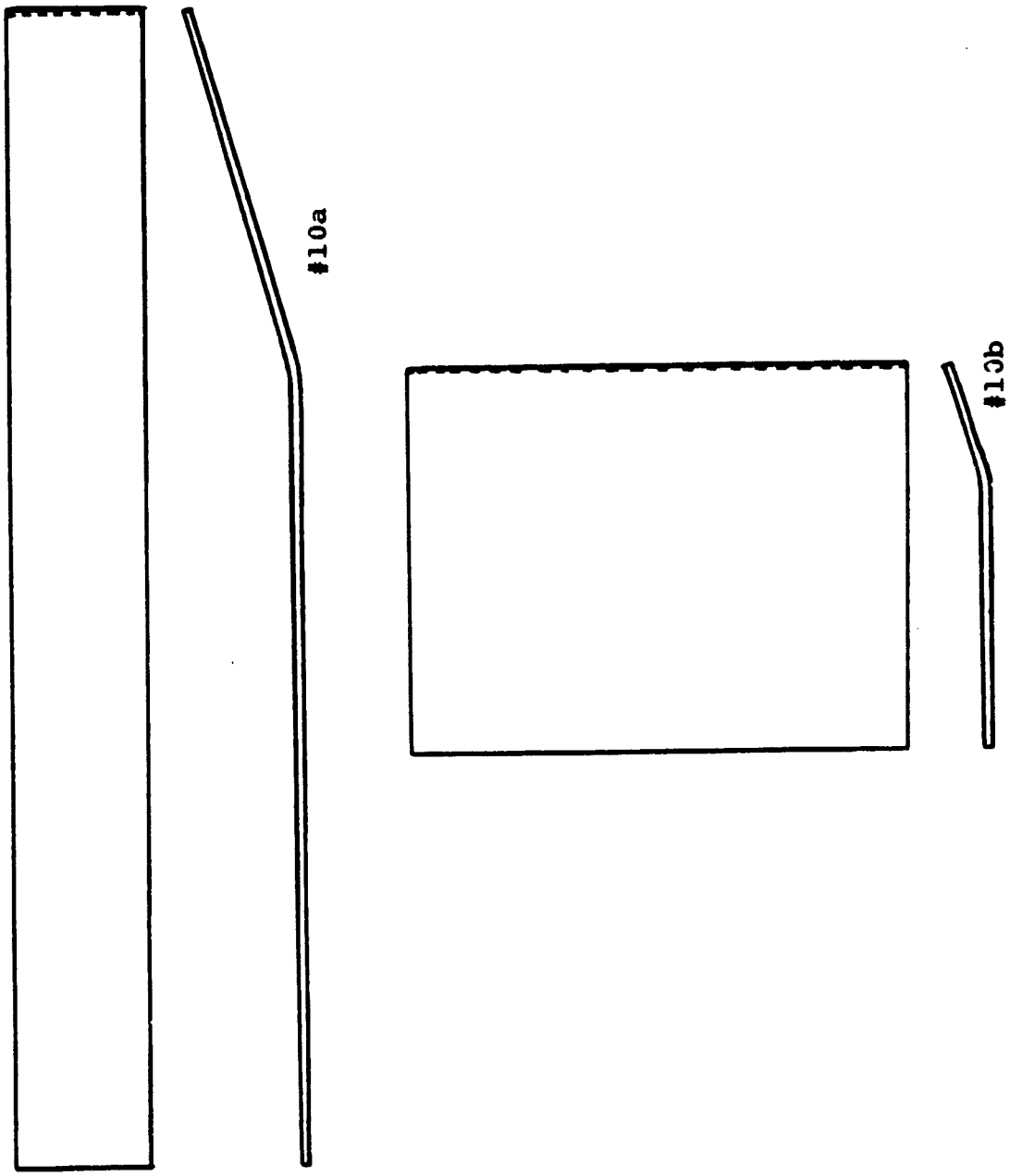
#10a
#13b

Figure B10 (Continued)

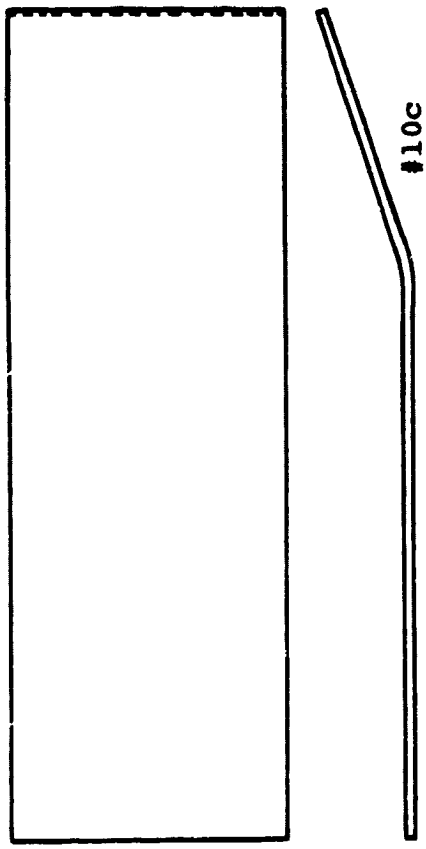
#10c

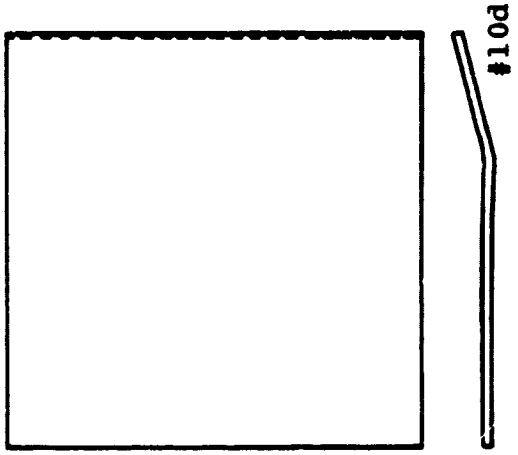
#10d

Figure B11. Fin family #11. Fin #11a is the only one tested from this family. It has sharp trailing edge, smooth leading and upper edges, and it is 0.25 in. thick

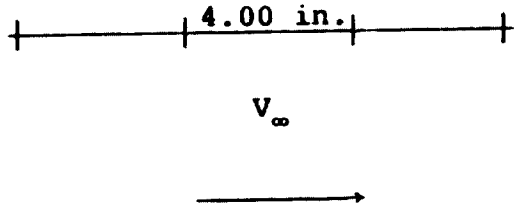

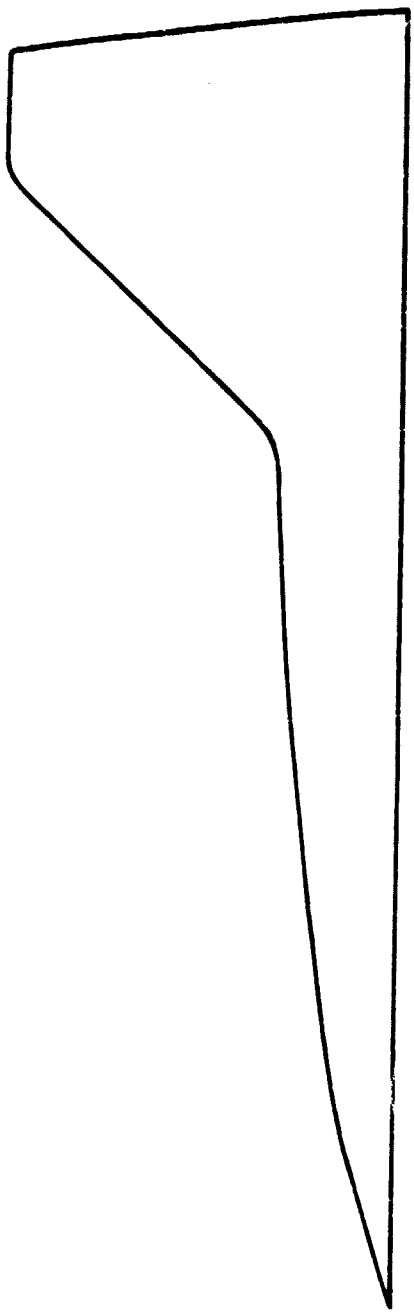

Fig. 11a

Figure A12. Fin family #12. Fin #12a is the only one tested from this family. It has sharp edges and is 0.0625 in. thick

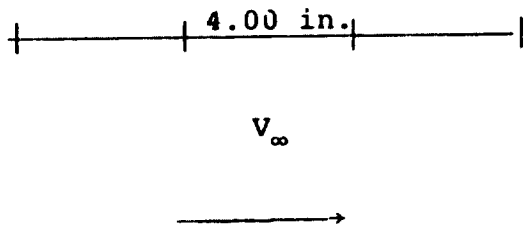

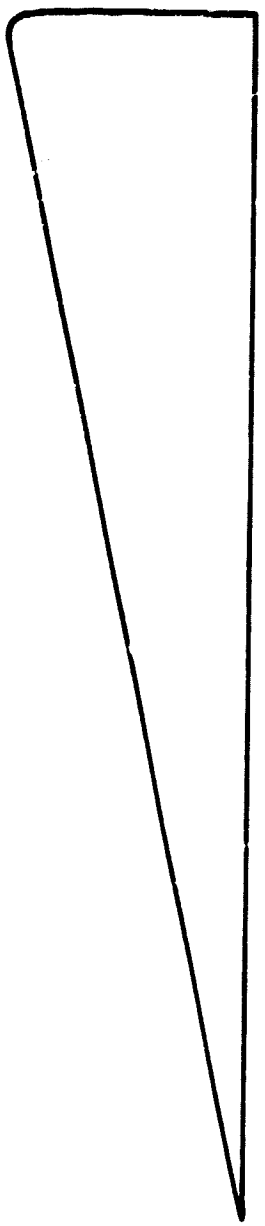
112a

APPENDIX C: ROTOR AND BALANCE DATA ALONG WITH FIN ANGLES OF ATTACK, AREAS AND ASPECT RATIOS

Table C1. The angular velocity to free stream velocity ratios at the corresponding fin angles of attack, area, and aspect ratios

Fin no.	α_F(degree)	S_F (in.^{2})	AR_F	$\frac{\omega}{V_\infty}$ ($\frac{\text{rpm-sec}}{\text{ft}}$)
1a	7	10.020	0.434	5.250
	12	9.990	0.432	8.550
	17	9.850	0.401	10.560
	22	9.780	0.386	9.160
1b	0	9.670	1.476	6.640
	2	9.660	1.478	8.430
	7	9.650	1.478	7.850
	12	9.660	1.478	2.400
1c	0	9.560	1.258	2.720
	2	9.560	1.258	6.030
	7	9.560	1.258	5.630
	12	9.560	1.258	2.700
1d	7	9.850	0.655	6.180
	12	9.850	0.655	10.650
	17	9.820	0.657	9.880
2a	7	10.560	0.734	13.930
	12	10.460	0.729	22.420
	13	10.440	0.728	20.500
	14	10.420	0.727	23.200
	15	10.400	0.726	25.350
	16	10.388	0.725	25.410
	17	10.370	0.724	{29.180 25.510
	18	10.358	0.723	26.120
	19	10.346	0.724	27.200
	20	10.334	0.725	26.170
	21	10.320	0.726	25.880
	22	10.310	0.728	27.850
2b	7	10.890	0.607	15.300
	12	10.750	0.588	21.130
	13	10.720	0.590	21.140
	14	10.690	0.592	22.800
	15	10.660	0.594	25.080
	16	10.630	0.596	27.370
	17	10.600	0.598	{31.840 28.060
	18	10.580	0.595	33.980
	19	10.560	0.592	32.560

Table C1 (Continued)

Fin no.	α_F (degree)	S_F (in.^{2})	AR_F	$\frac{\omega}{V_\infty}$ ($\frac{\text{rpm-sec}}{\text{ft}}$)
2b (cont.)	20	10.540	0.589	27.760
	21	10.520	0.586	
	22	10.500	0.583	24.580
2c	7	10.700	0.469	10.690
	12	10.470	0.468	18.470
	16	10.354	0.460	
	17	10.320	0.459	23.460
	18	10.286	0.456	
	19	10.252	0.453	
	20	10.218	0.450	
	21	10.184	0.446	
	22	10.150	0.443	19.420
	23	10.116	0.439	
2d	7	10.430	0.796	12.400
	12	10.420	0.789	21.900
	13	10.396	0.791	24.890
	14	10.372	0.794	27.230
	16	10.324	0.798	27.610
	17	10.300	0.801	28.300 28.420
	18	10.282	0.800	29.560
	19	10.264	0.799	29.100
	20	10.246	0.748	28.500
	21	10.228	0.797	
	22	10.210	0.796	24.670
2e	13	10.654	0.573	24.950
	14	10.620	0.571	25.370
	15	10.590	0.569	27.000
	16	10.570	0.567	27.730
	17	10.540	0.566	27.310
	18	10.500	0.563	28.780
	19	10.460	0.560	27.960
	20	10.420	0.558	25.300
	21	10.380	0.555	
2f	10	10.660	0.559	28.170
	11	10.650	0.557	31.770
	12	10.640	0.555	32.180
	13	10.610	0.553	32.740
	14	10.590	0.552	35.430
	15	10.570	0.550	35.410

Table C1 (Continued)

Fin no.	α_F (degree)	S_F (in.^{2})	AR_F	$\frac{\omega}{V_\infty}$ ($\frac{\text{rpm-sec}}{\text{ft}}$)
2f (cont.)	16	10.540	0.548	32.970
	17	10.520	0.547	32.140
2g	16	10.530	0.541	26.030
	17	10.500	0.535	28.450
	18	10.480	0.524	30.080
	19	10.440	0.523	30.490
	20	10.400	0.528	27.650
	21	10.360	0.533	
	22	10.320	0.34	
	23	10.280	0.536	
	24	10.240	0.537	
	25	10.200	0.538	
3a	7	10.450	0.398	9.470
	12	10.260	0.387	15.850
	16	10.161	0.396	
	17	10.140	0.398	25.000
	18	10.118	0.395	
	19	10.096	0.393	
	20	10.074	0.390	
	21	10.052	0.387	
	22	10.030	0.385	20.620
	23	10.008	0.382	
3b	2	9.640	1.544	10.650
	7	9.440	1.541	15.200
	12	9.430	1.535	11.770
3c	7	9.930	1.233	14.330
	12	9.910	1.227	14.780
	17	9.910	1.239	3.600
3d	7	10.340	0.631	11.260
	12	10.280	0.621	18.370
	17	10.220	0.618	22.180
	22	10.150	0.603	14.380
4a	7	10.430	0.577	14.090
	12	10.370	0.580	20.250
	16	10.128	0.598	
	17	10.110	0.603	22.700
	18	10.092	0.602	

Table C1 (Continued)

Fin no.	α_F (degree)	S_F (in.^{2})	AR_F	$\frac{\omega}{V_\infty}$ ($\frac{\text{rpm-sec}}{\text{ft}}$)
4a (cont.)	19	10.074	0.602	
	20	10.056	0.601	
	21	10.038	0.600	
	22	10.020	0.600	19.500
4b	7	10.000	0.863	12.960
	12	9.900	0.872	19.740
	14	9.860	0.879	
	15	9.840	0.883	
	16	9.820	0.887	
	17	9.800	0.891	23.580
	18	9.784	0.890	
	19	9.768	0.889	
	22	9.720	0.888	24.270
4c	7	9.950	1.003	14.890
	12	9.860	1.012	21.700
	17	9.778	1.021	19.080
4d	7	9.940	1.369	18.700
	12	9.910	1.374	19.060
	17	9.890	1.377	17.540
4e	7	9.760	1.825	16.670
	12	9.740	1.828	18.440
	17	9.740	1.828	18.610
5a	7	9.560	1.076	13.190
	12	9.510	1.067	20.220
	17	9.500	1.068	17.550
	22	9.460	1.055	5.510
5b	2	9.975	2.030	12.150
	7	9.970	2.030	12.350
	12	9.960	2.020	2.550
5c	2	9.740	1.497	8.800
	7	9.750	1.488	18.150
	12	9.740	1.500	1.950
6a	7	10.470	0.475	13.060
	12	10.390	0.479	18.980
	15	10.312	0.483	
	16	10.286	0.484	

Table C1 (Continued)

Fin no.	α_F (degree)	S_F (in.^{2})	AR_F	$\frac{\omega}{V_\infty}$ ($\frac{rpm\text{-}sec}{ft}$)
6a (cont.)	17	10.260	0.485	21.390
	18	10.248	0.486	
	19	10.236	0.486	
	22	10.200	0.488	23.860
6b	2	9.690	0.713	6.960
	7	9.680	0.714	13.880
	12	9.610	0.719	18.400
6c	2	10.344	0.965	7.050
	7	10.320	0.967	13.440
	12	10.260	0.973	5.520
7a	0	9.800	2.567	9.880
	1	9.800	2.567	
	2	9.800	2.567	14.500
	3	9.800	2.567	
	4	9.800	2.567	
	5	9.800	2.567	
	6	9.800	2.567	
	7	9.800	2.567	4.320
	12	9.790	2.570	1.850
7b	2	9.516	1.911	11.100
	7	9.516	1.911	18.190
	12	9.516	1.911	5.180
8a	7	11.920	0.279	6.090
	12	11.760	0.267	9.460
	17	11.580	0.282	11.210
	22	11.370	0.261	16.120
8b	7	10.850	0.401	5.610
	12	10.790	0.399	9.680
	17	10.720	0.402	8.210
	22	10.660	0.396	8.950
8c	7	10.810	0.552	7.340
	12	10.800	0.551	12.600
	17	10.710	0.555	12.970

Table C1 (Continued)

Fin no.	α_F (degree)	S_F (in.^{2})	AR_F	$\frac{\omega}{V_\infty}$ ($\frac{\text{rpm-sec}}{\text{ft}}$)
8d	2	10.870	0.830	8.600
	7	10.870	0.835	15.970
	12	10.850	0.822	7.650
8e	2	9.930	1.243	7.680
	7	9.940	1.241	10.650
	12	9.930	1.243	2.500
9a	7	10.660	1.323	20.500
	10	10.660	1.323	25.370
	11	10.655	1.324	29.600
	12	10.650	1.325	{31.770 32.280
	13	10.650	1.325	33.160
	14	10.650	1.325	24.020
	17	10.650	1.325	2.940
9b	7	7.00	1.328	{20.700 19.490
	8	7.00	1.328	20.120
	9	7.00	1.328	21.650
	10	7.00	1.328	21.820
	11	7.00	1.328	22.620
	12	7.00	1.328	{21.900 23.090
	13	7.00	1.328	24.320
	14	7.00	1.328	26.840
	15	7.00	1.328	27.880
	17	7.00	1.328	2.191
9c	2	10.770	1.341	13.530
	7	10.770	1.341	19.580
	10	10.770	1.341	22.000
	11	10.765	1.342	25.050
	12	10.760	1.324	{27.280 27.180
	13	10.760	1.342	14.950
	14	10.760	1.342	
	17	10.760	1.342	4.450

Table C1 (Continued)

Fin no.	α_F (degree)	S_F (in.^{2})	AR_F	$\frac{\omega}{V_\infty}$ ($\frac{\text{rpm-sec}}{\text{ft}}$)
9d	7	6.860	1.355	15.000
	12	6.850	1.357	19.750
	17	6.850	1.357	4.310
9e	2	9.650	1.328	12.550
	3	9.640	1.329	13.520
	4	9.640	1.329	14.070
	5	9.640	1.329	13.670
9f	5	9.700	1.305	14.900
	6	9.700	1.305	16.890
	7	9.690	1.306	17.750
	8	9.690	1.306	19.250
	9	9.680	1.307	15.290
9g	2	9.890	1.274	7.570
	7	9.880	1.281	18.150
	12	9.880	1.281	3.380
10a	7	10.350	0.325	17.020
	12	10.250	0.318	22.870
	17	10.150	0.300	11.540
10b	-2	11.850	2.704	16.670
	0	11.850	2.700	20.160
	2	11.840	2.706	13.900
10c	7	12.470	0.724	18.020
	12	12.410	0.706	21.920
	17	12.380	0.706	5.140
10d	-2	9.075	2.088	15.450
	0	9.075	2.084	16.130
	2	9.074	2.079	13.970
11a	7	11.550	1.568	8.920
	12	11.380	1.565	12.250
	17	11.240	1.584	14.750
	22	11.020	1.566	7.190

Table C1 (Continued)

Fin no.	α_F(degee)	S_F (in.^{2})	AR_F	$\frac{\omega}{V_\infty}$ ($\frac{\text{rpm-sec}}{\text{ft}}$)
12a	13	8.418	0.805	
	16	8.334	0.800	
	19	8.224	0.793	
	20.5	8.164	0.790	
	22	8.104	0.788	
	23	8.064	0.785	

Table C2. The force and moment[a] components on the follower aircraft model

Fin no.	α_F (degree)	X (lbs)	Y (lbs)	Z(lbs)	L(in.lb)	M(in.lb)	N(in.lb)
2a	16	-0.0154	-0.0265	0.0195	0.1262	0.0481	-0.0287
	17	-0.0077	-0.0235	0.0271	0.1345	0.0618	-0.0503
	18	0.0077	-0.0176	0.0224	0.1345	0.0653	-0.0575
	19	-0.0231	-0.0067	0.0208	0.1399	0.0687	-0.0431
	20	-0.0231	-0.0307	0.0332	0.1345	0.1031	-0.0611
	21	-0.0308	0.0033	0.0458	0.1317	0.1340	-0.0431
2b	16	0.0539	-0.0016	0.0239	0.1345	0.0825	-0.0431
	17	0.0308	-0.0042	0.0288	0.1454	0.0653	-0.0575
	18	0.0616	-0.0639	0.0129	0.1482	0.0721	-0.0179
	19	0.0770	-0.0015	0.0291	0.1455	0.0825	-0.0179
	20	0.0308	-0.0608	0.0254	0.1455	0.0859	-0.0647
	21	0.0154	-0.0271	0.0427	0.1345	0.0687	-0.0107
2c	16	-0.0308	-0.0075	0.0315	0.1317	0.0584	-0.0323
	17	0.0000	-0.0258	0.0416	0.1317	0.0825	-0.0934
	18	0.0231	0.0093	0.0103	0.1345	0.0962	0.0179
	19	0.0000	-0.0136	0.0491	0.1345	0.0653	-0.0287
	20	0.0231	-0.0154	0.0532	0.1345	0.1031	-0.0395
	21	0.0385	-0.0303	0.0455	0.1317	0.1375	-0.0647
	22	0.0077	-0.0291	0.0343	0.1317	0.0687	-0.0467
	23	-0.0231	-0.0161	0.0614	0.1262	0.1031	-0.0072
2d	16	0.0077	-0.0089	0.0303	0.1317	0.1065	-0.0323
	17	-0.0154	-0.0244	0.0447	0.1317	0.0825	-0.0251
	18	-0.0154	-0.0228	0.0367	0.1317	0.1065	-0.0359
	19	0.0154	0.0006	0.0324	0.1345	0.0756	0.0071
	20	0.0143	0.0187	0.0602	0.1372	0.1031	0.0539
	21	-0.0308	0.0161	0.0549	0.1372	0.1100	0.0827
	22	0.0077	0.0088	0.0306	0.1345	0.0893	0.0359
2e	16	-0.0154	-0.0071	0.0236	0.1372	0.0653	-0.0323
	17	-0.0231	-0.0149	0.0301	0.1399	0.0859	-0.0359
	18	-0.0308	-0.0133	0.0438	0.1399	0.0584	-0.0503
	19	-0.0231	-0.0266	0.0297	0.1399	0.0515	-0.0467
	20	-0.0077	-0.0198	0.0342	0.1454	0.1031	-0.0647
	21	-0.0154	-0.0042	0.0385	0.1290	0.1134	-0.0179
2f	11	0.0616	-0.0039	0.0310	0.1509	0.0756	-0.0683
	12	0.0693	-0.0042	0.0337	0.1537	0.0687	-0.0714
	13	0.0385	-0.0286	0.0263	0.1564	0.0618	-0.0791
	14	0.0308	-0.0367	0.0329	0.1619	0.0653	-0.1042
	15	0.0077	-0.0253	0.0463	0.1647	0.1031	-0.1042
	16	0.0154	-0.0199	0.0443	0.1619	0.0962	-0.1042

[a]See Figure C1.

Table C2 (Continued)

Fin no.	α_F (degree)	S(lbs)	Y(lbs)	Z(lbs)	L(in.lb)	M(in.lb)	N(in.lb)
2g	16	-0.0077	-0.0347	0.0263	0.1372	0.0481	-0.0539
	17	0.0077	-0.0051	0.0219	0.1427	0.0378	-0.0179
	18	0.0153	-0.0153	0.0329	0.1455	0.0653	-0.0575
	19	0.0000	-0.0251	0.0286	0.1482	0.0996	-0.0611
	20	0.0154	-0.0121	0.0505	0.1482	0.1134	-0.0575
	21	-0.0077	-0.0197	0.0619	0.1482	0.1581	-0.0467
	22	0.0077	-0.0227	0.0467	0.1509	0.1031	-0.0898
	23	-0.0077	-0.0306	0.0331	0.1537	0.1065	-0.0647
	24	0.0000	-0.0476	0.0321	0.1537	0.1065	-0.0071
	25	0.0385	-0.0382	0.0320	0.1098	0.1478	-0.0107
3a	16	0.0077	-0.0118	0.0377	0.1180	0.1065	-0.0503
	17	0.0077	-0.0063	0.0256	0.1235	0.0996	-0.0215
	18	0.0077	-0.0121	0.0177	0.1262	0.0756	-0.0251
	19	0.0000	-0.0204	0.0195	0.1290	0.0653	-0.0431
	20	0.0077	-0.0200	0.0218	0.1345	0.0859	-0.0395
	21	0.0077	-0.0254	0.0313	0.1345	0.0962	-0.0539
	22	0.0000	-0.0119	0.0352	0.1317	0.1031	-0.0395
	23	0.0000	-0.0176	0.0399	0.1290	0.1065	-0.0323
4a	16	0.0000	-0.0359	0.0299	0.1180	0.1031	-0.0683
	17	-0.0154	-0.0122	0.0355	0.1180	0.0996	-0.0215
	18	-0.0077	-0.0208	0.0299	0.1207	0.0687	-0.0395
	19	0.0000	-0.0352	0.0620	0.1207	0.0790	-0.0683
	20	-0.0154	-0.0206	0.0297	0.1235	0.0687	-0.0611
	21	0.0154	-0.0117	0.0224	0.1207	0.0859	-0.0539
	22	-0.0154	-0.0201	0.0219	0.1153	0.0928	-0.0143
4b	14	0.0077	-0.0075	0.0239	0.1180	0.0481	-0.0359
	15	0.0077	-0.0038	0.0360	0.1180	0.0859	-0.0719
	16	-0.0077	-0.0148	0.0249	0.1262	0.0790	-0.0467
	17	0.0231	-0.0087	0.0300	0.1290	0.1031	-0.0467
	18	0.0154	-0.0121	0.0303	0.1262	0.0893	-0.0395
	19	0.0154	-0.0042	0.0237	0.1207	0.0721	-0.0287
6a	15	0.0000	-0.0199	0.0293	0.1153	0.1031	-0.0359
	16	0.0000	-0.0176	0.0375	0.1153	0.1190	-0.0072
	17	0.0077	-0.0172	0.0312	0.1207	0.0962	0.0359
	18	-0.0077	-0.0125	0.0205	0.1235	0.0687	-0.0179
	19	0.0000	-0.0060	0.0403	0.1125	0.1375	-0.0359
7a	0	0.0077	0.0101	0.0498	0.0631	0.1547	0.0072
	1	0.0000	-0.0133	0.0517	0.0686	0.1822	-0.0323
	2	0.0077	-0.0110	0.0447	0.0796	0.1581	-0.0251
	3	0.0077	-0.0001	0.0483	0.0796	0.1650	-0.0179
	4	0.0077	-0.0145	0.0400	0.0768	0.1203	-0.0251

Table C2 (Continued)

Fin no.	α_F (degree	S(lbs)	Y(lbs)	Z(lbs)	L(in.lb)	M(in.lb)	N(in.lb)
7a	5	0.0000	-0.0120	0.0505	0.0741	0.1443	-0.0072
	6	0.0000	0.0096	0.0427	0.0713	0.1340	0.0323
	7				0.0329		
9a	10	0.0154	-0.0175	0.0247	0.1345	0.0721	-0.0611
	11	0.0231	-0.0156	0.0281	0.1372	0.0481	-0.0539
	12	0.0077	-0.0121	0.0277	0.1345	0.0637	-0.0791
	13	0.0154	-0.0056	0.0249	0.1345	0.1100	-0.0611
	14	0.0154	-0.0139	0.0193	0.1317	0.0962	-0.0575
9b	7	0.0077	-0.0116	0.0274	0.1125	0.0962	-0.0539
	8	0.0000	-0.0260	0.0368	0.1153	0.0996	-0.0179
	9	-0.0154	-0.0178	0.0249	0.1180	0.0687	-0.0431
	10	-0.0231	-0.0050	0.0319	0.1207	0.0548	-0.0179
	11	-0.0307	-0.0009	0.0336	0.1290	0.1031	-0.0431
	12	-0.0154	-0.0121	0.0378	0.1290	0.0893	-0.0683
	13	-0.0231	-0.0065	0.0483	0.1262	0.1031	-0.0791
	14	-0.0077	-0.0256	0.0290	0.1235	0.1065	-0.0072
9c	10	0.0770	-0.0116	0.0274	0.1262	0.0928	-0.0647
	11	0.1001	-0.0125	0.0356	0.1317	0.0721	-0.0611
	12	0.0770	-0.0113	0.0448	0.1372	0.1237	-0.0791
	13	0.0539	-0.0094	0.0507	0.1345	0.1065	-0.0683
	14	0.0115	-0.0139	0.0217	0.1290	0.0893	-0.0698
12a	13	0.0000	-0.0391	0.0301	0.1070	0.1031	-0.0287
	16	-0.0154	-0.0230	0.0242	0.1125	0.0225	-0.0359
	19	0.0000	-0.0184	0.0380	0.1152	0.0859	-0.0035
	20.5	0.0000	-0.0120	0.0278	0.1125	0.1031	0.0000
	22	0.0000	-0.0250	0.0310	0.1125	0.1203	-0.0359
	23	0.0000	-0.0208	0.0378	0.0960	0.1856	-0.0359

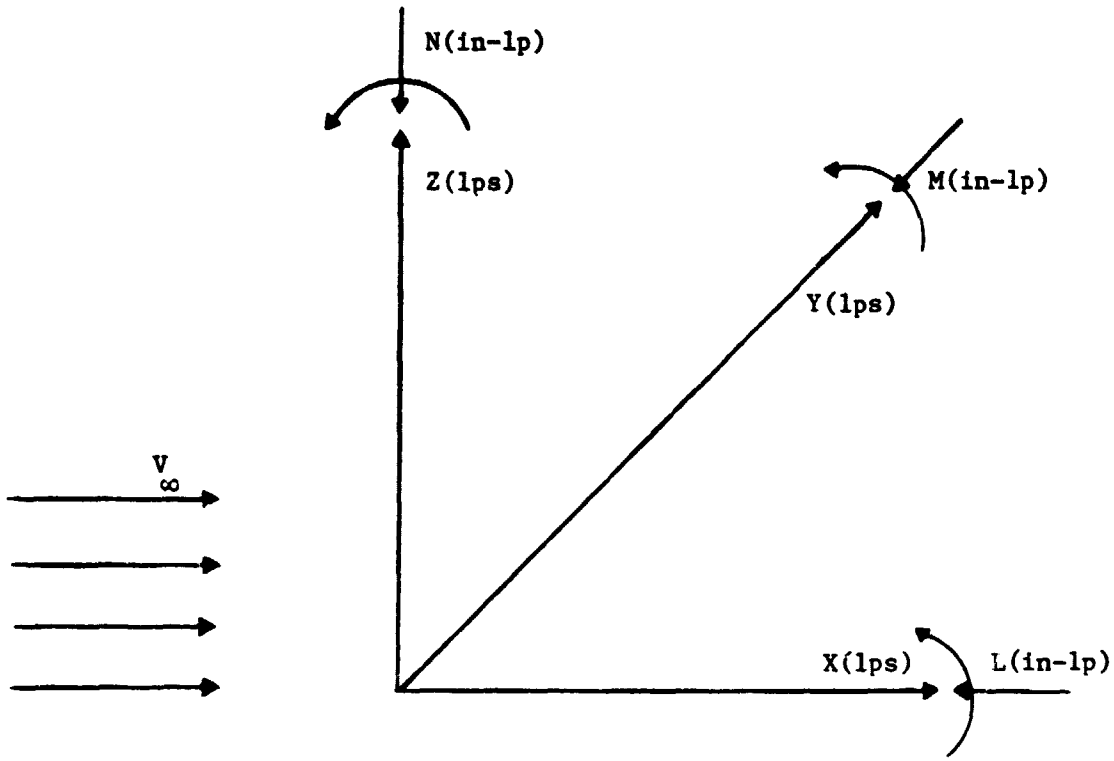

Figure C1. The positive direction of forces and moments of flow on the follower in the wake of the generator

APPENDIX D: VORTEX STRENGTH TERM

For the follower model the change in angle of attach $\Delta\alpha$, due to the tangential and free stream velocities is

$$\Delta\alpha = \frac{u_\theta}{V_\infty} \tag{D1}$$

The lift coefficient changes according to the equation $\Delta c_L = \Delta\alpha\ a_w$ where a_w is the average lift curve slope. Multiplying both sides of this equation by $qc\Delta y$ gives the change in total lift as

$$\Delta \text{ Lift} = \Delta\alpha a_w qc\Delta y$$

or

$$d \text{ lift} = \Delta\alpha a_w qc\ dy. \tag{D2}$$

Since the moment arm is y, then the infinitesimal change in rolling moment can be expressed as

$$dL = \Delta\alpha a_w qcy dy$$

and the total rolling moment as

$$L = \int_{-b/2}^{b/2} \Delta\alpha a_w qcy dy \tag{D3}$$

Equation D3 has to be integrated over the span length b. However, a specific flow behavior has to be assumed in the wake. A Rankine type of vortex has been adopted. Therefore, $u_\theta = K_1 r$ for $r \leq a_c$ and $u_\theta = \frac{K_2}{r}$ for $r \geq a_c$ where K_1 and K_2 are constants and a_c is the core radius. For circulatory

flow without rotation (i.e., for $r \geq a_c$) $K_2 = \frac{\Gamma}{2\pi}$ (30). Therefore, $u_\theta = \frac{\Gamma}{2\pi r}$ for $r \geq a_c$. For $r \leq a_c$ the constant K_1 has to be equal to $\frac{\Gamma}{2\pi a_c^2}$ so that $u_\theta = \frac{\Gamma_0 r}{2\pi a_c^2}$ $(r \leq a_i)$ is equal to $u_\theta = \frac{\Gamma}{2\pi r}$ $(r \geq a_c)$ at $r = a_c$, where Γ_0 is the total circulation.

Putting the value of $\Delta\alpha$ from Equation D1 and $q = \frac{1}{2}\rho V_\infty^2$ into Equation D3 results in the following

$$L = \int_{-b/2}^{b/2} \frac{u_\theta}{V_\infty} a_w \frac{1}{2}\rho V_\infty^2 \, ycdy$$

or

$$L = 2\int_0^{b/2} \frac{a_w \rho V_\infty^2 c}{2V_\infty} [u_\theta y dy] \tag{D4}$$

For a Rankine vortex the above equation takes the form

$$L = a_w \rho V_\infty c\{\int_0^{a_c} \frac{\Gamma_0 y}{2\pi a_c^2} y \, dy + \int_{a_c}^{b/2} \frac{\Gamma_0}{2\pi y} ydy\}$$

or

$$L = a_w \rho V_\infty c \quad \frac{\Gamma_0}{2\pi} \{\frac{b}{2} - \frac{2a_c}{3}\} \tag{D5}$$

since

$$L = \frac{1}{2}\rho V_\infty^2 S b c_\ell \tag{D6}$$

Then the right sides of D6 and D6 are equal and Γ_0 can be found as

$$\Gamma_0 = \frac{V_\infty S b c_\ell \pi}{a_w c [\frac{b}{2} - \frac{2a_c}{3}]} \tag{D7}$$

Dividing the sides of Equation D7 by $V_\infty\sqrt{S_F}$ result in

$$\frac{\Gamma_0}{V_\infty\sqrt{S_F}} = \frac{\pi b}{a_w[\frac{b}{2} - \frac{2a_c}{3}]} \frac{Sc_\ell}{c\sqrt{S_F}}$$

or

$$\frac{\Gamma_0}{V_\infty\sqrt{S_F}} = \frac{\pi}{a_w[\frac{1}{2} - \frac{2a_c}{3b}]} \frac{c_\ell b}{\sqrt{S_F}} \qquad \text{(D8)}$$

The term $\frac{\pi}{a_w[\frac{1}{2} - \frac{2a_c}{3b}]}$ is not known therefore

$$\frac{\Gamma_0}{V_\infty\sqrt{S_F}} \alpha \frac{c_\ell b}{\sqrt{S_F}} \qquad \text{(D9)}$$

On the other hand, it can be shown that c_ℓ is directly proportional to fin area. Since

$$\text{Lift} \approx \rho V_\infty \Gamma_0 b_F \approx c_{L_F} \frac{1}{2}\rho V_\infty^2 S_F$$

therefore

$$\Gamma_0 \approx \frac{c_{L_F} V_\infty S_F}{2b_F}$$

or

$$\Gamma_0 = \frac{K_3 V_\infty S_F}{b_F} \qquad \text{(D10)}$$

where K_3 depends on fin lift and is a constant. While the core radius a_c depends on fin span so that

$$a_c = K_4 b_F \tag{D11}$$

where K_4 is a constant.

Substituting the values of Γ_0 and a_c from Equations D10 and D11 into Equation D5 gives the rolling moment as

$$L = \frac{a_w}{2\pi} \rho V_\infty^2 S_F \frac{cb}{b_F} K_3 \{\frac{1}{2} - \frac{2}{3} \frac{b_F}{b} K_4\} \tag{D12}$$

or in coefficient form

$$c_\ell = \frac{L}{\frac{1}{2}\rho V_\infty^2 Sb} = \frac{a_w}{\pi} \frac{S_F}{S} \frac{c}{b_F} K_3 [\frac{1}{2} - \frac{2}{3} K_4 \frac{b_F}{b}] \tag{D13}$$

Substituting this value of c_ℓ into Equation D9 results in

$$\frac{\Gamma_0}{V_\infty \sqrt{S_F}} \sim K_3 \frac{\sqrt{S_F}}{b_F} [\frac{1}{2} - \frac{2}{3} \frac{b_F}{b} K_4] \tag{D14}$$

which means the vortex term $\frac{\Gamma_0}{V_\infty \sqrt{S_F}}$ depends directly on lift, square root of fin area and inverse of fin span. If different area fins are to be tested Equation D14 should be used instead of D9.

ADDENDUM: EXPERIMENTAL ANALYSIS OF WAKES OF VARIOUS WING FIN CONFIGURATIONS

LIST OF SYMBOLS

A_{S_B}	Small rotor-blade area
A_{L_B}	Large rotor-blade area
a	Core radius
D_L	Large rotor frontal diameter
D_S	Small rotor frontal diameter
P_a	Atmospheric pressure
P_i	Pore pressure
R	Rotor radius
r_1	Radial position with respect to a fixed reference
r	Radial position measured from the center of the vortex
S_F	Fin planform area
V	Wake velocity or free stream velocity
V_∞	Free stream velocity
V_{in}	Wake induced velocity
U_θ	Tangential velocity
Γ	Circulation
θ	Induced angle due to tangential velocity
θ_1	Pitch angle
ΔP	Atmospheric and tunnel static pressure differences
ω	Angular velocity

INTRODUCTION

The purpose of this addendum is to provide additional data to the preceding analysis.

Fourteen aerodynamic fins, which were tested using two different methods (i.e., rotor and force balance methods), were retested. However, since the main goal of the present work is to analyze the wake of each fin and thus provide information on how circulation is spread in the radial direction, a pressure probe was used as a measuring device. Each fin was tested at angles of attack very close to maximum circulation strength. The plots of $U_{\theta/V}$ versus r_1 and $\Gamma/V\sqrt{S_F}$ versus r are presented.

Two different size rotors (in addition to the one rotor used in the preceding analysis) were also used to measure the circulation strength of each vortex. The results of the three rotors, the force balance, and the pressure probe are compared.

Experimental Procedure and Setup

The test procedure and the experimental setup were the same as explained previously, with the following exceptions:

1. When the pressure probe was being used, the tunnel velocity was not changed ($V_\infty \approx 98.5$ ft/sec for every fin tested). Furthermore, while the probe was mounted on the traverse system (as shown in Fig. 1) the traverse system had to be positioned vertically such that the pores of the pressure probe were along the horizontal line going approximately through the center of the corresponding fin vortex. This was

accomplished easily by referring to the raw data obtained during 1979-1980, which contain the vertical and horizontal positions of the vortex center lines of all fins at their tested angles of attack. The pressure probe was then traversed along the horizontal direction in increments of 0.2, 0.3, 0.4 and 0.5 in. This was done for both sides of each vortex wake.

2. A water manometer was used to measure $P_a - P_i$, where $i = 1 \rightarrow 5$ and corresponds to the position of each pore of the pressure probe as shown in Fig. 1.
3. When rotors were used as measuring devices, the tunnel velocity was changed for each fin, so that there were enough data points to plot ω versus V_∞, where ω is rotor angular velocity measured at the center of each vortex. The fins were tested at only one angle of attack. The earlier results were used to choose these angles (these angles are either at, or very close to, optimum).

Data Reduction

As shown in Fig. 1, the pressure probe was mounted at zero pitch angle θ_1 relative to free stream velocity. The pressure pores therefore measured $P_a - P_i$, where P_i is the pressure felt through each pore in the wake ($i = 1 \rightarrow 5$).

The ratio $(P_2 - P_3)/\Delta p$ was chosen to predict the angle θ, shown in Fig. 2. Using the calibration curve of Fig. 3, the ratio $(P_2 - P_3)/\Delta p$

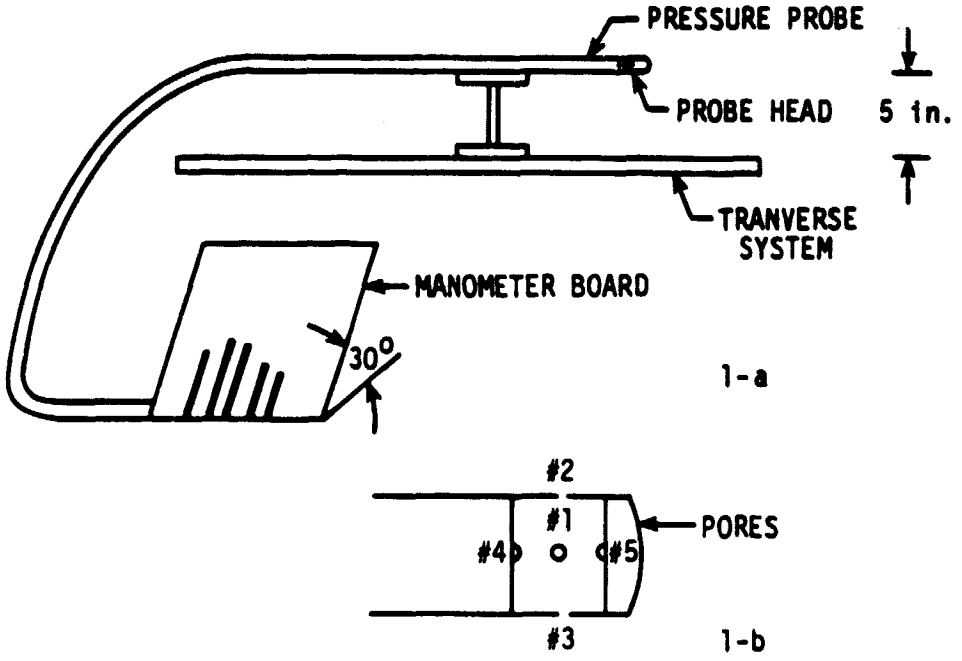

Figure 1. a) The pressure probe mounted on the tranverse system such that free stream velocity is perpendicular to pore #1 ($V_\infty \perp$ to the paper) (i.e., $\theta_1 = 0$).

b) Positions of the pores of the pressure probe (expanded view of the probe head, flow direction into the paper).

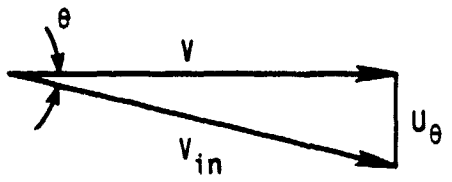

Figure 2. Wake velocity V is induced due to existence of fin vortex tangential velocity U_θ.

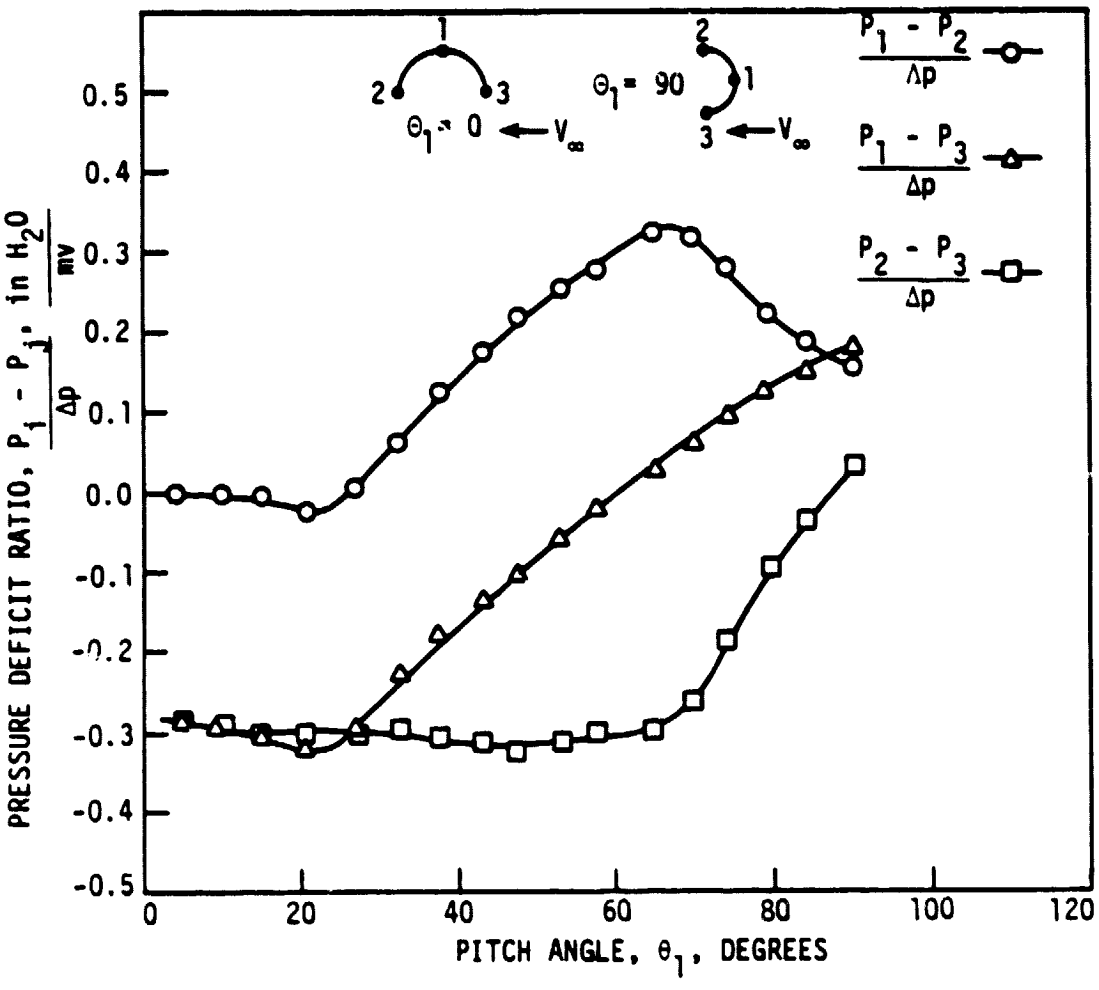

Figure 3. Pressure probe calibration curves.

determines the induced angle θ. This angle exists due to the tangential velocity U_θ in the wake. Since the induced velocity V_{in} and its components U_θ and V are not known, $\tan\theta = U_\theta/V$ is plotted against radial position, instead of U_θ. Figures 4-17 are plots of U_θ/V versus r_1 for the tested fins.

The circulation Γ is equal to $2\pi U_\theta r$ for an axisymmetric vortex flow. Since U_θ is not known, only Γ/V can be calculated; thus $\Gamma/V\sqrt{S_F}$ is plotted against r in Figs. 18-21, where $\Gamma/V\sqrt{S_F}$ is a dimensionless circulation parameter.

Finally, two rotors (D_S = 1.0 in., A_{S_B} = 3.06 × 0.5 in.^{2}, D_L = 6.0 in., A_{L_B} = 2.0 × 3.0 in.^{2}) were used to obtain the data ω versus V_∞ shown in Figs. 22 and 23.

DISCUSSION

Rotors

Table 1 shows that there are inconsistencies between the results of the three rotors and the force balance. This is due to the fact that each vortex has its own circulation distribution and each rotor, depending on its size, has a different degree of stability (as far as ω measurements are concerned, i.e., the smaller the rotor, the harder it is to stabilize). This is illustrated in Table 1 and in Figs. 18-21, where the vortex strength term $\omega S_R/V\sqrt{S_F}$ becomes larger (and rotor velocity at the same time becomes more stable) as the blade frontal area increases.

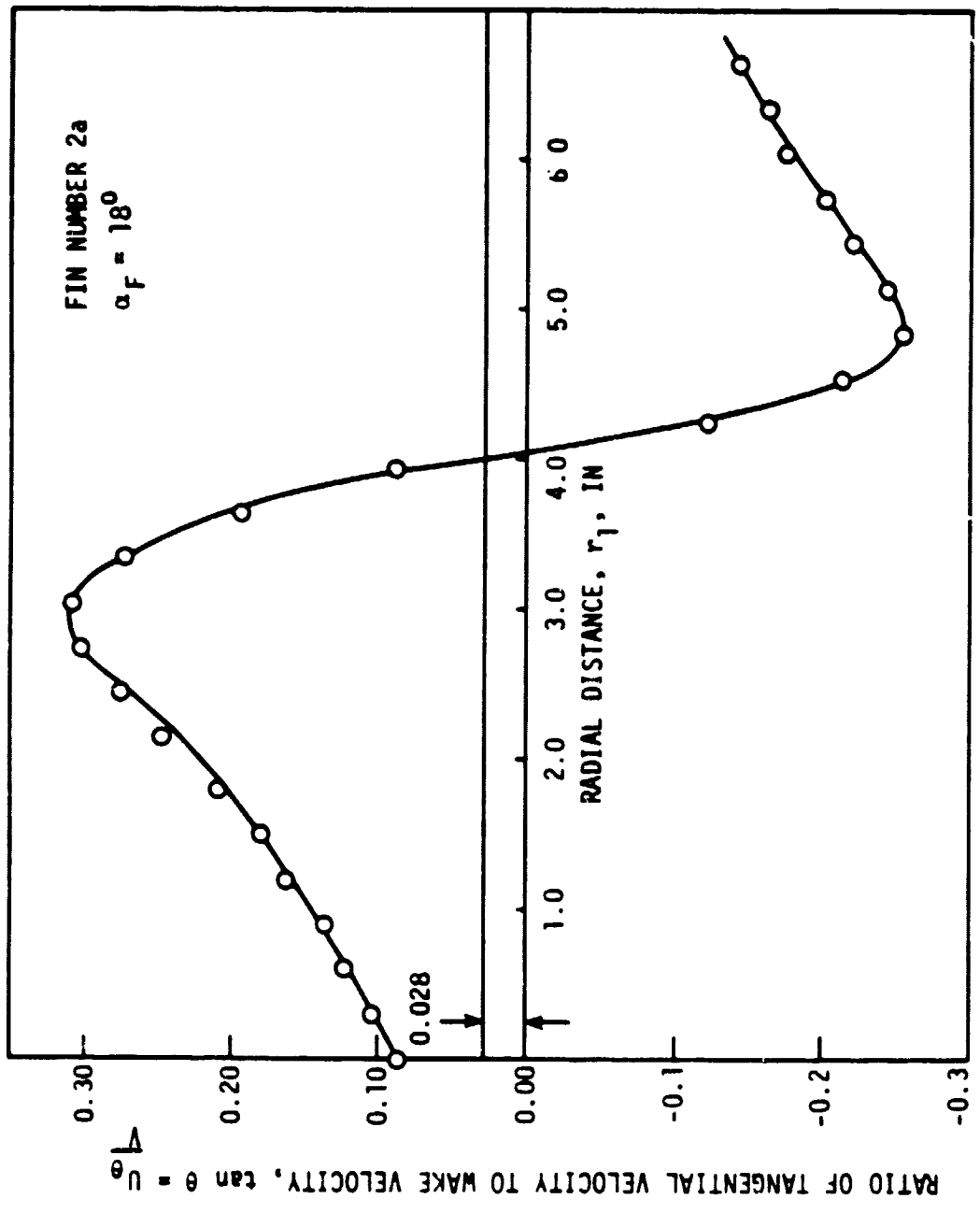

Figure 4. Tangential velocity versus fin vortex radius.

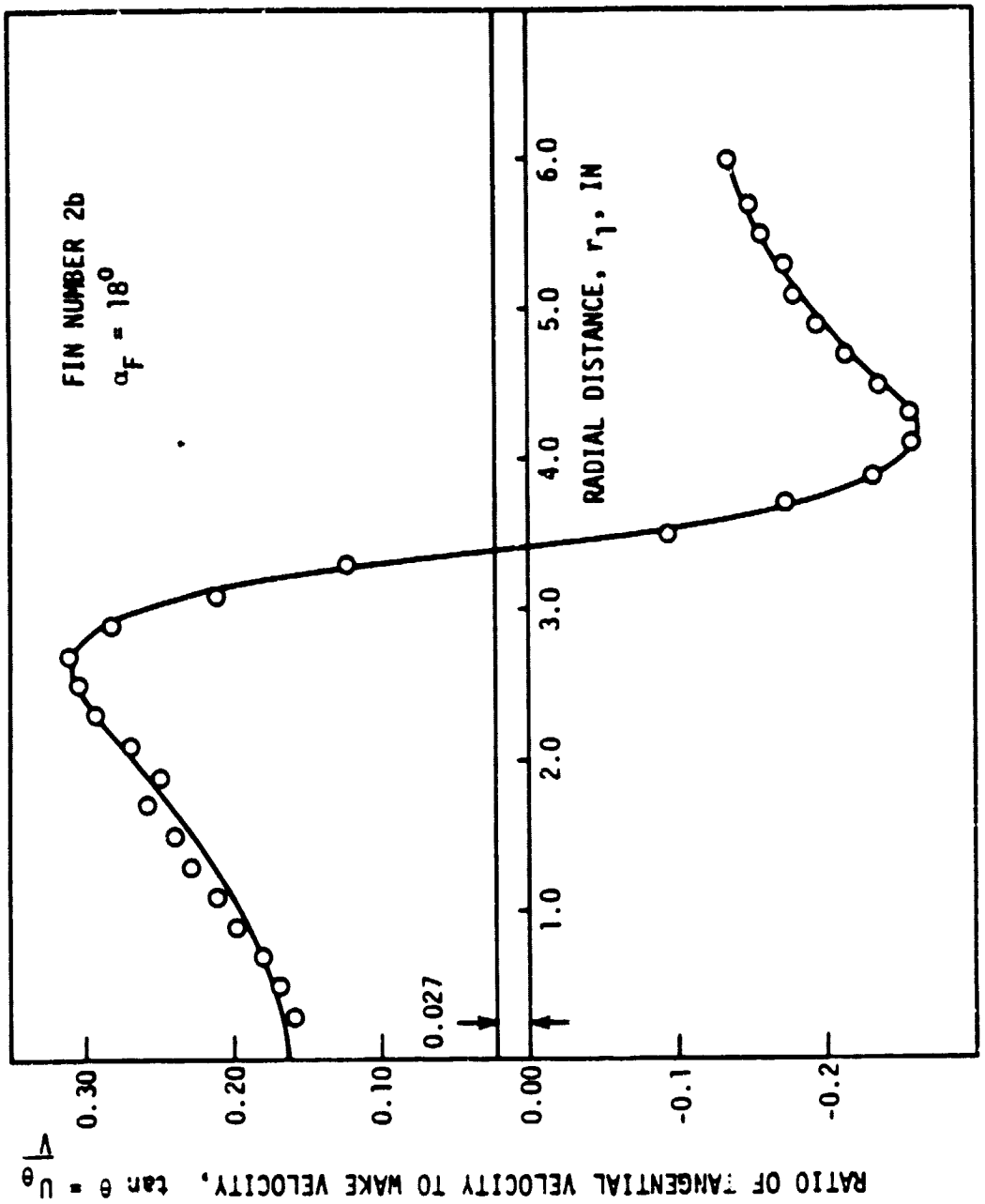

Figure 5. Tangential velocity versus fin vortex radius.

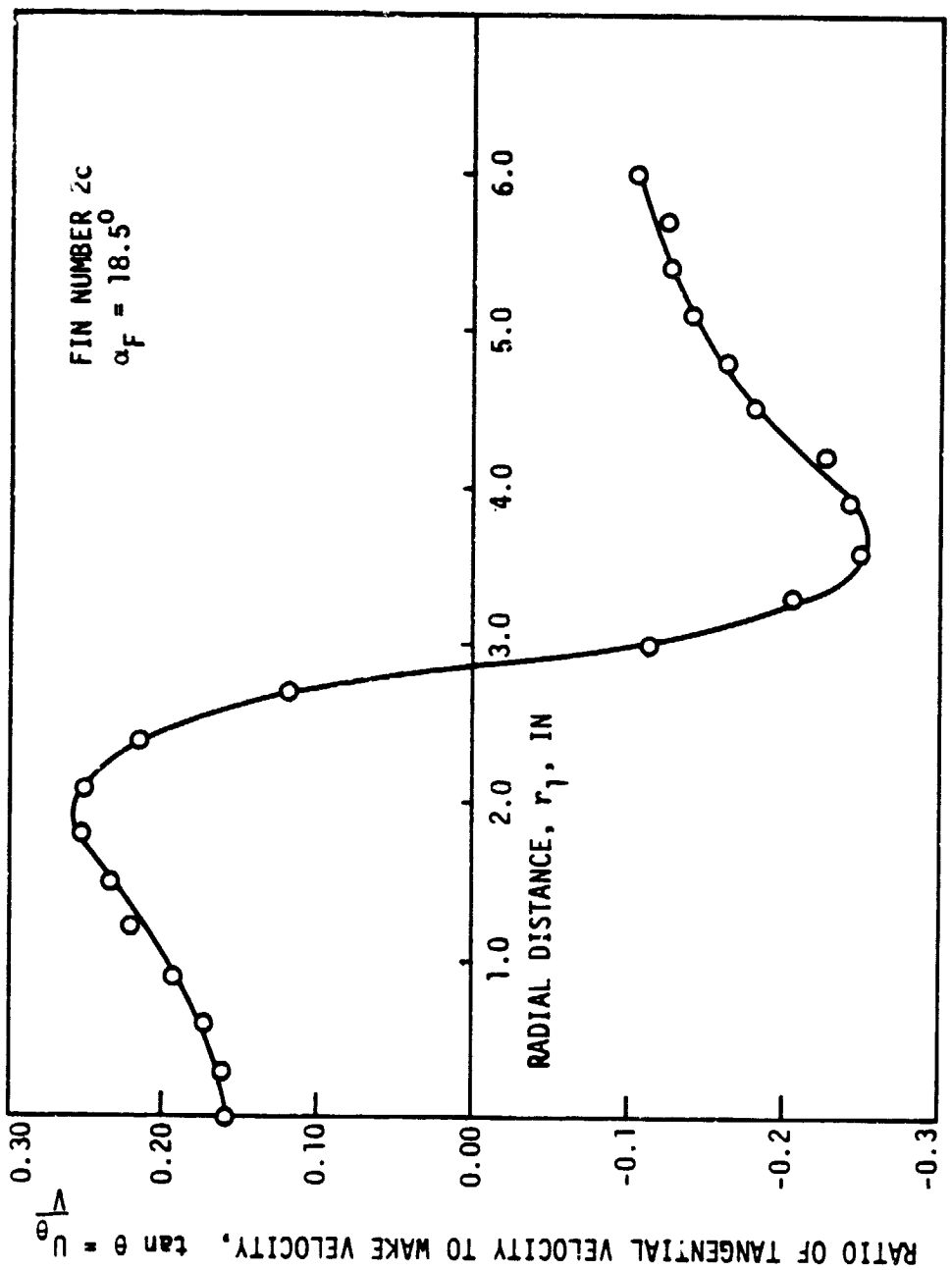

Figure 6. Tangential velocity versus fin vortex radius.

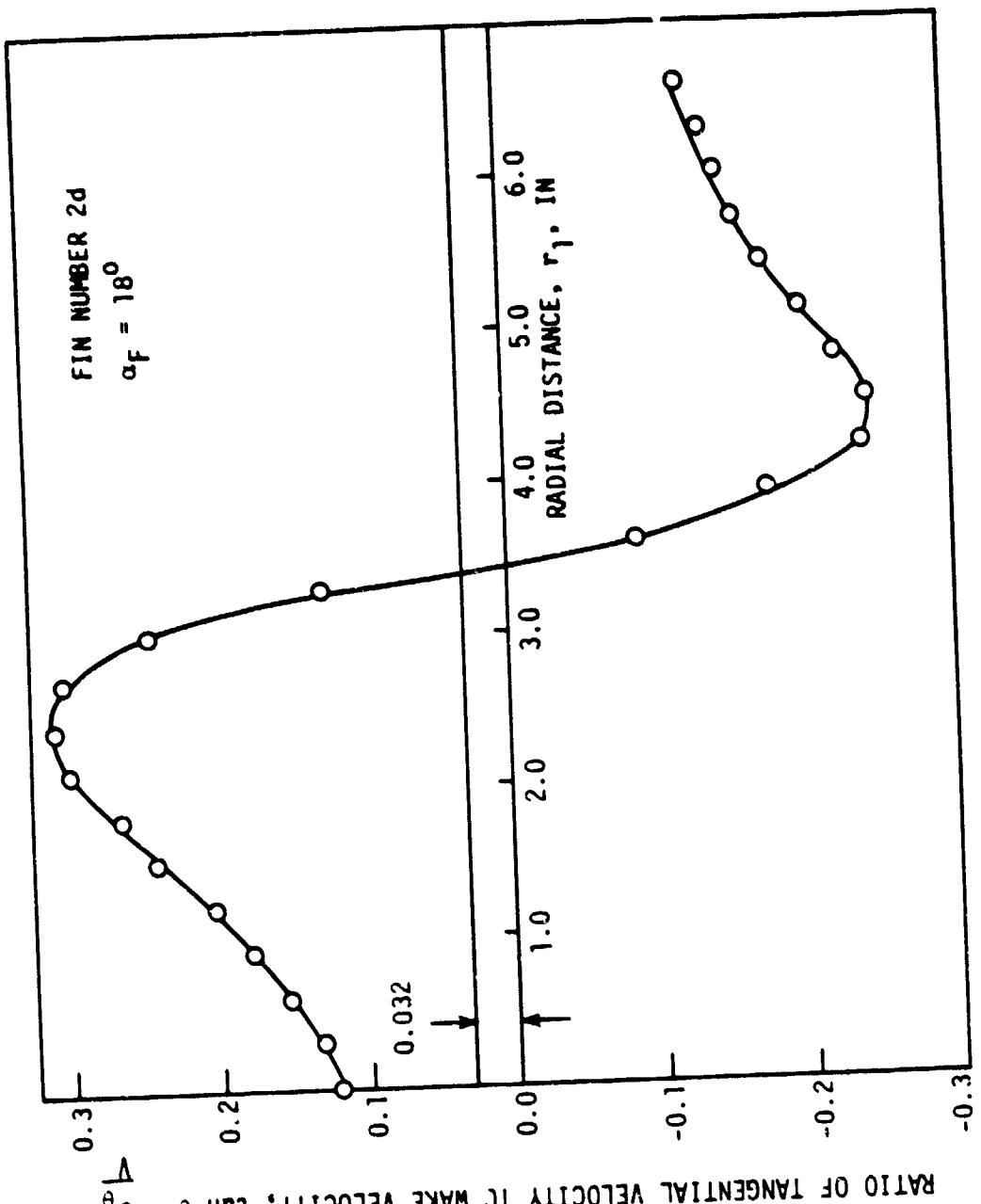

Figure 7. Tangential velocity versus fin vortex radius.

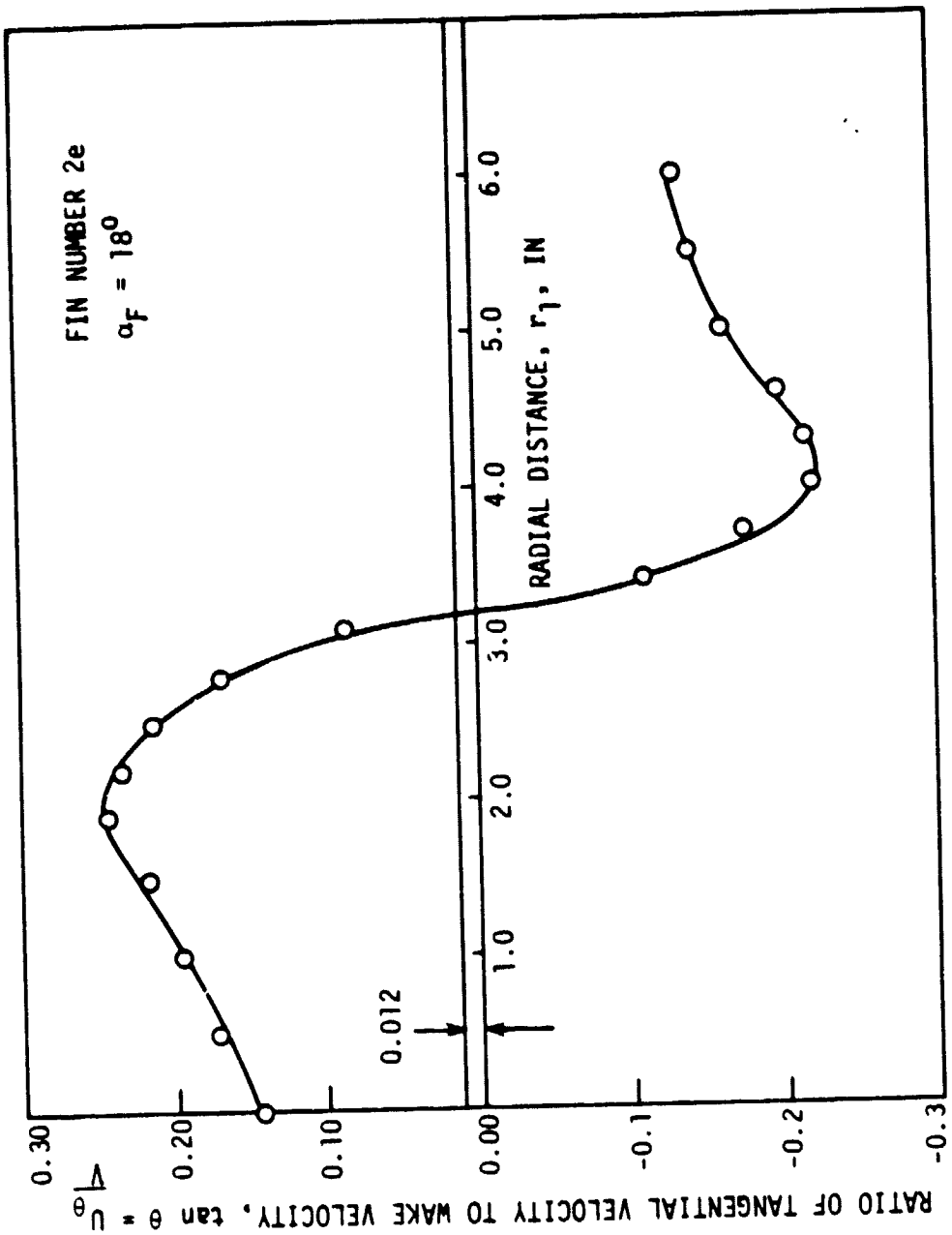

Figure 8. Tangential velocity versus fin vortex radius.

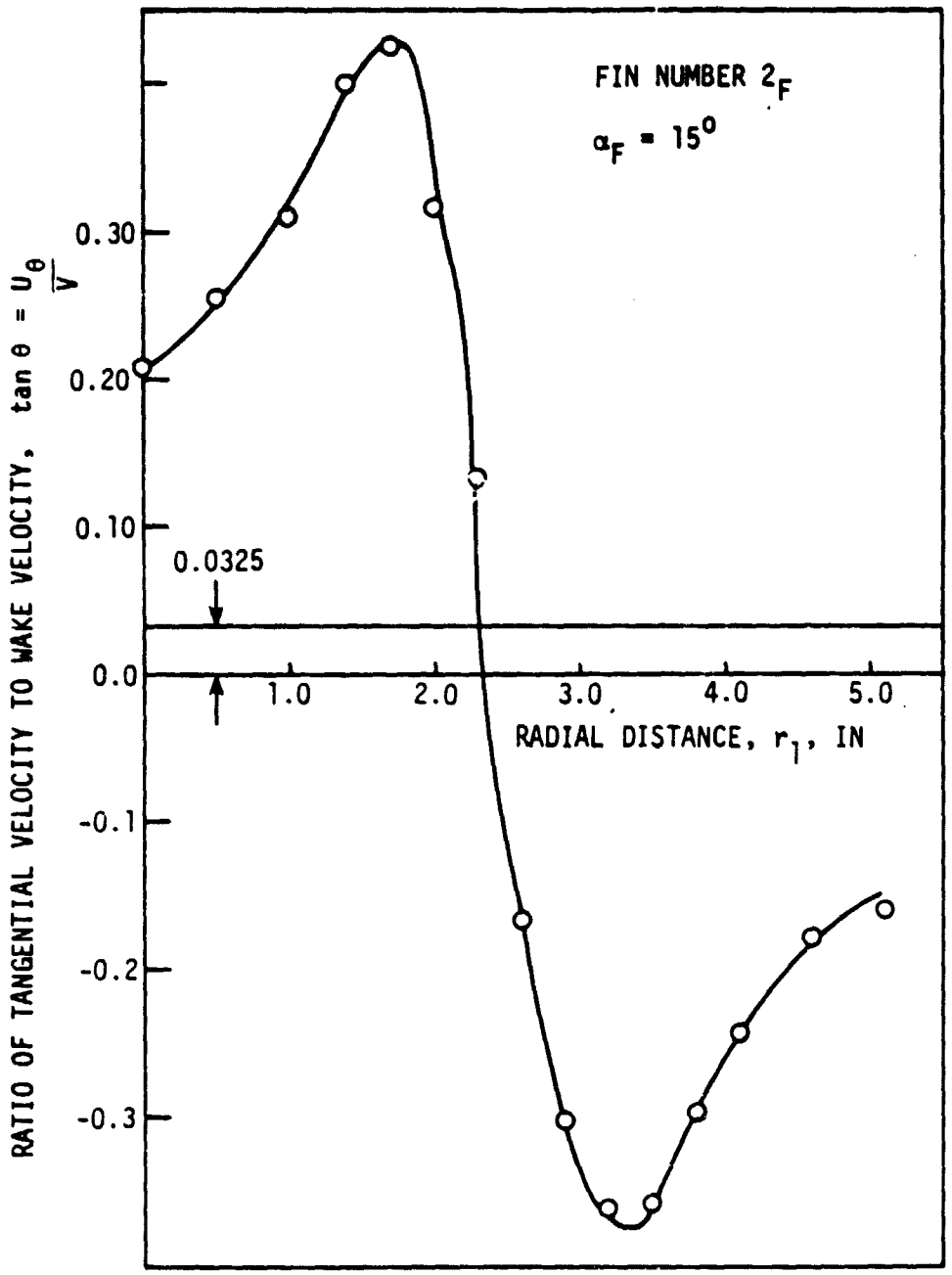

Figure 9. Tangential velocity versus fin vortex radius.

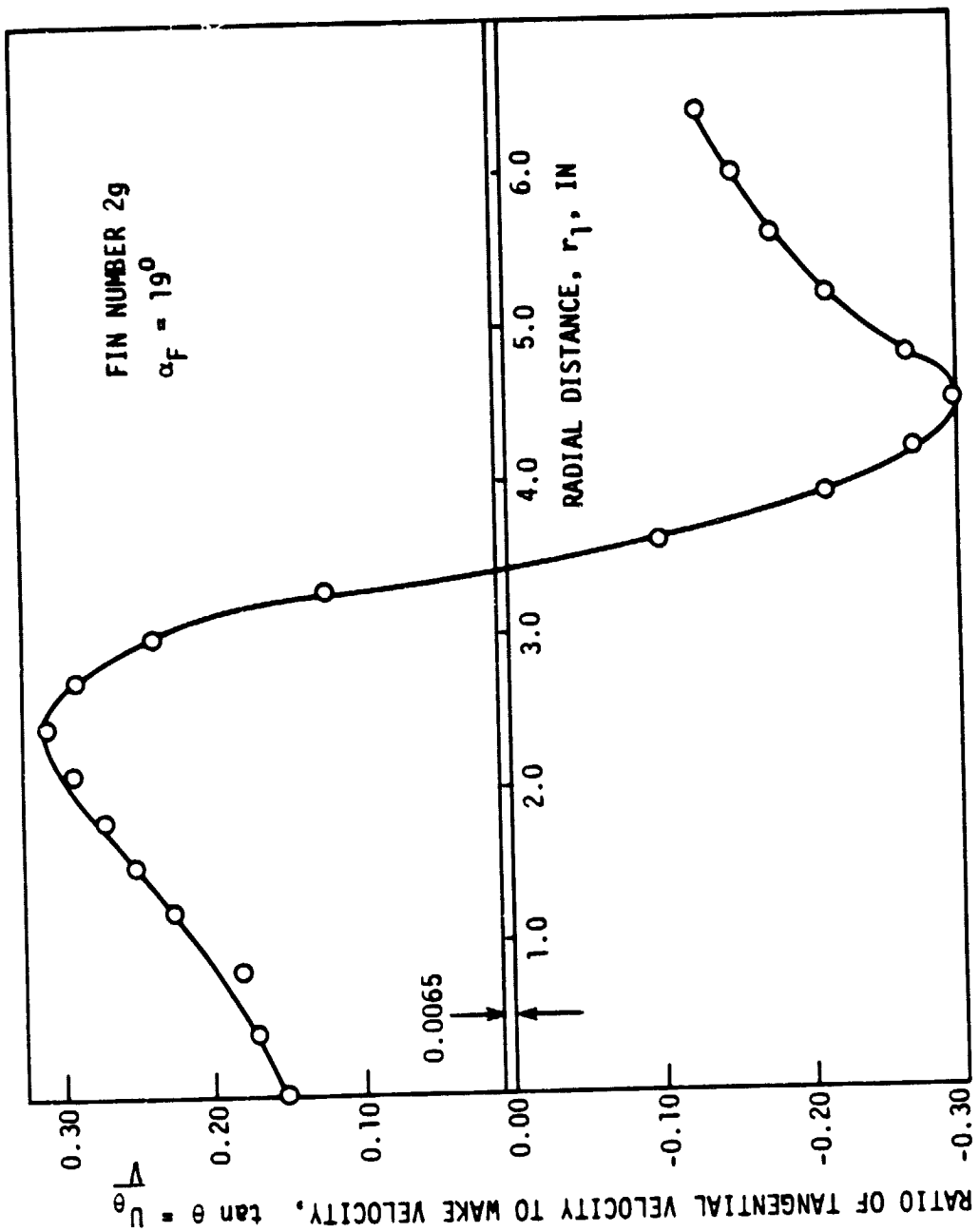

Figure 10. Tangential velocity versus fin vortex radius.

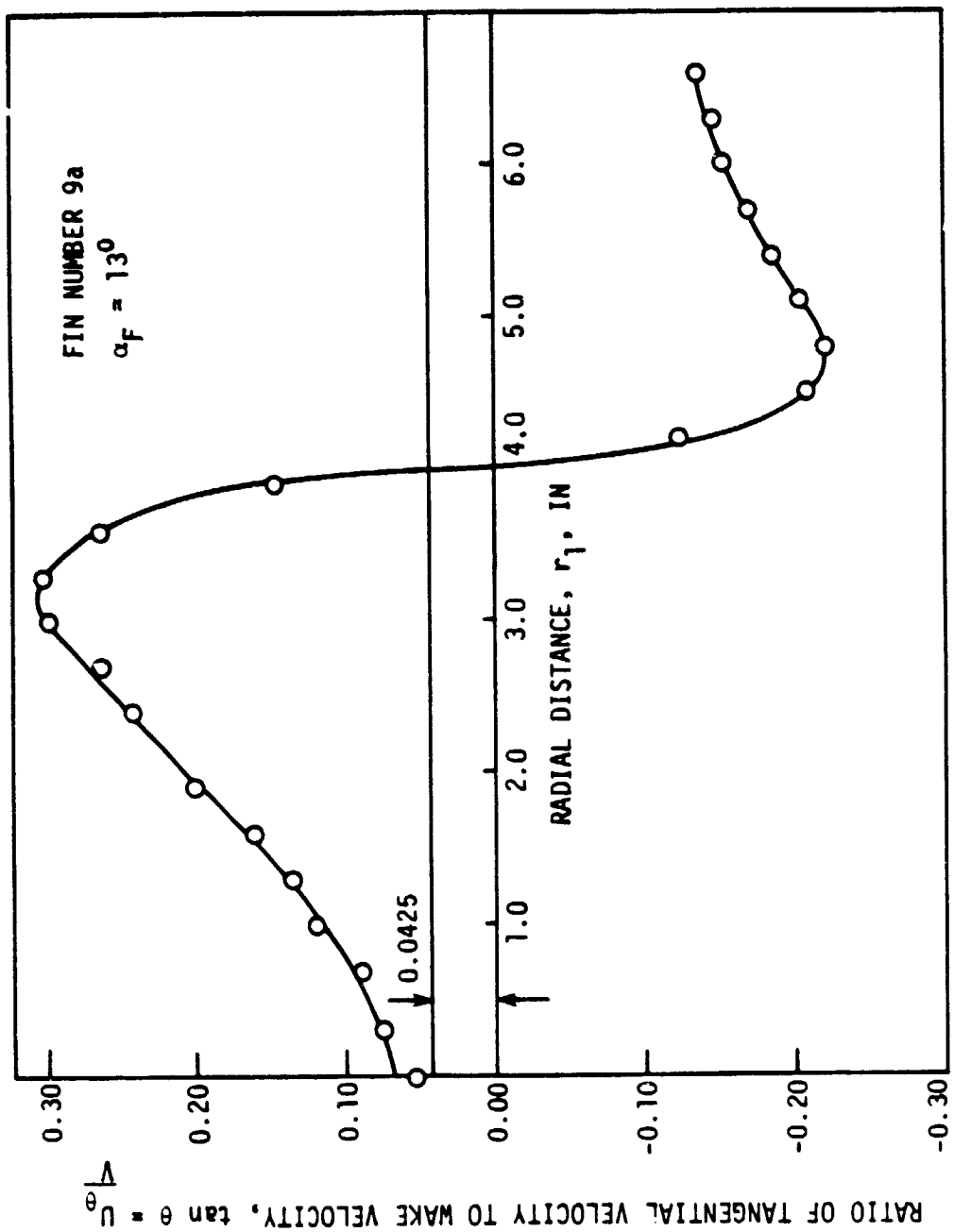

Figure 11. Tangential velocity versus fin vortex radius.

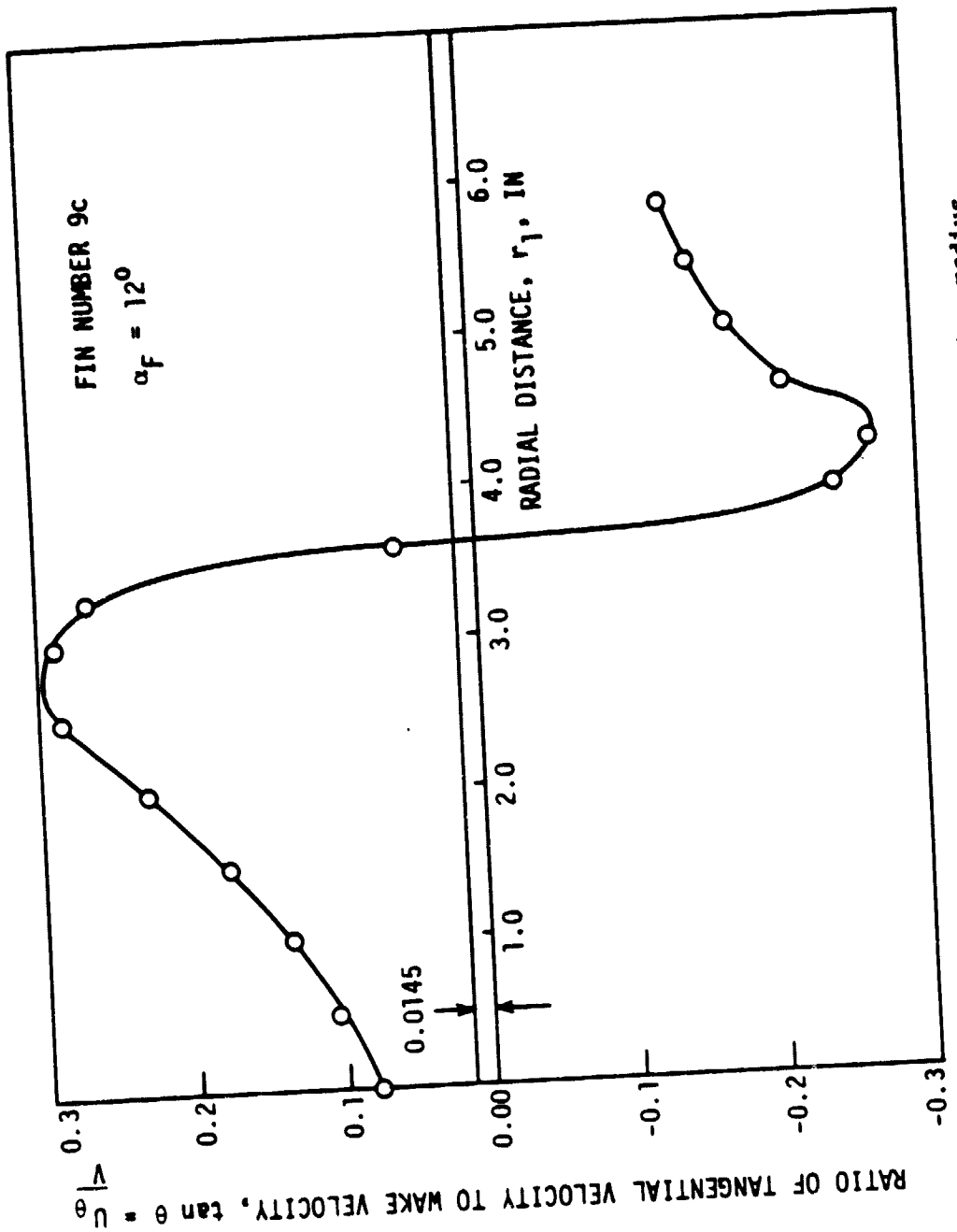

Figure 12. Tangential velocity versus fin vortex radius.

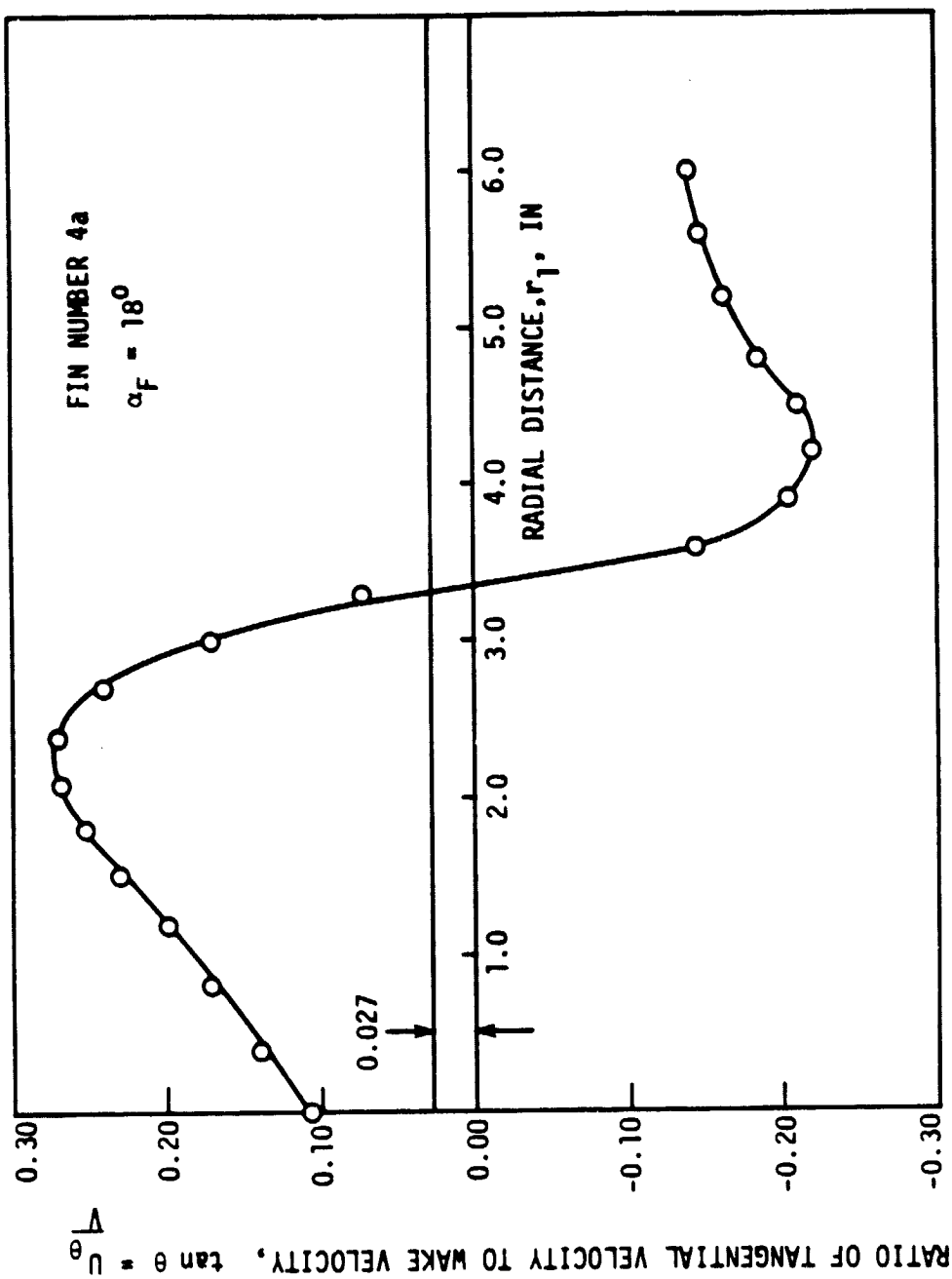

Figure 13. Tangential velocity versus fin vortex radius.

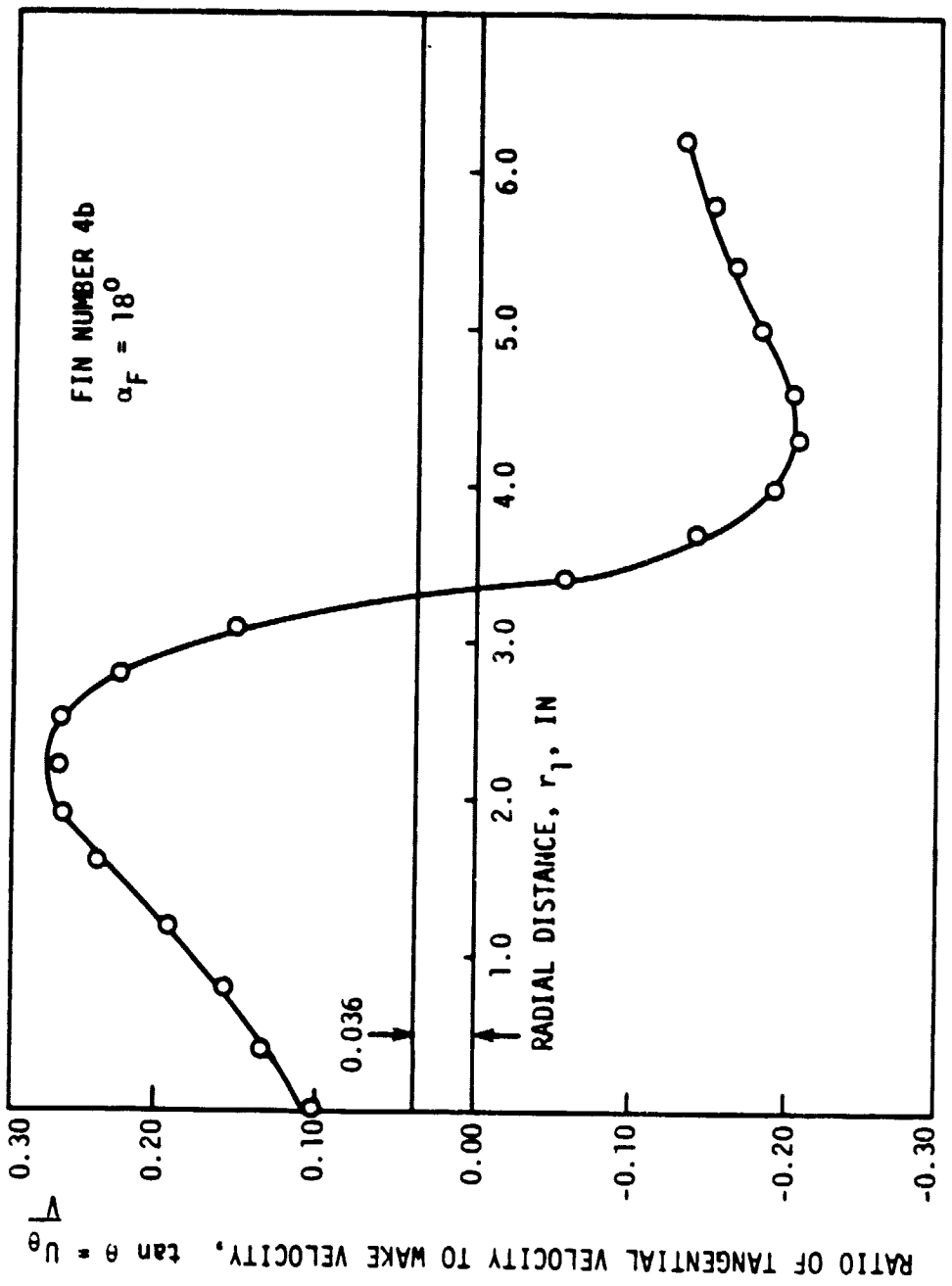

Figure 14. Tangential velocity versus fin vortex radius.

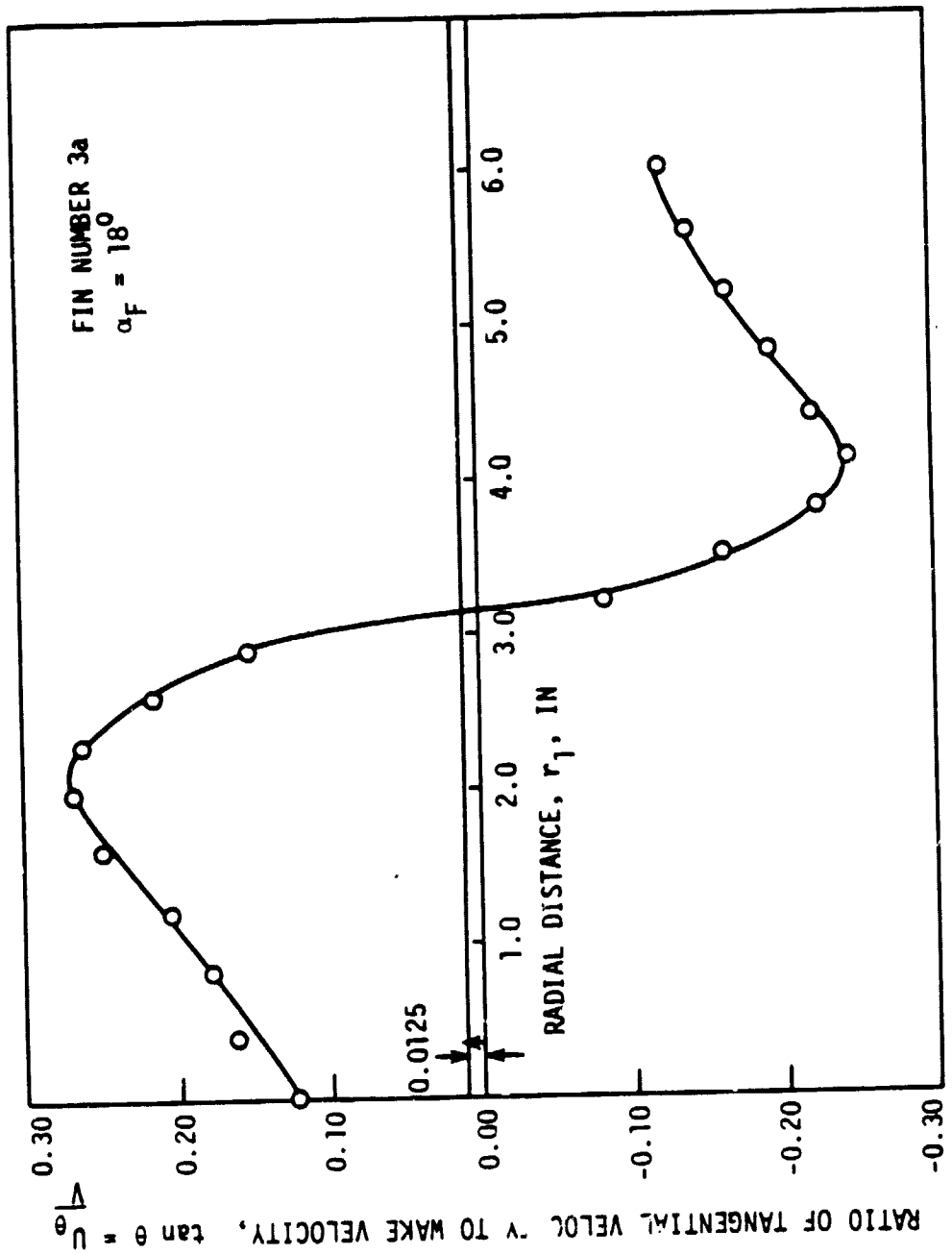

Figure 15. Tangential velocity versus fin vortex radius.

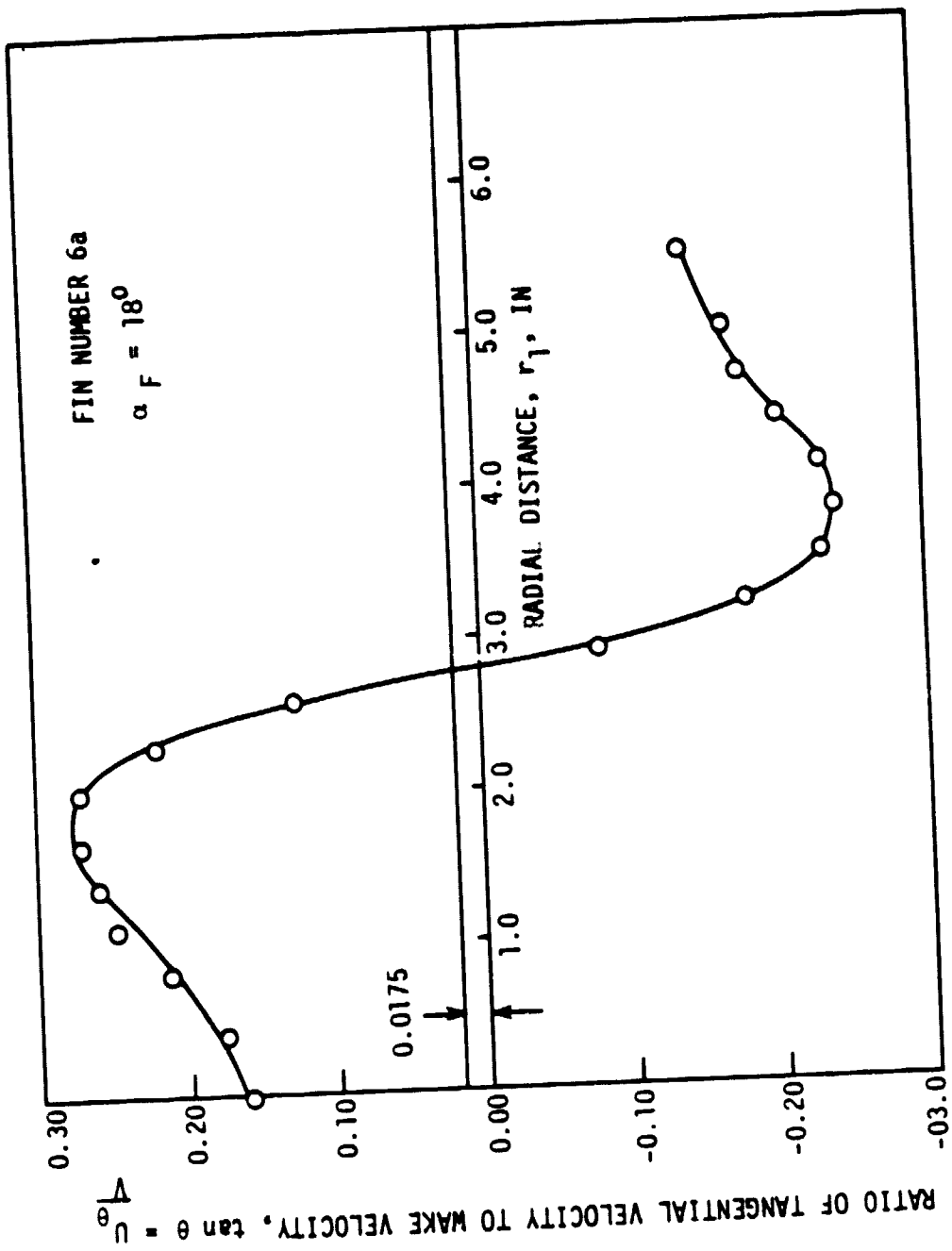

Figure 16. Tangential velocity versus fin vortex radius.

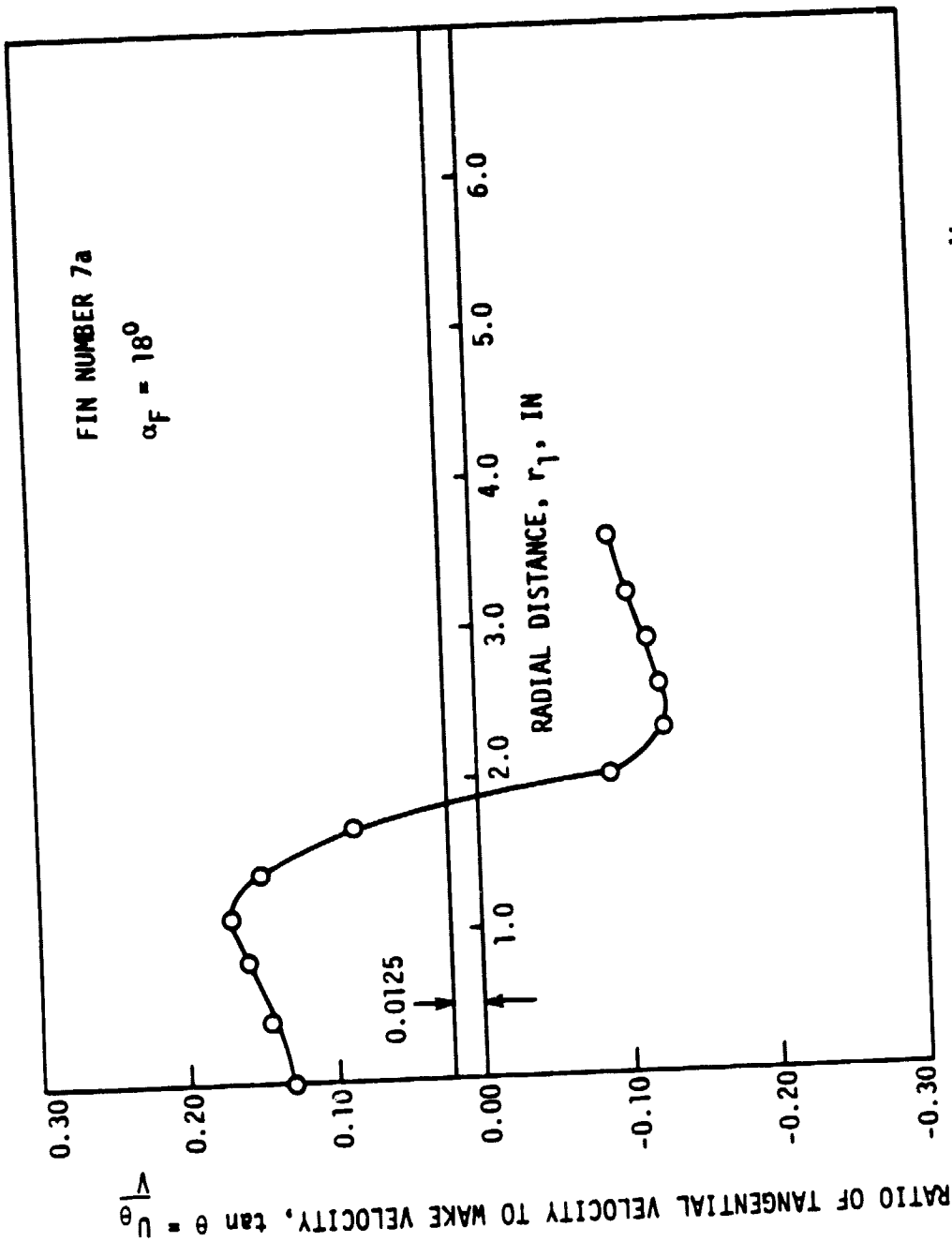

Figure 17. Tangential velocity versus fin vortex radius.

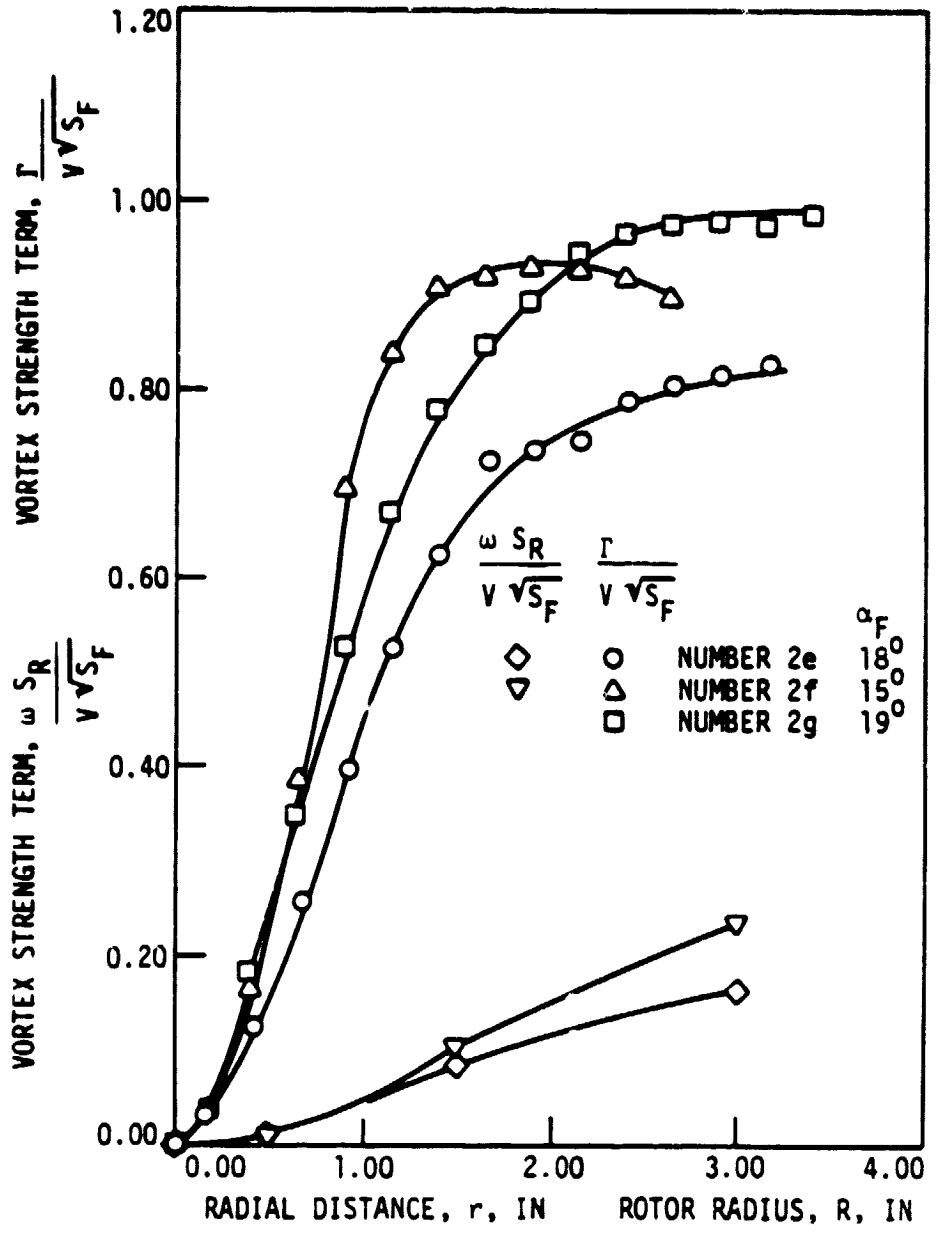

Figure 18. Circulation parameters $\omega S_R/V\sqrt{S_F}$ (determined from rotor tests) and $\Gamma/V\sqrt{S_F}$ (determined from pressure probe tests) as functions of rotor radius R (rotor tests) or vortex radial distance V (pressure probe tests).

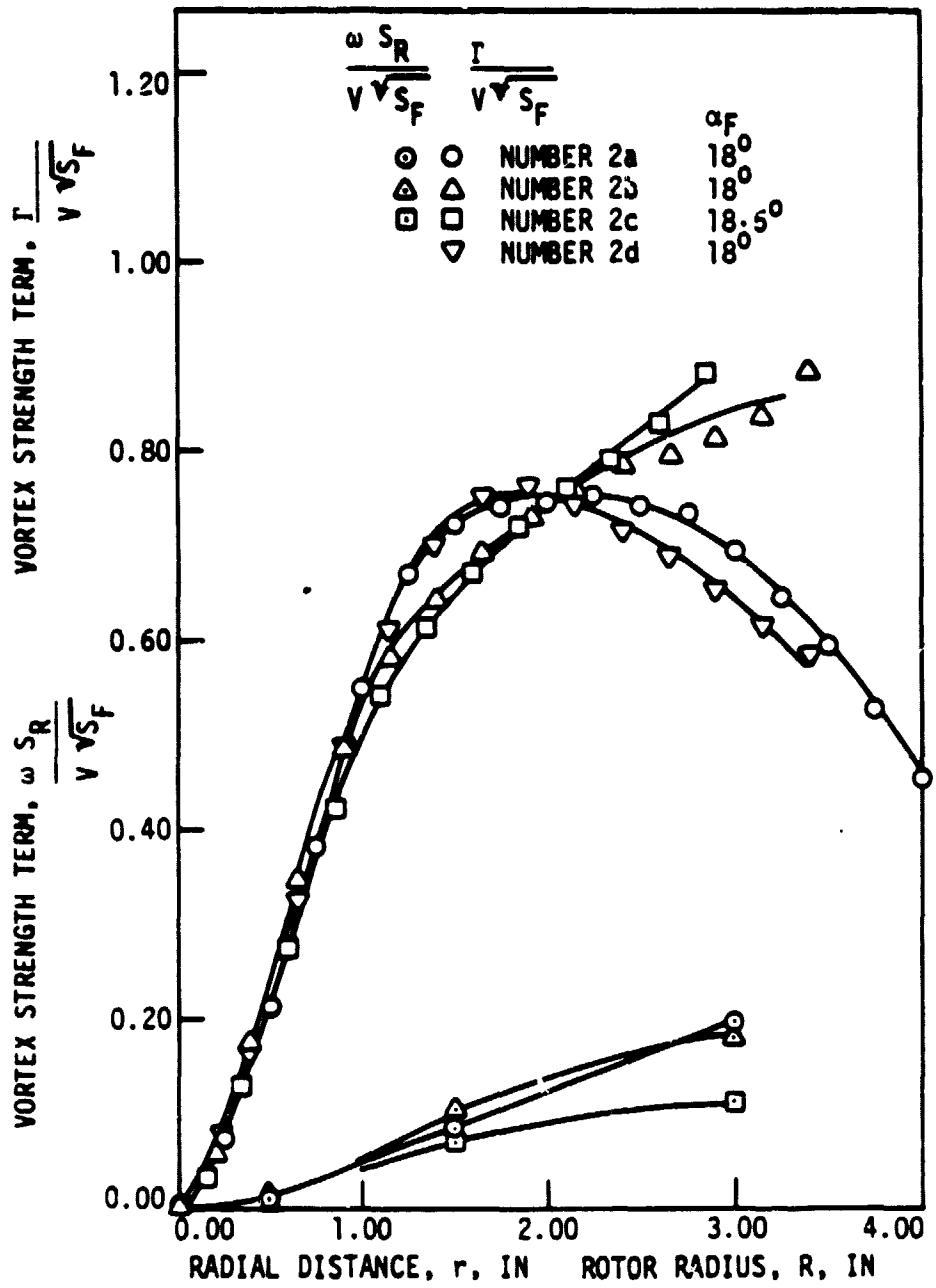

Figure 19. Circulation parameters $\omega S_R/V\sqrt{S_F}$ (determined from rotor tests) and $\Gamma/V\sqrt{S_F}$ (determined from pressure probe tests) as functions of rotor radius R (rotor tests) or vortex radial distance V (pressure probe tests).

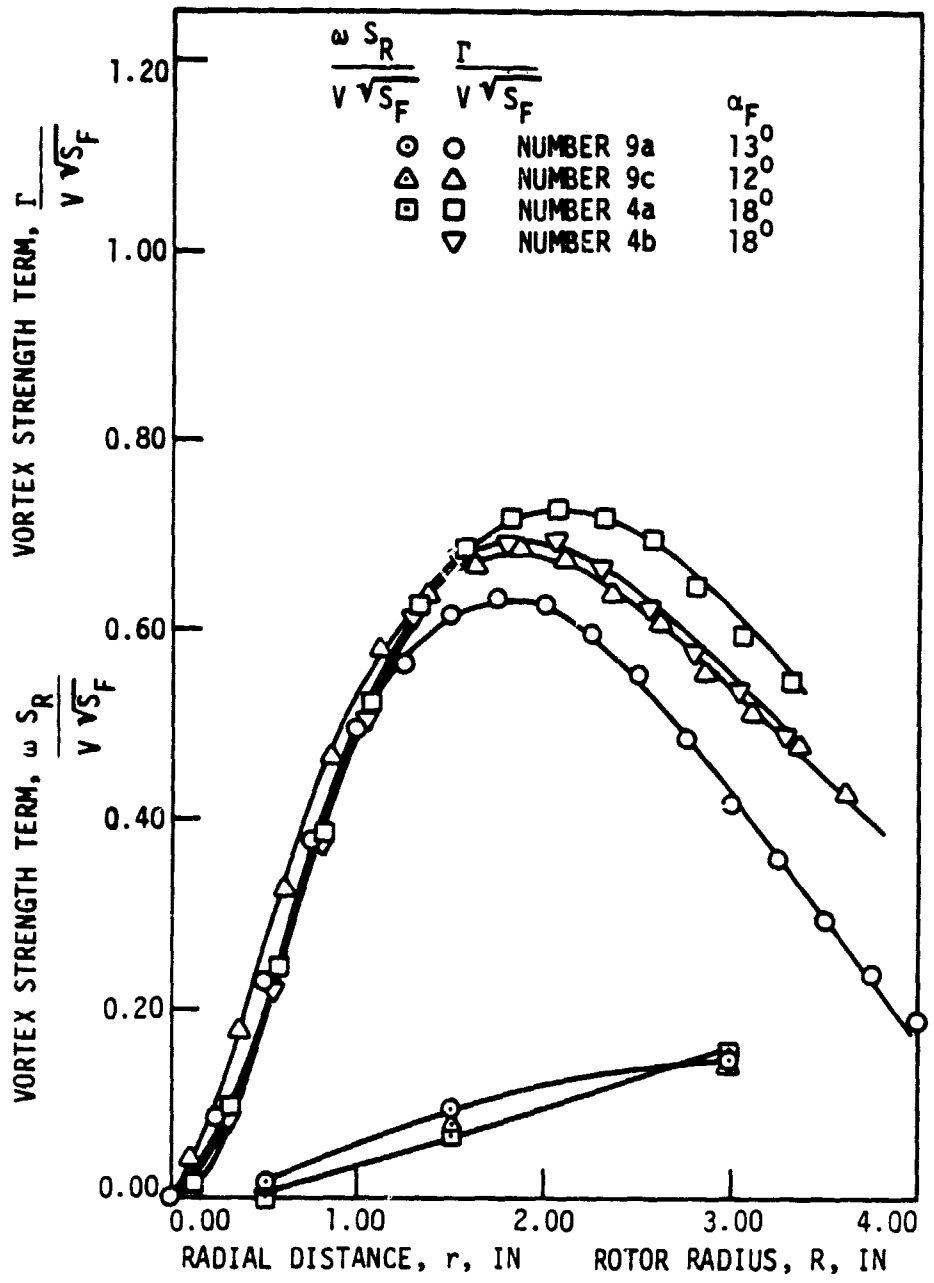

Figure 20. Circulation parameters $\omega S_R/V\sqrt{S_F}$ (determined from rotor tests) and $\Gamma/V\sqrt{S_F}$ (determined from pressure probe tests) as functions of rotor radius R (rotor tests) or vortex radial distance V (pressure probe tests).

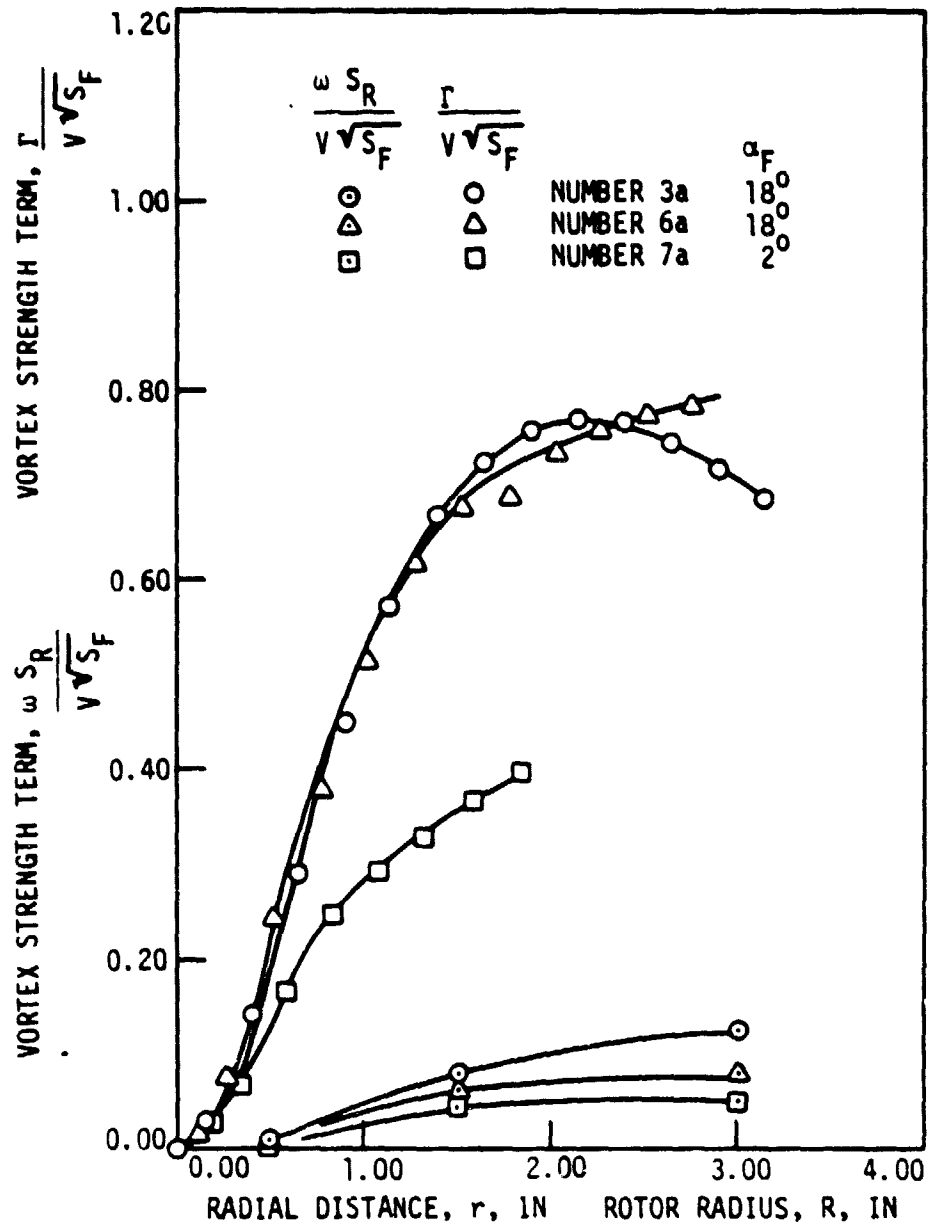

Figure 21. Circulation parameters $\omega S_R/V\sqrt{S_F}$ (determined from rotor tests) and $\Gamma/V\sqrt{S_F}$ (determined from pressure probe tests) as functions of rotor radius R (rotor tests) or vortex radial distance V (pressure probe tests)

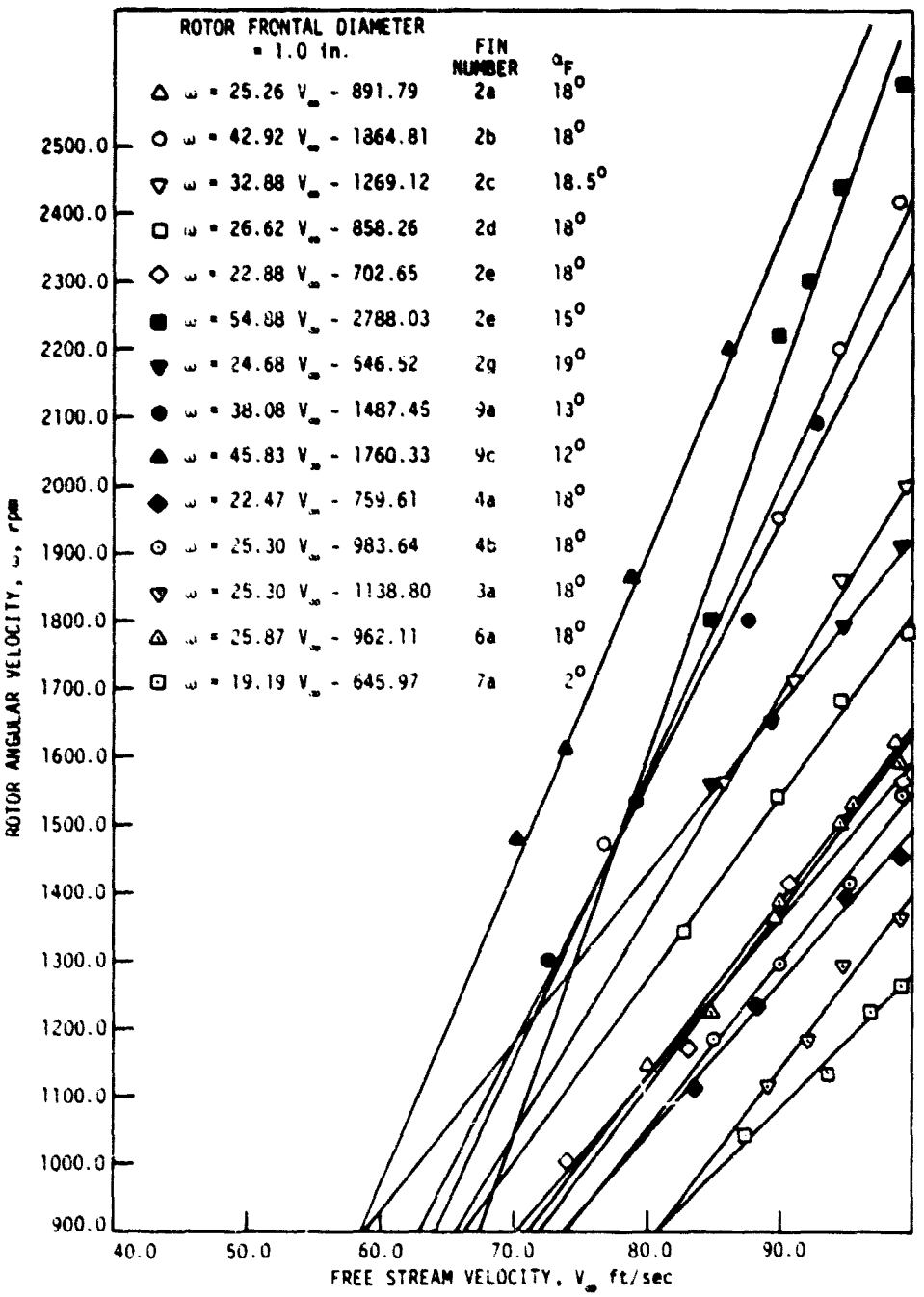

Figure 22. Rotor angular velocity (one-inch rotor) vs free stream speed. The slopes of these curves were used to obtain the values of circulation parameter $\omega S_R/V\sqrt{S_F}$ in Figs. 18-21.

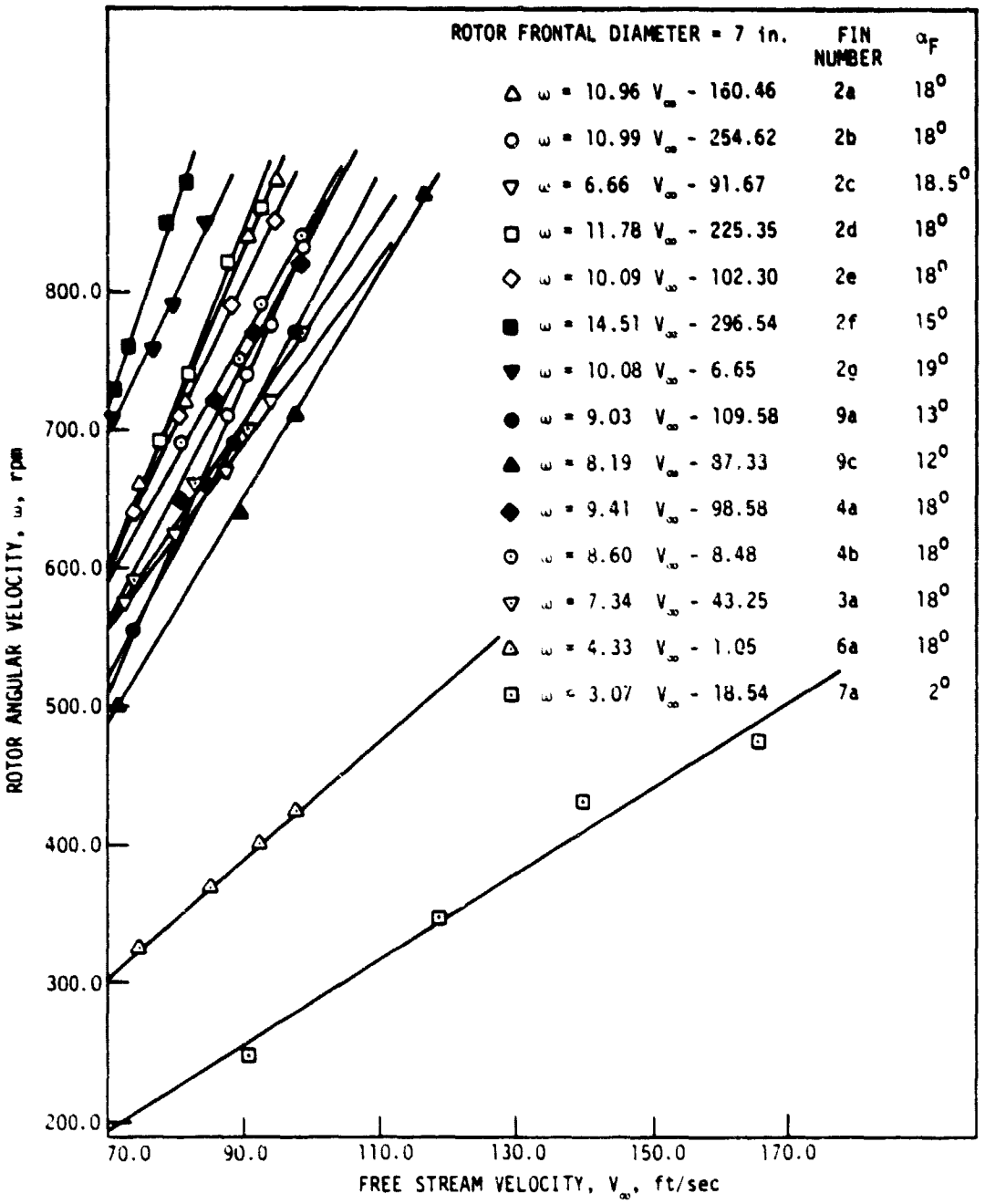

Figure 23. Rotor angular velocity (seven-inch rotor) vs free stream speed. The slopes of these curves were used to obtain the values of circulation parameter $\omega S_R/V\sqrt{S_F}$ in Figs. 18-21.

The $\omega S_R/V_\infty\sqrt{S_F}$ versus R is compared with $\Gamma/V\sqrt{S_F}$ versus r for the tested fins (Figs. 18-21). Since $\Gamma/V_\infty\sqrt{S_F} = K(\omega S_R/V\sqrt{S_F})$, the $\omega S_R/V\sqrt{S_F}$ versus R and $\Gamma/V\sqrt{S_F}$ versus r curves do not coincide (since $K \neq 1$). However, Figs. 18-21 show that the ratio $\omega S_R/V_\infty\sqrt{S_F}$ is directly proportional to S_R; and as S_R increases, $\omega S_R/V_\infty\sqrt{S_F}$ increases also.

Pressure Probe

The left side of almost every wake (Figs. 4-17) has a larger peak than the right side. The reason for this asymmetry is the fact that the vortices move in the upward direction with distance, since the direction of lift on the fins is downward. Therefore, the averages of the right and left peaks can be determined by transferring the r_1 axis and placing it exactly halfway between the peaks. The average peak is probably closer to the actual peak and, thus, is used to determine $\Gamma/V = 2\pi r(U_\theta/V)$ of all vortices.

From Figs. 4-21 the following can be concluded:

1. The comparisons between the tested fins show once again that parabolic configurations (gothic planform) are better vortex generators. The maximum ratio of $\Gamma/V\sqrt{S_F}$ varies from 0.752 for Fin 2a to 0.988 for Fin 2g. The rest of the fins had ranges of $\Gamma/V\sqrt{S_F}$ from 0.4 for Fin 7a to 0.79 for Fin 6a.
2. Comparison between parabolic fins in Figs. 4-10, 18 and 19 shows that Fin 2f at $\alpha_F = 15°$ has the largest rate of increase of U_θ/V and $\Gamma/V\sqrt{S_F}$ with respect to change in radial distance. However, at $\Gamma/V\sqrt{S_F} = 0.9$, this rate of increase starts to

decrease for Fin 2f, while Fin 2g starts with a smaller $\Gamma/rV\sqrt{S_F}$ slope and continues increasing to $\Gamma/V\sqrt{S_F} = 0.988$, as shown in Fig. 18.

3. Comparison between the rest of the fins shows that the vortex of circular Fin 9c has a larger slope (i.e., U_θ/r_1V and $\Gamma/rV\sqrt{S_F}$)than for Fins 9a, 4a, 4b, 3a, 6a, and 7a (Figs. 11-17, 20 and 21). However, this slope starts to decrease at about $\Gamma/V\sqrt{S_F} = 0.6$. Meanwhile, $\Gamma/V\sqrt{S_F}$ of Fin 4a, which started with larger r's (i.e., smaller slope $\Gamma/rV\sqrt{S_F}$), continues to increase until it reaches $\Gamma/V\sqrt{S_F} = 0.724$. Fins 3a and 6a follow the same type of behavior.

The question at this point is, "How can $\Gamma/V\sqrt{S_F}$ of one vortex be larger at some radial distance r than another $\Gamma/V\sqrt{S_F}$ of a different vortex (at the same r); but as r gets larger, the $\Gamma/V\sqrt{S_F}$ of the first vortex becomes smaller than that of the second one?" The answer probably has something to do with changes in the vortex tangential velocity distribution with radius (and perhaps axial distribution) as angle of attack is increased.

Table 1. Comparison between three rotors and the force balance methods.

Fin Number	α_F (degrees)	$\frac{\omega S_R}{V_\infty \sqrt{S_F}}$ R = 6 in.	R = 3 in.	R = 1 in.	$\frac{C_l b}{\sqrt{S_F}}$	a (inches)
2a	18	0.182	0.084	0.0085	0.1278	0.975
2b	18	0.180	0.103	0.0143	0.1310	0.795
2c	18.5	0.111	0.072	0.0112	0.1290	0.875
2d	18	0.196	0.090	0.0090	0.1220	0.995
2e	18	0.166	0.086	0.0077	0.1324	1.045
2f	15	0.238	0.106	0.0184	0.1531	0.80
2g	19	0.166	0.092	0.0083	0.1403	1.045
9a	13	0.148	0.099	0.0153	0.1260	0.80
9c	12	0.133	0.081	0.0126	0.1270	0.745
4a	18	0.158	0.068	0.0077	0.1173	1.00
4b	18	0.147	0.074	0.0088	0.1260	1.075
3a	18	0.123	0.080	0.0086	0.1220	1.00
6a	18	0.072	0.067	0.0088	0.1200	1.00
7a	2	0.052	0.045	0.0066	0.078	0.675